CSEM and Seismic Monitoring
Studies of Deep Low-Enthalpy Reservoirs

Dissertation

for the purpose of obtaining the degree of
doctor at Delft University of Technology
by the authority of the Rector Magnificus prof.dr.ir. T.H.J.J. van der Hagen
chair of the Board for Doctorates
to be defended publicly on
Tuesday 9 December 2025 at 17.30

by

Mahmoud Farouk Marwan Ismail ELTAYIEB

Master of Science in Geophysics, University of Bergen, Norway
born in Dakahlyia, Egypt

This dissertation has been approved by the promotors.

Doctoral committee:

Rector Magnificus	chairman
Dr. ir. G.G. Drijkoningen	Delft University of Technology, promotor
Prof. dr. ir. E.C. Slob	Delft University of Technology, promotor
Prof. dr. H. Maurer	ETH Zurich, Switzerland, promotor
Dr. D. Werthmüller	ETH Zurich, Switzerland, copromotor

Independent members:

Dr. ir. D.J. Verschuur	Delft University of Technology
Prof. dr. ir. L.V. Socco	Delft University of Technology
Prof. dr. P.J. Vardon	Delft University of Technology
Prof. dr. F.M. Wagner	RWTH Aachen University, Germany

Reserve member:

Dr. K. Löer	Delft University of Technology

TUDelft   **ETH**zürich

Contents

Summary

Achieving net zero in greenhouse gases emissions attributed to human activities depends on the transition to renewable energy resources. Low-enthalpy geothermal systems, characterized by their widespread geographical distribution and suitability for direct heating applications, represent a promising alternative to fossil fuels. However, maintaining the long-term efficiency and economic viability of such geothermal reservoirs requires the development of new methods to monitor subtle variations in their properties, particularly those induced by temperature changes during energy extraction and reinjection.

This thesis evaluates the feasibility and advances the methodology of two key geophysical approaches for reservoir monitoring: the controlled-source electromagnetic (CSEM) method and the full waveform inversion (FWI) of seismic data. The research is grounded in two study areas: the Delft campus geothermal project in the Netherlands and the Munich geothermal project in Germany.

A feasibility study of CSEM monitoring was carried out on the Delft site to assess its sensitivity to subtle resistivity variations corresponding to temperature changes in the reservoir. Surface-to-borehole CSEM survey configuration was modeled to optimize source frequency and offset, with results demonstrating the detectability of a 4 Ω·m resistivity increase calculated for a 25 °C temperature drop in the Delft Sandstone reservoir. The study systematically analyzed the impacts of environmental disturbances—random noise, repeatability errors, seasonal near-surface temperature fluctuations, and the presence of steel-cased wells—on the performance of CSEM monitoring data. It was shown that a careful survey design and adequate source parameters allow CSEM monitoring, which is robust against most undesired effects, although steel casings require careful consideration due to their strong field attenuation within a radius of 100 m for a frequency of 1 Hz.

For high-resolution seismic characterization, the thesis develops and validates a novel sequential FWI approach for reconstructing high-resolution models of P-wave velocity and impedance from vertical seismic profiling (VSP) data. The method incorporates travel-time tomography for starting models and introduces a temporal phase resemblance step to improve convergence and mitigate phase error propagation in impedance inversion.

Inversion experiments of synthetic data demonstrate that this approach enables the detection of impedance variations greater than 2 %, directly linked to temperature-driven reservoir changes. Field application to baseline VSP data at the Munich geothermal site confirms the robustness of the approach. A comparative analysis of distributed acoustic sensing (DAS) and conventional geophone-based FWI of P-wave velocity further elucidates the operational benefits and challenges of fiber-optic deployments inside the casing for characterization of geothermal reservoirs.

The results presented in this thesis establish CSEM and advanced seismic FWI as promising and complementary tools for noninvasive monitoring of low-enthalpy geothermal reservoirs. The work concludes with a discussion of current limitations, practical considerations for field deployment, and recommendations for future research.

Samenvatting

Om de uitstoot van broeikasgassen ten gevolge van menselijke activiteiten tot nul te reduceren, moet worden overgeschakeld op hernieuwbare energiebronnen. Geothermische systemen met lageenthalpie, gekenmerkt door hun wijdverspreide geografische verspreiding en geschiktheid voor directe verwarmingstoepassingen, vormen een veelbelovend alternatief voor fossiele brandstoffen. Om de efficiëntie en economische levensvatbaarheid van dergelijke geothermische reservoirs op de lange termijn te behouden, moeten er echter nieuwe methoden worden ontwikkeld om subtiele variaties in hun eigenschappen te controleren, met name variaties die worden veroorzaakt door temperatuurveranderingen tijdens de energiewinning en herinjectie.

Dit proefschrift evalueert de haalbaarheid en ontwikkelt de methodiek van twee belangrijke geofysische benaderingen voor reservoirmonitoring: de controlled-source elektromagnetische (CSEM) methode en full waveform inversie (FWI) van seismische data. Het onderzoek is gebaseerd op twee studiegebieden: het Delft campus geothermieproject in Nederland en het München geothermieproject in Duitsland.

Op de locatie in Delft werd een haalbaarheidsstudie uitgevoerd naar CSEM-monitoring om de gevoeligheid voor subtiele weerstandsvariaties die samenhangen met temperatuurveranderingen in het reservoir te beoordelen. De configuratie van een oppervlakte-tot-boorgat CSEM-metingsopstelling werd gemodelleerd om de bronfrequentie en offset te optimaliseren, waarbij werd aangetoond dat een toename van 4 Ω·m in weerstand als gevolg van een temperatuurdaling van 25 $^{\circ}$C in het Delft Zandsteenreservoir waarneembaar is. De studie analyseerde systematisch de impact van omgevingsverstoringen—zoals ruis, herhaalbaarheidsfouten, seizoensgebonden temperatuurschommelingen nabij het oppervlak en de aanwezigheid van stalen beklede putten—op de prestaties van CSEM-monitoringsdata. Uit het onderzoek bleek dat een zorgvuldige surveyopzet en adequate bronparameters CSEM-monitoring robuust maken tegen de meeste ongewenste effecten, hoewel stalen bekledingen bijzondere aandacht vereisen vanwege hun sterke veldverzwakking binnen een straal van 100 m.

Voor seismische karakterisering met hoge resolutie ontwikkelt en valideert het proefschrift

een nieuwe sequentiële FWI-benadering voor het reconstrueren van gedetailleerde modellen van P-golf snelheid en impedantie op basis van vertical seismic profiling (VSP) data. De methode maakt gebruik van reistijdtomografie voor de startmodellen en introduceert een temporele fase-overeenkomstenstap om de convergentie te verbeteren en fasefouten in de impedantie-inversie te beperken. Inversie-experimenten met synthetische data tonen aan dat deze benadering het mogelijk maakt om impedantievariaties groter dan 2 % te detecteren, direct gekoppeld aan temperatuurgedreven veranderingen in het reservoir. Toepassing op baseline VSP-data van de locatie in München bevestigt de robuustheid van de aanpak. Een vergelijkende analyse van distributed acoustic sensing (DAS) en conventionele geofone-gebaseerde FWI van P-golfsnelheid belicht bovendien de operationele voordelen en uitdagingen van vezeloptische implementaties in de casing voor de karakterisering van geothermische reservoirs.

De resultaten uit dit proefschrift tonen aan dat CSEM en geavanceerde seismische FWI veelbelovende en complementaire hulpmiddelen zijn voor niet-invasieve monitoring van lage-enthalpie geothermische reservoirs. Het werk wordt afgesloten met een bespreking van huidige beperkingen, praktische overwegingen voor veldimplementatie, en aanbevelingen voor toekomstig onderzoek—including de gezamenlijke inversie van elektromagnetische en seismische data, ondersteund door verbeterde modellering van complexe reservoirgeometrieën en gevalideerd door veldcampagnes op schaal.

List of Symbols

Symbol	Description	Units
$A^{\pm}, B^{\pm}$	Boundary condition coefficients	–
$\mathbf{C}(\mathbf{x})$	Electrical conductivity tensor	S/m
$\mathbf{E}(\mathbf{x})$	Electric-field vector	V/m
$\mathbf{H}(\mathbf{x})$	Magnetic-field vector	A/m
$\mathbf{I}$	Identity matrix	–
$\mathbf{J^e}(\mathbf{x})$	External current density vector	A/m^2
$\mathbf{J}$	Jacobian matrix	–
$\mathbf{K}(\mathbf{x})$	Dielectric permittivity tensor	F/m
L	Smoothing operator	–
$\mathbf{M_p}(\mathbf{x})$	Magnetic permeability tensor	H/m
R_r	Cross correlation	–
$\mathbf{S}$	Scaling matrix	–
T	Temperature	°C
V_{P}	P-wave velocity	m/s
V_{S}	S-wave velocity	m/s
a	Temperature coefficient of resistivity	–
$\mathbf{f}$	Body-force vector	N/m^3
f	Frequency	Hz
g	Sampling time lag	s
k_r	Horizontal radial wavenumber	rad/m
k_z	Vertical wavenumber	rad/m
m	Model vector	–
m_{true}	Inverted model vector	–

Symbol	Description	Units
m_{true}	True model vector	–
r	Radial distance	m
t	Time	s
t_d	Seismic trace duration	s
z	Depth	m
α	Damping factor	–
β	Smoothing factor	–
Δf	Change in frequency	Hz
Δm_q	Model perturbation	–
δd	Data residual	–
ϵ_d	Relative data error	–
ϵ_m	Relative model error	–
λ	First Lamé parameter	Pa
μ	Shear modulus (Second Lamé parameter)	Pa
ρ	Mass density	kg/m^3
ϕ	Scalar compressional potential	–
ψ	Scalar shear potential	–
ω	Angular frequency, $\omega = 2\pi f$	rad/s
$\mathbf{u}$	Displacement vector	m
∇	Vector differential operator	–
d_{calc}	Calculated data	–
d_{obs}	Observed data	–
mod	Wrapping operator	–

Chapter 1

Introduction

1.1 Background and motivation

Hazards of Anthropogenic Climate Change

Climate change has impacted the Earth's ecosystem in recent decades (Karl and Trenberth, 2003). The emission of greenhouse gases (GHG) into the atmosphere (Ledley et al., 1999), primarily from the burning of fossil fuels, such as coal, oil and gas, led to an increase in global temperatures (Yoro and Daramola, 2020), causing widespread environmental and humanitarian consequences (McMichael and Haines, 1997; Short and Neckles, 1999; Doherty and Clayton, 2011). Rising sea levels and more frequent meteorological events are a few tangible examples (Etkins and Epstein, 1982; Michener et al., 1997). A fundamental aspect of mitigating these consequences is a rapid transition in the global energy sector, which accounts for the largest share of GHG emissions, to renewable energy (Markard, 2018). Renewable energy resources, such as solar, wind, and geothermal, offer good alternatives by reducing GHG emissions while providing a long-term renewable resource (Ellabban et al., 2014; Twidell, John, 2021). Among these, geothermal energy is promising due to its ability to generate continuous base-load power with minimal environmental footprint (Fridleifsson, 2001, 2003; Aljubran and Horne, 2024). As the transition to clean energy accelerates, research and development in geothermal energy systems are necessary to facilitate their widespread economic deployment, thus contributing to the mitigation of climate change and the advancement of a more sustainable future.

Geothermal energy as a sustainable solution

Geothermal energy is thermal energy derived from the interior of the Earth, originating from the decay of radioactive isotopes such as uranium and thorium, and the residual

heat from the planet's formation (Turcotte and Schubert, 2002). This heat travels upward through the crust at a rate that depends, among other factors, on the thermal conductivity of the rocks (Clauser, 2009). Geothermal energy resources are classified according to the temperature and location of their reservoirs into high-enthalpy and low-enthalpy systems (Munoz, 2014). High-enthalpy systems are typically found in tectonically active regions with high temperatures exceeding 150 °C, making them suitable for the generation of electricity through conventional steam power plants (Muffler and Cataldi, 1978). Low-enthalpy systems operate at temperatures below 150 °C and are used primarily for direct heating applications, such as district heating, greenhouse agriculture, and industrial processes (Martín-Gamboa et al., 2015). Although high-enthalpy systems are commonly exploited in volcanic regions, low-enthalpy systems are more widespread and accessible geographically, offering a broader potential for geothermal energy utilization (Moeck, 2014).

Importance of low-enthalpy geothermal reservoirs

Low-enthalpy geothermal systems are commonly found in porous or fractured sedimentary or crystalline bedrocks, called reservoirs (Legarth et al., 2003). Low-enthalpy reservoirs should be saturated with groundwater, which allows heat transport through convection (Chandrasekharam and Bundschuh, 2008). The thermal recharge usually occurs through natural conduction, which is a slower process than convection (Saeid et al., 2015). Heat production involves pumping geothermal fluids, e.g. ground water, to the surface through production wells, where heat is extracted via heat exchangers for direct use (Crooijmans et al., 2016). The cooled fluids are commonly pumped back into the reservoir through injection wells (Pruess and Bodvarsson, 1984; Diaz et al., 2016).

1.2 Problem statement and role of monitoring

Issues associated with geothermal energy production

In the short term, temperature reductions occur in reservoir volumes around return wells and typically diffuse to farther volumes over time (Bödvarsson and Tsang, 1982). In the long term, temperature changes lead to a wider thermal depletion, where the heat flux from deeper geological layers may not fully compensate for the extracted energy (Evans et al., 2012). Heat production can also lead to changes in geomechanical stresses (Uribe-Patino et al., 2017), which in turn alters fracture networks (Gan and Elsworth, 2014). The extraction of geothermal fluids can also cause pressure drops, altering the mechanical equilibrium in the subsurface (Jeanne et al., 2014). These thermobaric effects potentially trigger microseismic events, especially in systems where fluid reinjection is used.

Why monitoring low-enthalpy reservoirs is essential

Monitoring the temperature and pressure of low-enthalpy geothermal reservoirs is fundamental to ensuring their long-term efficiency and operational safety (Poulsen et al., 2015). If reinjected fluids rapidly circulate back to production wells without spending enough time in the low-enthalpy reservoir, the thermal recovery process is significantly compromised, leading to early thermal breakthroughs (Bödvarsson and Tsang, 1982; Fadel et al., 2022). This effect can diminish the economic feasibility of the geothermal project. Periodic monitoring of reservoir temperature, fluid circulation, and changes in fluid pathways helps optimize reinjection strategies and reservoir management (Weinbrandt et al., 1975). Another key aspect of reservoir monitoring is tracking pressure variations and their impact on subsurface stress conditions (Tomac and Sauter, 2018). In some cases, stress changes can lead to the reactivation of pre-existing faults or induce microseismic activity, particularly in reservoirs with complex fracture networks (Martin III, 1972). Monitoring pressure dynamics and possible induced seismicity is therefore crucial for minimizing the risk of induced seismicity and ensuring the structural integrity of the reservoir and minimizing potential operational risks.

1.3 Limitations of existing monitoring approaches

Several traditional and modern borehole-based, geochemical, geophysical, and simulation techniques have been employed to track subsurface changes over time. These methods can be broadly categorized into the following:

- **Well-based techniques**: Traditional techniques rely mainly on borehole-based measurements, such as temperature and pressure logging, tracer testing, and flow-rate monitoring (Freifeld et al., 2009). These methods provide a valuable understanding of reservoir dynamics. However, they suffer from spatial limitations because they cover localized areas around wells (Patidar et al., 2022). In addition, tracer tests provide indirect, time-averaged information on fluid pathways and require extensive sampling campaigns (Ren et al., 2023). Implementing multiple monitoring wells to improve spatial coverage significantly increases operational costs, making large-scale monitoring impractical (Sanni et al., 2017).

- **Reservoir modeling**: Numerical reservoir models, such as thermal-hydraulic-mechanical (THM) simulations, are widely used to predict reservoir behavior with different heat production rates (Pandey et al., 2018). Although these models integrate available geological, geophysical, and well data, their accuracy depends on the quality and completeness of the input data (Fanchi, 2005). Many modeling ap-

proaches have assumptions that do not fully capture complex reservoir processes, leading to uncertainties in long-term monitoring (Todd et al., 1972). Furthermore, integrating time-lapse monitoring data into real-time reservoir management remains a challenge due to computational constraints and data assimilation difficulties (Saputelli et al., 2006; Jansen et al., 2009).

- **Surface-based geophysical methods**: Geophysical monitoring at the earth's surface may include gravity, electromagnetic (EM) and seismic methods as non-invasive means for characterizing the changes in the reservoir (Day-Lewis et al., 2017). Gravity and interferometric synthetic aperture radar (InSAR) methods might be useful to track surface deformation related to reservoir pressure changes but lack direct insight into fluid and heat flow (Zumberge et al., 2008; Smith and Knight, 2019). Electrical and electromagnetic techniques, such as magnetotellurics (MT) and controlled-source electromagnetics (CSEM), help identify changes in resistivity associated with subsurface temperature and fluid variations (Buselli and Lu, 2001; Stummer et al., 2004; Uhlemann et al., 2015). However, these methods struggle with depth penetration and small-scale resolution (Vozoff, 1980). Thermal contraction due to heat production can cause subtle shifts in the propagation characteristics of seismic waves, which can be identified using time-lapse seismic surveys (Wu et al., 2013; Zhang et al., 2016). Moreover, seismic monitoring allows the detection of natural and induced microseismic events, which can reveal stress variations and fluid flow patterns within the reservoir (Verliac and Le Calvez, 2021). However, seismic monitoring of both subtle variations associated with temperature changes and microseismic activity requires developing new approaches to estimate acoustic or elastic properties with sufficient accuracy (Zang et al., 2014; Edwards et al., 2015; Zhang et al., 2016).

Given the limitations of the previously mentioned techniques, there is a growing demand to develop advanced monitoring approaches that offer wide spatial coverage, better sensitivity to small-scale reservoir changes, and cost-effective deployment.

1.4 Potential of geophysical monitoring

Recent advancements in the acquisition and processing techniques of CSEM and seismic data offer new opportunities for non-invasive, high-resolution 3D characterization of low-enthalpy reservoirs, allowing for monitoring. These techniques address some of the limitations of surface-based geophysical characterization and monitoring methods by providing improved sensitivity and resolution to subsurface changes in temperature, fluid movement associated with flooding fronts or sequestration, and stress changes.

CSEM is highly sensitive to electrical resistivity, which is linearly proportional to the temperature distribution of geothermal fluids (Constable, 2010; Newman et al., 2010). Thus, temperature changes due to heat production result in resistivity variations (Marsden et al., 1973; Llera et al., 1990). Unlike passive electrical methods, for example magnetotelluric, CSEM uses a man-made transmitter that generates repeatable and controllable fields with high signal-to-noise (SNR) (Constable, 2013). The exponential decay of diffusive EM fields with depth is frequency-dependent. High frequencies naturally offer high resolving capabilities useful for characterization and monitoring, but will be heavily attenuated at the reservoir level (Um and Alumbaugh, 2007). Defining a suitable configuration for collecting CSEM data over time (time lapse) to detect resistivity variations in a low-enthalpy reservoir setting is a research gap. Furthermore, it is unknown whether the CSEM data from repeated surveys over low-enthalpy reservoirs will have an adequate difference because of relevant resistivity variations, a difference greater than noise interference and other environmental or instrumental effects.

Seismic methods provide primary information on the mechanical and thermal properties of the subsurface (Rost and Thomas, 2002). Full waveform inversion (FWI) approaches help reconstruct high-resolution subsurface models from seismic data (Warner et al., 2013). Developing new FWI approaches to characterize low-enthalpy reservoirs with sufficient resolution to capture variations related to temperature changes is still an unresolved research challenge. Furthermore, modern sensors such as distributed acoustic sensing (DAS) leverages existing fiber-optic cables as dense arrays, offering a cost-effective alternative to conventional geophones (Mestayer et al., 2011). However, the ability of DAS data to help high-resolution characterization, useful for monitoring low-enthalpy reservoirs, has not been tested.

1.5   Research objectives

One key objective of this thesis is to evaluate the feasibility of CSEM monitoring of subtle resistivity variations caused by temperature changes inside a low-enthalpy geothermal reservoir, using a subsurface model of the Delft campus geothermal project. To facilitate such monitoring with sufficient confidence, I aim at identifying the optimal survey design, i.e. layout, source frequency, and offset. In addition, I will quantify the impact of other environmental effects that introduce differences in, distort, or mask time-lapse EM fields. These effects include and are not limited to background natural and artificial noise, instruments redeployment, and steel infrastructure.

I also develop a novel seismic FWI approach for high-resolution characterization of the acoustic impedance of low-enthalpy reservoirs; thus variations generated by heat production can be detected. To increase computational efficiency and ensure convergence of the

FWI, I deploy initial models estimated from travel time tomography, where I design an inversion algorithm of arrival times to give a layered model for offset VSP. To evaluate the performance of this approach, I applied it to a field VSP data set recorded by geophones at a geothermal site in Munich, Germany. The subsurface of the Munich geothermal site has large properties contrasts, posing significant challenges for existing FWI approaches.

Finally, I evaluate the potential of seismic FWI of DAS data collected with a fibre-optic cable inside the casing for high-resolution characterization of the subsurface of the Munich geothermal site. This DAS data was collected at the same doublet as the geophones data but in another production well. I redefine the residuals and the sensitivities in the previously mentioned FWI approach to be in terms of strain rates—unit measured by the fibre-optic cable. The resulting models from the inversion of the DAS data are compared with those of the geophone data, establishing the merits and limitations of DAS in terms of data quality and resolution when collected inside the casing.

By addressing these objectives, I show the ability of geothermal reservoir monitoring using the CSEM and the seismic method. The findings will contribute to more sustainable reservoir management and optimization of heat-extraction strategies in low-enthalpy reservoirs.

1.6   Outline of the thesis

Chapter 2 outlines the study areas and methodologies employed in this research. It focuses on two deep geothermal projects: the Delft campus site in The Netherlands, representing an early-stage development, and the Munich geothermal project in Germany. The chapter also discusses the limitations of available resistivity and seismic data, and presents the methodologies adopted for modelling and monitoring. These include frequency-domain controlled-source electromagnetic (CSEM) modelling for feasibility assessment at the Delft site, and deterministic full waveform inversion (FWI) applied to DAS and geophone VSP data collected at the Munich site. Modelling assumptions, numerical techniques, and inversion strategies—the Gauss-Newton method—are mentioned. The chapter also highlights how simplifications and data constraints influence model accuracy in both EM and seismic approaches.

Chapter 3 presents a feasibility study on the application of the CSEM method to monitor low-enthalpy geothermal reservoirs, with a specific focus on the TU Delft campus geothermal project. This chapter details the geological setting, modeling approaches, and the effects of source-injection-borehole offsets. In addition, it discusses the impact of temperature variations on electromagnetic responses and investigates potential sources of error, including recording noise, survey repeatability issues, near-surface temperature

changes, and casing effects. The chapter concludes with a discussion on the limitations and practical considerations of implementing CSEM in real-world geothermal monitoring.

Chapter 4 shows seismic monitoring using an advanced FWI approach to reconstruct P-wave velocity and impedance models for the Munich geothermal reservoir. This chapter introduces a novel approach that combines conventional FWI with temporal phase resemblance to enhance sensitivity to impedance changes. The methodology, synthetic validation, and field data application are discussed in detail, followed by an evaluation of the improvements in resolution and accuracy compared to traditional seismic imaging techniques.

In Chapter 5 the use of DAS and its comparison with conventional geophone-based measurements in a vertical seismic profile (VSP) configuration is investigated. This chapter presents a case study from Munich, Germany, analyzing the capabilities of FWI on DAS data from a fibre installed within a casing to capture effects of the seismic wave propagation from the waveforms and the potential to characterize geothermal reservoirs. The advantages and limitations of DAS systems in terms of data quality, spatial coverage, and operational feasibility are critically assessed.

The thesis is concluded in Chapter 6 with a summary of the key findings, their implications for geothermal reservoir monitoring, and potential directions for future research. The conclusions highlight the contributions of this study to the field of geophysical reservoir monitoring and provide recommendations for the integration of CSEM, seismic FWI, and DAS technologies in geothermal energy development.

References

Aljubran, M. J. and Horne, R. N. (2024). Power supply characterization of baseload and flexible enhanced geothermal systems. Scientific reports, 14(1):17619.

Bödvarsson, G. S. and Tsang, C. F. (1982). Injection and thermal breakthrough in fractured geothermal reservoirs. Journal of Geophysical Research: Solid Earth, 87(B2):1031–1048.

Buselli, G. and Lu, K. (2001). Groundwater contamination monitoring with multichannel electrical and electromagnetic methods. Journal of Applied Geophysics, 48(1):11–23.

Chandrasekharam, D. and Bundschuh, J. (2008). Low-enthalpy geothermal resources for power generation. CRC Press.

Clauser, C. (2009). Heat transport processes in the Earth's crust. Surveys in Geophysics, 30(3):163–191.

References

Constable, S. (2010). Ten years of marine CSEM for hydrocarbon exploration. Geophysics, 75(5):75A67–75A81.

Constable, S. (2013). Instrumentation for marine magnetotelluric and controlled source electromagnetic sounding. Geophysical Prospecting, 61:505–532.

Crooijmans, R. A., Willems, C. J., Nick, H. M., and Bruhn, D. (2016). The influence of facies heterogeneity on the doublet performance in low-enthalpy geothermal sedimentary reservoirs. Geothermics, 64:209–219.

Day-Lewis, F. D., Slater, L. D., Robinson, J., Johnson, C. D., Terry, N., and Werkema, D. (2017). An overview of geophysical technologies appropriate for characterization and monitoring at fractured-rock sites. Journal of environmental management, 204:709–720.

Diaz, A. R., Kaya, E., and Zarrouk, S. J. (2016). Reinjection in geothermal fields- A worldwide review update. Renewable and Sustainable Energy Reviews, 53:105–162.

Doherty, T. J. and Clayton, S. (2011). The psychological impacts of global climate change. American Psychologist, 66(4):265.

Edwards, B., Kraft, T., Cauzzi, C., Kästli, P., and Wiemer, S. (2015). Seismic monitoring and analysis of deep geothermal projects in St Gallen and Basel, Switzerland. Geophysical Journal International, 201(2):1022–1039.

Ellabban, O., Abu-Rub, H., and Blaabjerg, F. (2014). Renewable energy resources: Current status, future prospects and their enabling technology. Renewable and Sustainable Energy Reviews, 39:748–764.

Etkins, R. and Epstein, E. S. (1982). The rise of global mean sea level as an indication of climate change. Science, 215(4530):287–289.

Evans, K. F., Zappone, A., Kraft, T., Deichmann, N., and Moia, F. (2012). A survey of the induced seismic responses to fluid injection in geothermal and CO2 reservoirs in Europe. Geothermics, 41:30–54.

Fadel, M., Reinecker, J., Bruss, D., and Moeck, I. (2022). Causes of a premature thermal breakthrough of a hydrothermal project in Germany. Geothermics, 105:102523.

Fanchi, J. R. (2005). Principles of applied reservoir simulation. Elsevier.

Freifeld, B. M., Daley, T. M., Hovorka, S. D., Henninges, J., Underschultz, J., and Sharma, S. (2009). Recent advances in well-based monitoring of CO2 sequestration. Energy Procedia, 1(1):2277–2284.

Fridleifsson, I. B. (2001). Geothermal energy for the benefit of the people. Renewable and Sustainable Energy Reviews, 5(3):299–312.

Fridleifsson, I. B. (2003). Status of geothermal energy amongst the world's energy sources. Geothermics, 32(4-6):379–388.

Gan, Q. and Elsworth, D. (2014). Analysis of fluid injection-induced fault reactivation and seismic slip in geothermal reservoirs. Journal of Geophysical Research: Solid Earth, 119(4):3340–3353.

Jansen, J.-D., Douma, S., Brouwer, D. R., Van den Hof, P., Bosgra, O., and Heemink, A. (2009). Closed-loop reservoir management. In SPE Reservoir Simulation Conference, pages SPE–119098. SPE.

Jeanne, P., Rutqvist, J., Dobson, P. F., Walters, M., Hartline, C., and Garcia, J. (2014). The impacts of mechanical stress transfers caused by hydromechanical and thermal processes on fault stability during hydraulic stimulation in a deep geothermal reservoir. International Journal of Rock Mechanics and Mining Sciences, 72:149–163.

Karl, T. R. and Trenberth, K. E. (2003). Modern global climate change. Science, 302(5651):1719–1723.

Ledley, T. S., Sundquist, E. T., Schwartz, S. E., Hall, D. K., Fellows, J. D., and Killeen, T. L. (1999). Climate change and greenhouse gases. Eos, Transactions American Geophysical Union, 80(39):453–458.

Legarth, B., Tischner, T., and Huenges, E. (2003). Stimulation experiments in sedimentary, low-enthalpy reservoirs for geothermal power generation, Germany. Geothermics, 32(4-6):487–495.

Llera, F. J., Sato, M., Nakatsuka, K., and Yokoyama, H. (1990). Temperature dependence of the electrical resistivity of water-saturated rocks. Geophysics, 55(5):576–585.

Markard, J. (2018). The next phase of the energy transition and its implications for research and policy. Nature Energy, 3(8):628–633.

Marsden, S., Ramey, H., and Sanyal, S. (1973). The effect of temperature on electrical resistivity of porous media. The Log Analyst, 14(02).

Martín-Gamboa, M., Iribarren, D., and Dufour, J. (2015). On the environmental suitability of high-and low-enthalpy geothermal systems. Geothermics, 53:27–37.

Martin III, R. J. (1972). Time-dependent crack growth in quartz and its application to the creep of rocks. Journal of Geophysical Research, 77(8):1406–1419.

References

McMichael, A. J. and Haines, A. (1997). Global climate change: the potential effects on health. Bmj, 315(7111):805–809.

Mestayer, J., Cox, B., Wills, P., Kiyashchenko, D., Lopez, J., Costello, M., Bourne, S., Ugueto, G., Lupton, R., Solano, G., and Hill, D. (2011). Field trials of distributed acoustic sensing for geophysical monitoring. In SEG Technical Program Expanded Abstracts 2011, pages 4253–4257. Society of Exploration Geophysicists.

Michener, W. K., Blood, E. R., Bildstein, K. L., Brinson, M. M., and Gardner, L. R. (1997). Climate change, hurricanes and tropical storms, and rising sea level in coastal wetlands. Ecological Applications, 7(3):770–801.

Moeck, I. S. (2014). Catalog of geothermal play types based on geologic controls. Renewable and Sustainable Energy Reviews, 37:867–882.

Muffler, P. and Cataldi, R. (1978). Methods for regional assessment of geothermal resources. Geothermics, 7(2-4):53–89.

Munoz, G. (2014). Exploring for geothermal resources with electromagnetic methods. Surveys in Geophysics, 35:101–122.

Newman, G. A., Commer, M., and Carazzone, J. J. (2010). Imaging CSEM data in the presence of electrical anisotropy. Geophysics, 75(2):F51–F61.

Pandey, S., Vishal, V., and Chaudhuri, A. (2018). Geothermal reservoir modeling in a coupled thermo-hydro-mechanical-chemical approach: A review. Earth-Science Reviews, 185:1157–1169.

Patidar, A. K., Joshi, D., Dristant, U., and Choudhury, T. (2022). A review of tracer testing techniques in porous media specially attributed to the oil and gas industry. Journal of Petroleum Exploration and Production Technology, 12(12):3339–3356.

Poulsen, S., Balling, N., and Nielsen, S. (2015). A parametric study of the thermal recharge of low enthalpy geothermal reservoirs. Geothermics, 53:464–478.

Pruess, K. and Bodvarsson, G. (1984). Thermal effects of reinjection in geothermal reservoirs with major vertical fractures. Journal of Petroleum Technology, 36(09):1567–1578.

Ren, Y., Kong, Y., Pang, Z., and Wang, J. (2023). A comprehensive review of tracer tests in enhanced geothermal systems. Renewable and Sustainable Energy Reviews, 182:113393.

Rost, S. and Thomas, C. (2002). Array seismology: Methods and applications. Reviews of Geophysics, 40(3):2–1–2–27.

Saeid, S., Al-Khoury, R., Nick, H. M., and Hicks, M. A. (2015). A prototype design model for deep low-enthalpy hydrothermal systems. Renewable Energy, 77:408–422.

Sanni, M., Abbad, M., Kokal, S., Ali, R., Zefzafy, I., Hartvig, S., and Huseby, O. (2017). A field case study of an interwell gas tracer test for GAS-EOR monitoring. In Abu Dhabi International Petroleum Exhibition and Conference, page D031S081R004. SPE.

Saputelli, L., Nikolaou, M., and Economides, M. (2006). Real-time reservoir management: A multiscale adaptive optimization and control approach. Computational Geosciences, 10:61–96.

Short, F. T. and Neckles, H. A. (1999). The effects of global climate change on seagrasses. Aquatic Botany, 63(3-4):169–196.

Smith, R. and Knight, R. (2019). Modeling land subsidence using InSAR and airborne electromagnetic data. Water Resources Research, 55(4):2801–2819.

Stummer, P., Maurer, H., and Green, A. G. (2004). Experimental design: Electrical resistivity data sets that provide optimum subsurface information. Geophysics, 69(1):120–139.

Todd, M., O'dell, P., and Hirasaki, G. (1972). Methods for increased accuracy in numerical reservoir simulators. Society of Petroleum Engineers Journal, 12(06):515–530.

Tomac, I. and Sauter, M. (2018). A review on challenges in the assessment of geomechanical rock performance for deep geothermal reservoir development. Renewable and Sustainable Energy Reviews, 82:3972–3980.

Turcotte, D. L. and Schubert, G. (2002). Geodynamics. Cambridge University Press.

Twidell, John (2021). Renewable energy resources. Routledge.

Uhlemann, S., Chambers, J., Hagedorn, S., Maurer, H., Wilkinson, P., Dijkstra, T., Dashwood, B., Merritt, A., and Gunn, D. (2015). Structurally constrained 4D ERT monitoring to image hydrological processes leading to landslide reactivation. In Near Surface Geoscience 2015-21st European Meeting of Environmental and Engineering Geophysics, volume 2015, pages 1–5. European Association of Geoscientists & Engineers.

Um, E. S. and Alumbaugh, D. L. (2007). On the physics of the marine controlled-source electromagnetic method. Geophysics, 72(2):WA13–WA26.

References

Uribe-Patino, J., Alzate-Espinosa, G., and Arbelaez-Londono, A. (2017). Geomechanical aspects of reservoir thermal alteration: A literature review. Journal of Petroleum Science and Engineering, 152:250–266.

Verliac, M. and Le Calvez, J. (2021). Microseismic monitoring for reliable CO2 injection and storage—Geophysical modeling challenges and opportunities. The Leading Edge, 40(6):418–423.

Vozoff, K. (1980). Electromagnetic methods in applied geophysics. Geophysical Surveys, 4(1):9–29.

Warner, M., Ratcliffe, A., Nangoo, T., Morgan, J., Umpleby, A., Shah, N., Vinje, V., Štekl, I., Guasch, L., Win, C., and Conroy, G. (2013). Anisotropic 3D full-waveform inversion. Geophysics, 78(2):R59–R80.

Weinbrandt, R., Ramey Jr, H., and Casse, F. (1975). The effect of temperature on relative and absolute permeability of sandstones. Society of Petroleum Engineers Journal, 15(05):376–384.

Wu, G., Wang, Y., Swift, G., and Chen, J. (2013). Laboratory investigation of the effects of temperature on the mechanical properties of sandstone. Geotechnical and Geological Engineering, 31:809–816.

Yoro, K. O. and Daramola, M. O. (2020). CO2 emission sources, greenhouse gases, and the global warming effect. In Advances in carbon capture, pages 3–28. Elsevier.

Zang, A., Oye, V., Jousset, P., Deichmann, N., Gritto, R., McGarr, A., Majer, E., and Bruhn, D. (2014). Analysis of induced seismicity in geothermal reservoirs–An overview. Geothermics, 52:6–21.

Zhang, W., Sun, Q., Hao, S., Geng, J., and Lv, C. (2016). Experimental study on the variation of physical and mechanical properties of rock after high temperature treatment. Applied Thermal Engineering, 98:1297–1304.

Zumberge, M., Alnes, H., Eiken, O., Sasagawa, G., and Stenvold, T. (2008). Precision of seafloor gravity and pressure measurements for reservoir monitoring. Geophysics, 73(6):WA133–WA141.

Chapter 2

Study Areas and Methodologies

2.1 Study areas and data limitations

The research in this thesis focuses on two geothermal projects in the Netherlands and Germany. The two projects share significant similarities for being inner-city ones and having low-enthalpy reservoirs. These reservoirs are at similar depths and have comparable thicknesses. They also have similar temperature contrasts between the geothermal fluids produced and returned. However, the geological settings are not the same. More details about these projects are as follows:

- **Delft campus geothermal project**: A developing geothermal site located at Delft in the Netherlands, designed to provide sustainable heating to Delft University of Technology (TU Delft) and surrounding areas, visit: https://geothermiedelft.nl/. This project represents an early-stage geothermal development with opportunities to implement and validate novel geophysical monitoring techniques from the outset (Vardon et al., 2024). In this thesis, the feasibility of CSEM monitoring will be assessed for this setting.

- **Munich geothermal project**: A well-established geothermal district heating system in the Bavarian Molasse Basin, supplying heat to the city of Munich, see Section 4.2. The Munich project provides an ideal case study for evaluating the performance of seismic FWI in an operational geothermal reservoir with an ongoing heat extraction, where conventional geophone and novel DAS VSP data are available. This site allows for the validation of advanced FWI techniques in a real-world environment.

Limitations of resistivity models for the Delft geothermal site

The electric resistivity model related to the Delft geothermal site has several limitations.

Although the lithological layers below the Delft campus are known, the resistivity structure at this site remains unknown. Therefore, a resistivity model of the Delft campus was built with logging information of the same lithologies measured in other parts of the Netherlands. Furthermore, the logs were not corrected for the conditions of the borehole fluids given the uncertainty about them. Lastly, heterogeneous three-dimensional (3D) models that capture the complexity of both the overburden and the low-enthalpy reservoir are not available. Overall, the feasibility of CSEM monitoring of the Delft campus reservoir is conducted with a simplified resistivity model.

Limitations of data from the Munich geothermal site

The Munich field data were collected in wells with 3D geometry for vertical sources. Two source positions were deployed; the first source position is about 180 m away from the well head, and the second source position is about 1100 m away. At only two positions, the generated wavefield does not adequately illuminate the subsurface regions, including the reservoir, surrounding the wells, restricting our ability to perform full seismic 3D FWI. The Munich field data also has a limited angular aperture to resolve structural dips such as tilted layers.

Another limitation is the absence of time-lapse data, which restricts the ability to monitor temperature changes in the reservoir over time. Acquiring multiple datasets over extended periods is costly and logistically complex. Therefore, we demonstrate the ability of the developed FWI approach for seismic monitoring of heat production by using synthetic time lapse data. This is an oversimplification of real-world scenarios with change having limited spans and are affected by heterogeneous fluid flow patterns.

A further limitation relates to DAS installation issues that affect data quality. DAS relies on fiber-optic cables to measure strain rates along the cable axis due to seismic signal. At the Munich geothermal site, the DAS cable was lowered into a deviated borehole with gravity being the main coupling factor. Hence, the cable was susceptible to resonance and incoherent contact with the casing (and therefore formations). Moreover, the quality of these measurements is affected by signal attenuation, amplified noise and artifacts, and instrument noise. These issues degraded the SNR ratio of the DAS VSP data.

2.2 Study methodology and assumptions: CSEM

2.2.1 Modelling of EM fields

The EM signal can be transmitted at a specific frequency, called frequency-domain EM (FDEM), or as a transient signal, called time-domain EM (TDEM) (Weiss, 2007; Di et al., 2020). In FDEM, the amplitude and phase of monochromatic or single-frequency/sinusoidal

fields are measured. In TDEM, transient current is injected into the ground, and the decay of induced eddy currents is recorded over time (Nabighian, 1979; Strack et al., 1992). As TDEM requires the modelling of many frequencies as of computationally more expensive the modelling (Werthmüller, 2017). Furthermore, the steady-state nature of the former simplifies data analysis and interpretation. Because of these advantages, we chose to study the feasibility of CSEM monitoring of the Delft campus geothermal project with the FDEM technique.

FDEM fields can be generated by electric or magnetic field sources, and their potentials recorded by electric- or magnetic-field receivers. Electric dipoles generate strong signals that effectively propagate throughout the depth range of the low-enthalpy reservoirs that we will study. With electric-field receivers, these signals might enable the detection of small variations in resistivity as indication of temperature changes. Electric-field sources and receivers would be more suitable for time-lapse CSEM monitoring (Key, 2009). To determine the electric field response at a point due to an external source of electric field, two Maxwell's equations are coupled—Ampère's law and Faraday's law. Assuming a harmonic time dependence of the form $\mathrm{e}^{-i\omega t}$, these are given in the frequency domain as Zhdanov (2009); Chew et al. (2022)

$$\nabla \times \mathbf{H}(\mathbf{x}) = -i\omega \mathbf{K}(\mathbf{x}) \cdot \mathbf{E}(\mathbf{x}) + \mathbf{C}(\mathbf{x}) \cdot \mathbf{E}(\mathbf{x}) + \mathbf{J}^{(e)}(\mathbf{x}), \qquad (2.1)$$

and

$$\nabla \times \mathbf{E}(\mathbf{x}) = i\omega \mathbf{M}_p(\mathbf{x}) \cdot \mathbf{H}(\mathbf{x}), \qquad (2.2)$$

where i is the imaginary unit, ω is the angular frequency, t is time, $\nabla\times$ is the divergence operator, $\mathbf{H}$ is the magnetic-field strength, $\mathbf{K}$ is the dielectric permittivity, $\mathbf{E}$ is the electric-field intensity, $\mathbf{C}$ is the electrical conductivity, $\mathbf{J}^{(e)}$ is the electric current due to the external source, and $\mathbf{M}_p$ is the magnetic permeability. The combination of these two equations results in the general form (Jakobsen and Tveit, 2018),

$$\left[\nabla \times \nabla \times -i\omega \mathbf{M}_p(\mathbf{x})\mathbf{C}(\mathbf{x}) \cdot -\omega^2 \mathbf{M}_p(\mathbf{x})\mathbf{K}(\mathbf{x}) \cdot \right] \mathbf{E}(\mathbf{x}) = i\omega \mathbf{M}_p(\mathbf{x}) \cdot \mathbf{J}^{(e)}(\mathbf{x}). \qquad (2.3)$$

Eq. 2.3 can be reformulated as an integral equation, which is then solved to compute the electromagnetic field within a subsurface Earth model (Eltayieb, 2020). Section 2.3 outlines the computational methods used to evaluate the CSEM response with the aim of studying the feasibility of CSEM for monitoring low-enthalpy reservoirs.

2.2.2 Assumptions

A few assumptions related to the models have been made for the FDEM modelling: (1) A layered resistivity model was used to represent the subsurface of the Delft campus. (2) A

homogeneous and isotropic reservoir model is assumed, where the resistivity was assumed to vary equally throughout a rounded reservoir volume. This is clearly a simplification of the real-world scenario and may affect the validity of the modelling results. (3) temperature variations have not been determined based on reservoir modelling, which is important to capture dynamic geothermal processes. These variations should have a gradual transition from the cooled to the warm areas. Instead of integrating a fully coupled CSEM and THM reservoir model, this research approximates time-lapse effects through variations of increasing volume with a sharp transition.

2.3 Study methodology and assumptions: seismic FWI

2.3.1 Modelling of seismic wave fields

Seismic FWI is a powerful technique for reconstructing subsurface velocities (Sears et al., 2008) and impedances (Baeten et al., 2013). While most FWI applications to date have focused on surface-based seismic data for characterization (Vigh et al., 2014; Benfield et al., 2017; Mirzanejad and Tran, 2019; Sedova et al., 2019) and monitoring (Zhang et al., 2013; Hicks et al., 2016), its extension to borehole environments, such as VSP, improves resolution in the wellbore region (Owusu et al., 2015; Egorov et al., 2017, 2018; Pan et al., 2018; Takougang et al., 2020). FWI depends on iteratively refining velocity and impedance models to minimize misfit between observed and calculated waveforms (Operto et al., 2013). Hence, it is necessary to model seismic waveforms accurately.

Seismic waveforms are governed by the fundamental laws of motion and deformation in elastic continua. One of these laws is the equation of motion (Newton's second law) (Kane and Wang, 1965),

$$\rho\frac{\partial^2 \mathbf{u}}{\partial t^2} = \nabla \cdot \boldsymbol{\sigma} + \mathbf{f}, \tag{2.4}$$

where ρ is the mass density, $\mathbf{u}$ is the displacement vector, $\boldsymbol{\sigma}$ is the stress tensor and $\mathbf{f}$ represents body forces (seismic sources). The other fundamental law is Hooke's law for isotropic materials (Thompson, 1926),

$$\boldsymbol{\sigma} = \lambda\left(\nabla \cdot \mathbf{u}\right)\mathbf{I} + 2\mu\boldsymbol{\varepsilon}, \tag{2.5}$$

where $\boldsymbol{\varepsilon}$ is the strain tensor, λ and μ are the Lamé parameters and $\mathbf{I}$ is the identity tensor. Notice that we did not include any source terms in this equation since we only deal with body-force sources in this thesis.

In order to arrive at the elastic wave equation, Eq. 2.5 first needs to be substituted into Eq. 2.4. Then, using the compact tensor form $\boldsymbol{\varepsilon} = \frac{1}{2}\left(\nabla\mathbf{u} + \left(\nabla\mathbf{u}\right)^{\top}\right)$ where $\nabla\mathbf{u}$ stands for

a matrix with the partial derivatives of the three components of the displacement vector $\mathbf{u}$, $\boldsymbol{\varepsilon}$ is replaced by $\mathbf{u}$ and vector-calculus identities allow further simplification to arrive at our desired result:

$$(\lambda + 2\mu)\nabla(\nabla \cdot \mathbf{u}) - \mu\nabla \times \nabla \times \mathbf{u} - \rho\partial_t^2 \mathbf{u} = \mathbf{f}. \tag{2.6}$$

In the FWI studies in this thesis, ground displacement is considered at arbitrary receiver locations in a horizontally stratified (axissymmetric) elastic half-space, excited by a vertical point force at the surface. Because of these assumptions, it is easier to evaluate the solution in the frequency–horizontal (radial) wavenumber (ω–k_r) domain so polar coordinates are used in the horizontal plane.

First, the forward temporal Fourier transform is applied to Eq. 2.6,

$$\hat{\mathbf{u}}(r, z, \omega) = \int_{-\infty}^{\infty} \mathbf{u}(r, z, t)\, e^{-i\omega t}\, dt, \tag{2.7}$$

converting it from the time to the frequency domain so that ∂_t^2 becomes $-\omega^2$. This is followed by forward spatial Fourier transforms in x and y that can be written as a forward Hankel transform to the k_r–ω domain. The new formulation reduces the problem to solving for the displacement analytically, which is particularly well suited for horizontally layered elastic media (Haskell, 1964).

Next, the displacement field can be written in terms of potentials within each homogeneous layer as $\mathbf{u} = \nabla\phi + \nabla \times (\psi\mathbf{e}_\theta)$, where $\mathbf{e}_\theta$ stands for the azimuthal direction in axis-symmetric 3D geometry (cylindrical coordinates), which simplifies the computation of the curl to be in the $r - z$ plane (Eringer, 1974; Bian et al., 2021). The potential ϕ has zero curl (irrotational) and $\psi\mathbf{e}_\theta$ has zero divergence (Harkrider, 1976). The scalar potential ϕ is the one for compressional waves (P-waves) which describes longitudinal motion and is associated with volume changes (dilatation) in the medium. The scalar potential ψ is the one for shear waves (S-waves) which describes the transverse motion and is associated with shearing in the medium.

In each layer, the total wave field is a superposition of up- and down-going plane P- and S-waves traveling along an azimuthal direction $\mathbf{e}_\theta$ and are given by (Haskell, 1953),

$$\tilde{\phi}(k_r, z, \omega) = A^+ e^{ik_z^{(P)}z} + A^- e^{-ik_z^{(P)}z}, \tag{2.8}$$

$$\tilde{\psi}(k_r, z, \omega) = B^+ e^{ik_z^{(S)}z} + B^- e^{-ik_z^{(S)}z}, \tag{2.9}$$

where $k_z^{(P)}$ and $k_z^{(S)}$ are the vertical wavenumbers ($k_z^{(P,S)} = [\omega^2/c_{P,S}^2 - k_r^2]^{1/2}$) for the P- and S-wave, respectively. The amplitude coefficients $A^\pm$ and $B^\pm$ are determined by satisfying

the boundary conditions, i.e. continuity of displacement and stress at all interfaces.

For the depth-dependent solution, the classical propagator matrix method introduced by Haskell (1953) is used. This method relates the field variables across interfaces recursively, using compact matrix relations to track up- and down-going wave amplitudes through the stratified half-space. It allows for efficient and memory-conserving computation of the layered response. The linear system of equations constructed via the propagator formalism relates the displacement–stress state at the surface and bottom of each layer through (Haskell, 1964)

$$\mathbf{u}_{m-1}(k_r) = \mathbf{P}_m(k_r) \cdot \mathbf{u}_m(k_r), \tag{2.10}$$

where $\mathbf{u}_m$ is a vector of displacement and stress components, and $\mathbf{P}_m$ is the propagator matrix for layer m, whose formulation, evolution and implementation have been provided by Meehan (2018). The complete system is assembled recursively across all layers, incorporating source terms and receiver characteristics at the appropriate depths.

Once these solutions are established in the ω–k_r domain, the frequency-domain displacement field can again be formulated as a Hankel-type integral (Hudson, 1969). In numerical computation, the radial-wavenumber integral in this Hankel-type integral is discretized and truncated appropriately. Quadrature rules are applied to ensure numerical stability and computational efficiency. Due to the presence of oscillatory integrands and poles near the real axis (related to surface and guided modes), complex contour integration is employed, as described by Wang and Herrmann (1980). This deformation into the complex plane circumvents singularities and enhances the convergence of the integral.

Finally, the frequency-domain solution is inverse-Fourier transformed by using standard integration techniques to efficiently obtain time-domain waveforms (Brigham, 1988):

$$\mathbf{u}(r, z, t) = \frac{1}{2\pi} \int_{-\infty}^{\infty} \mathbf{u}(r, z, \omega) e^{-i\omega t} \, d\omega. \tag{2.11}$$

The approach outlined above allows simulation of broadband seismic responses at arbitrary receiver locations in layered elastic media, incorporating full-wave phenomena including body waves, surface waves, and reverberations.

In this thesis, we assume a lossless medium when calculating seismic waveforms. The Earth is known to act as a low-pass filter, meaning that high frequencies are affected more by attenuation (quality factor) than low frequencies (Yilmaz, 2001). Due to the lack of prior information on the quality factor or a reliable method to calculate it, a perfectly elastic medium is assumed in waveform modelling. Even though seismic waves suffer various degrees of anelastic attenuation as they propagate through different subsurface media, high frequencies are generally more impacted than low frequencies. Hence, such an

assumption would be valid on waveforms calculated in the low frequency band of interest , Section 4.5.

2.3.2 Inversion approach

For the inversion part, there are two approaches for optimizing a fit between observed and synthetic data, namely a statistical and a deterministic one (Sen and Stoffa, 2013). Statistical techniques use probabilistic frameworks to explore multiple possible subsurface models and quantify uncertainty (Grana et al., 2022). Methods such as genetic algorithms, Bayesian inference and Markov chain Monte Carlo (MCMC) consider a range of models rather than converging to a single solution (Sambridge and Drijkoningen, 1992; Gouveia and Scales, 1998; Malinverno, 2002). These approaches are particularly useful in cases with limited data coverage or high uncertainty, as they provide a probabilistic estimate of the subsurface properties rather than a single deterministic solution (Veeken et al., 2004). However, statistical techniques are computationally expensive because they require a large number of forward waveform modelling to adequately sample the solution space (Laloy et al., 2018, 2019).

Deterministic optimization techniques rely on a gradient to guide adjustments in the model parameters (Floudas, 2013). For seismic monitoring, velocity and/or impedance models are estimated from occasionally repeated surveys over the geothermal reservoir. In this context, deterministic FWI offers a viable tool because it provides an optimal baseline and monitor models with reasonable computational cost, for example, resources and time (Lelièvre et al., 2009). The difference between these models should help to track the occurring changes qualitatively and quantitatively. Statistical FWI gives an ensemble of models when applied to a data set of each survey, which significantly complicates the description of reservoir changes. The focus here is on capturing the kinematic and structural changes between successive surveys with maximum spatial resolution and physical interpretability. Therefore, we prefer deterministic FWI approaches.

Deterministic approaches such as conjugate-gradient, quasi-Newton, and Gauss-Newton are local optimizers (Cavazzuti, 2012), therefore require a good starting model. The conjugate-gradient method improves upon the steepest decent by ensuring that each model update step is conjugate to the previous step, which prevents erratic fluctuation in the search space (Shewchuk et al., 1994). Although the conjugate-gradient method is computationally less intensive, it can suffer from slower convergence compared to Newton-type methods (Dai et al., 2000; Homeier, 2005). Quasi-Newton methods such as the limited-memory Broyden-Fletcher-Goldgarb-Shanno (L-BFGS) ensure fast convergence by conditioning the gradient with an approximate Hessian matrix that is computed using past gradient information instead of computing it directly (Liu and Nocedal, 1989). However,

they require fine-tuning of step size and memory parameters, which can be a difficult task (Métivier et al., 2017). The Gauss-Newton method approximates the Hessian matrix by neglecting the second-order derivative terms (Pratt et al., 1998). This offers more accurate model updates and better handling of weak nonlinearities at early iterations in FWI (Dennis Jr and Schnabel, 1996). Ultimately, we deploy the Gauss-Newton method for the FWI inversion scheme. More details on this FWI scheme are given in Sections 4.3 and 5.3.

2.3.3 Assumptions

The assumptions for the modelling in FWI are imposed by the data limitations of the case study at the Munich geothermal site. Due to the very limited source coverage of the VSP data, I use 3D modelling with allowing heterogeneities in only one dimension (1D), which will not fully represent the complex 3D nature of the subsurface of the Munich geothermal site. In reality, reservoir heterogeneities and fluid flow patterns are inherently three-dimensional, making lower-dimensional models potentially insufficient for precise reservoir characterization and monitoring. However, the FWI approaches developed for high resolution 1D models could be extended to higher dimensions. These 1D models also serve as initial models for the FWI of subsurface media with lateral heterogeneities.

References

Baeten, G., de Maag, J. W., Plessix, R.-E., Klaassen, R., Qureshi, T., Kleemeyer, M., ten Kroode, F., and Rujie, Z. (2013). The use of low frequencies in a full-waveform inversion and impedance inversion land seismic case study. Geophysical Prospecting, 61(4):701–711.

Benfield, N., Rambaran, V., Dowlath, J., Sinclair, T., Evans, M., Richardson, J., Ratcliffe, A., and Irving, A. (2017). Extracting geologic information directly from high-resolution full-waveform inversion velocity models—A case study from offshore Trinidad. The Leading Edge, 36(1):67–74.

Bian, C., Wang, J., Huang, B., Xie, L., Yi, L., Yuan, L., Li, H., and Tian, Y. (2021). An analysis of axisymmetric Sezawa waves in elastic solids. Physica Scripta, 96(12):125272.

Brigham, E. O. (1988). The fast Fourier transform and its applications. Prentice-Hall, Inc.

Cavazzuti, M. (2012). Deterministic optimization. In Optimization methods: From theory to design scientific and technological aspects in mechanics, pages 77–102. Springer.

Chew, W., Tong, M.-S., et al. (2022). Integral equation methods for electromagnetic and elastic waves. Springer Nature.

Dai, Y., Han, J., Liu, G., Sun, D., Yin, H., and Yuan, Y.-x. (2000). Convergence properties of nonlinear conjugate gradient methods. SIAM Journal on Optimization, 10(2):345–358.

Dennis Jr, J. E. and Schnabel, R. B. (1996). Numerical methods for unconstrained optimization and nonlinear equations. SIAM.

Di, Q., Xue, G., Yin, C., and Li, X. (2020). New methods of controlled-source electromagnetic detection in China. Science China Earth Sciences, 63:1268–1277.

Egorov, A., Correa, J., Bóna, A., Pevzner, R., Tertyshnikov, K., Glubokovskikh, S., Puzyrev, V., and Gurevich, B. (2018). Elastic full-waveform inversion of vertical seismic profile data acquired with distributed acoustic sensors. Geophysics, 83(3):R273–R281.

Egorov, A., Pevzner, R., Bóna, A., Glubokovskikh, S., Puzyrev, V., Tertyshnikov, K., and Gurevich, B. (2017). Time-lapse full waveform inversion of vertical seismic profile data: Workflow and application to the CO2CRC Otway project. Geophysical Research Letters, 44(14):7211–7218.

Eltayieb, M. (2020). Integral Equation Methods for CSEM Modeling, Inversion and Time-lapse Studies. Master's Thesis, University of Bergen, Bergen, Norway. Department of Earth Science.

Eringer, A. (1974). Elastodynamics, volume 2. Рипол Классик.

Floudas, C. A. (2013). Deterministic global optimization: theory, methods and applications, volume 37. Springer Science & Business Media.

Gouveia, W. P. and Scales, J. A. (1998). Bayesian seismic waveform inversion: Parameter estimation and uncertainty analysis. Journal of Geophysical Research: Solid Earth, 103(B2):2759–2779.

Grana, D., Azevedo, L., De Figueiredo, L., Connolly, P., and Mukerji, T. (2022). Probabilistic inversion of seismic data for reservoir petrophysical characterization: Review and examples. Geophysics, 87(5):M199–M216.

Harkrider, D. G. (1976). Potentials and displacements for two theoretical seismic sources. Geophysical Journal International, 47(1):97–133.

Haskell, N. (1964). Radiation pattern of surface waves from point sources in a multi-layered medium. Bulletin of the Seismological Society of America, 54(1):377–393.

References

Haskell, N. A. (1953). The dispersion of surface waves on multilayered media. Bulletin of the Seismological Society of America, 43(1):17–34.

Hicks, E., Hoeber, H., Houbiers, M., Lescoffit, S. P., Ratcliffe, A., and Vinje, V. (2016). Time-lapse full-waveform inversion as a reservoir-monitoring tool—A North Sea case study. The Leading Edge, 35(10):850–858.

Homeier, H. H. (2005). On Newton-type methods with cubic convergence. Journal of Computational and Applied Mathematics, 176(2):425–432.

Hudson, J. (1969). A quantitative evaluation of seismic signals at teleseismic distances—I radiation from point sources. Geophysical Journal International, 18(3):233–249.

Jakobsen, M. and Tveit, S. (2018). Distorted Born iterative T-matrix method for inversion of CSEM data in anisotropic media. Geophysical Journal International, 214(3):1524–1537.

Kane, T. R. and Wang, C. (1965). On the derivation of equations of motion. Journal of the Society for Industrial and Applied Mathematics, 13(2):487–492.

Key, K. (2009). 1D inversion of multicomponent, multifrequency marine CSEM data: Methodology and synthetic studies for resolving thin resistive layers. Geophysics, 74(2):F9–F20.

Laloy, E., Hérault, R., Jacques, D., and Linde, N. (2018). Training-image based geostatistical inversion using a spatial generative adversarial neural network. Water Resources Research, 54(1):381–406.

Laloy, E., Linde, N., Ruffino, C., Hérault, R., Gasso, G., and Jacques, D. (2019). Gradient-based deterministic inversion of geophysical data with generative adversarial networks: is it feasible? Computers & Geosciences, 133:104333.

Lelièvre, P. G., Oldenburg, D. W., and Williams, N. C. (2009). Integrating geological and geophysical data through advanced constrained inversions. Exploration Geophysics, 40(4):334–341.

Liu, D. C. and Nocedal, J. (1989). On the limited memory BFGS method for large scale optimization. Mathematical Programming, 45(1):503–528.

Malinverno, A. (2002). Parsimonious Bayesian Markov chain Monte Carlo inversion in a nonlinear geophysical problem. Geophysical Journal International, 151(3):675–688.

Meehan, T. (2018). Evolution of the propagator matrix method and its implementation in seismology. arXiv preprint arXiv:1801.04635.

Métivier, L., Brossier, R., Operto, S., and Virieux, J. (2017). Full waveform inversion and the truncated Newton method. SIAM Rreview, 59(1):153–195.

Mirzanejad, M. and Tran, K. T. (2019). 3D viscoelastic full waveform inversion of seismic waves for geotechnical site investigation. Soil Dynamics and Earthquake Engineering, 122:67–78.

Nabighian, M. N. (1979). Quasi-static transient response of a conducting half-space—An approximate representation. Geophysics, 44(10):1700–1705.

Operto, S., Gholami, Y., Prieux, V., Ribodetti, A., Brossier, R., Métivier, L., and Virieux, J. (2013). A guided tour of multiparameter full-waveform inversion with multicomponent data: From theory to practice. The Leading Edge, 32(9):1040–1054.

Owusu, J. C., Podgornova, O., Charara, M., Leaney, S., Campbell, A., Ali, S., Borodin, I., Nutt, L., and Menkiti, H. (2015). Anisotropic elastic full-waveform inversion of walkaway vertical seismic profiling data from the Arabian Gulf. Geophysical Prospecting, 64(1):38–53.

Pan, W., Innanen, K. A., and Geng, Y. (2018). Elastic full-waveform inversion and parametrization analysis applied to walk-away vertical seismic profile data for unconventional (heavy oil) reservoir characterization. Geophysical Journal International, 213(3):1934–1968.

Pratt, R. G., Shin, C., and Hick, G. (1998). Gauss–Newton and full Newton methods in frequency–space seismic waveform inversion. Geophysical Journal International, 133(2):341–362.

Sambridge, M. and Drijkoningen, G. (1992). Genetic algorithms in seismic waveform inversion. Geophysical Journal International, 109(2):323–342.

Sears, T. J., Singh, S., and Barton, P. (2008). Elastic full waveform inversion of multicomponent OBC seismic data. Geophysical Prospecting, 56(6):843–862.

Sedova, A., Royle, G., Allemand, T., Lambaré, G., and Hermant, O. (2019). Highfrequency acoustic land full-waveform inversion: A case study from the Sultanate of Oman. First Break, 37(1):75–81.

Sen, M. K. and Stoffa, P. L. (2013). Global optimization methods in geophysical inversion. Cambridge University Press.

Shewchuk, J. R. et al. (1994). An introduction to the conjugate gradient method without the agonizing pain.

References

Strack, K.-M. et al. (1992). Exploration with deep transient electromagnetics, volume 373. Elsevier Amsterdam.

Takougang, E. M. T., Ali, M. Y., Bouzidi, Y., Bouchaala, F., Sultan, A. A., and Mohamed, A. I. (2020). Characterization of a carbonate reservoir using elastic full-waveform inversion of vertical seismic profile data. Geophysical Prospecting, 68(6):1944–1957.

Thompson, J. O. (1926). Hooke's law. Science, 64(1656):298–299.

Vardon, P., Laumann, S., van Esser, B., Ursem, L., van Schravendijk, B., Meleza, L. V., Barnhoorn, A., Abels, H., Vondrak, A., Drijkoningen, G., et al. (2024). End-of-Well Science Programme Report DEL-GT-01 and DEL-GT-02: TU Delft campus geothermal project.

Veeken, P., Silva, D., and M (2004). Seismic inversion methods and some of their constraints. First Break, 22(6).

Vigh, D., Jiao, K., Watts, D., and Sun, D. (2014). Elastic full-waveform inversion application using multicomponent measurements of seismic data collection. Geophysics, 79(2):R63–R77.

Wang, C. Y. and Herrmann, R. B. (1980). A numerical study of P-, SV-, and SH-wave generation in a plane layered medium. Bulletin of the Seismological Society of America, 70(4):1015–1036.

Weiss, C. J. (2007). The fallacy of the "shallow-water problem" in marine CSEM exploration. Geophysics, 72(6):A93–A97.

Werthmüller, D. (2017). An open-source full 3D electromagnetic modeler for 1D VTI media in Python: empymod. Geophysics, 82(6):WB9–WB19.

Yilmaz, Ö. (2001). Seismic data analysis: Processing, inversion, and interpretation of seismic data. Society of exploration geophysicists.

Zhang, F., Juhlin, C., Ivandic, M., and Lüth, S. (2013). Application of seismic full waveform inversion to monitor CO2 injection: Modelling and a real data example from the Ketzin site, Germany. Geophysical Prospecting, 61:284–299.

Zhdanov, M. S. (2009). Geophysical electromagnetic theory and methods, volume 43. Elsevier.

Chapter 3

Feasibility Study of CSEM Method Monitoring

Tracking temperature changes by measuring the resulting resistivity changes inside low-enthalpy reservoirs is crucial to avoid early thermal breakthroughs and maintain sustainable energy production. The controlled-source electromagnetic method (CSEM) allows for the estimation of sub-surface resistivity. However, it has not yet been proven that the CSEM can monitor the subtle resistivity changes typical of low-enthalpy reservoirs. In this chapter, we present a feasibility study considering the CSEM monitoring of 4–8 $\Omega \cdot$m resistivity changes in a deep low-enthalpy reservoir model, as part of the Delft University of Technology (TU Delft) campus geothermal project. We consider the use of a surface-to-borehole CSEM for the detection of resistivity changes in a simplified model of the TU Delft campus reservoir. We investigate the sensitivity of CSEM data to disk-shaped resistivity changes with a radius of 300, 600, 900, or 1200 m at return temperatures equal to 25, 30, $\cdots$, 50 °C. We test the robustness of CSEM monitoring against various undesired effects, such as random noise, survey repeatability errors, and steel-cased wells. The modelled differences in the electric field suggest that they are sufficient for the successful CSEM detection of resistivity changes in the low-enthalpy reservoir. The difference in monitoring data increases when increasing the resistivity change radius from 300 to 1200 m or from 4 to 8 $\Omega \cdot$m. Furthermore, all considered changes lead to differences that would be detectable in CSEM data impacted by undesired effects. The obtained results indicate that the CSEM could be a promising geophysical tool for the monitoring of small resistivity changes in low-enthalpy reservoirs, which would be beneficial for geothermal energy production.

3.1 Introduction

District heating consumes about half of the energy produced worldwide (Pirouti et al., 2013; Mazhar et al., 2018). Most of this energy is generated by burning fossil fuels, which contributes to global warming (European Commission, 2011; Lake et al., 2017). Low-enthalpy reservoirs provide geothermal energy for heating and cooling, both in residential and industrial applications (Chandrasekharam and Bundschuh, 2008). Low-enthalpy energy is renewable energy, which makes it important in the pursuit to mitigate global warming. Low-enthalpy reservoirs are sub-surface layers of water-filled rocks at temperatures below 150 °C (Muffler and Cataldi, 1978; Barbier, 2002; Munoz, 2014). Energy can be produced from these reservoirs by pumping out hot water, extracting the heat, and then re-injecting it at lower temperatures (Martín-Gamboa et al., 2015; Olasolo et al., 2016). The re-injected water spreads around the return well and forms a cold plume (Kaya et al., 2011), which maintains the volume of the geothermal reservoir but leads to a long-term temperature decline (Bödvarsson and Tsang, 1982). The cold plume grows depending on the production rate and, if not managed properly, can result in an early thermal breakthrough, where the cold plume reaches the producing well. As a result, energy production may decrease to a level that is no longer profitable (Stefansson, 1997).

Efficient management of production helps to avoid early thermal breakthroughs, which can be achieved by determining a level of sustainable utilization that can be maintained for many decades (Axelsson et al., 2003, 2005; Poulsen et al., 2015). For this purpose, reservoir simulation is typically used to predict the development of the cold plume in many production scenarios (O'Sullivan et al., 2001). However, uncertainty in the petrophysical characteristics of the reservoir, such as its porosity and permeability, can lead to predictions that differ from actual future production (Wang et al., 2021). Therefore, it is necessary to monitor the cold plume in real-time to calibrate reservoir simulations and predict energy production more accurately. In this chapter, we focus on monitoring the cold plume in the low-enthalpy reservoir of the TU Delft campus geothermal project, which is a well doublet that is under construction (Bruhn et al., 2015).

Geophysical methods, such as seismic and electromagnetic (EM), provide valuable information regarding the physical properties of reservoirs for characterization and monitoring. Seismic methods utilise the elastic structure of the earth (Virieux and Operto, 2009), while EM methods explore the electrical resistivity (Nabighian, 1988, 1991). At a fixed salinity, the electrical resistivity of a fluid filling rock pores is inversely proportional to its temperature (Kaya et al., 2011; Schön, 2015). Therefore, the electrical resistivity of the TU Delft campus reservoir can be expected to increase at a percentage as the temperature decreases. EM techniques, such as electrical resistivity tomography (ERT), magnetotellurics (MT), and the CSEM, are suitable for mapping resistivity changes as an indicator

of the cold plume.

The length of the ERT acquisition profile is normally several times the investigated depth (Balasco et al., 2022). To monitor the deep TU Delft campus reservoir, ERT surveys require an acquisition profile many kilometres deep, which is not feasible. MT can achieve a great depth of investigation by measuring the sub-surface response to naturally occurring EM fields (Chave and Jones, 2012); however, MT measurements suffer from a low signal-to-noise ratio (SNR) in urban environments (Fraser Smith and Coates, 1978; Egbert, 1997), and may not be able to detect small resistivity changes due to variations in MT fields (Abdelfettah et al., 2018). The CSEM relies on artificial sources of EM fields to investigate the electrical resistivity of the sub-surface to a depth of a few kilometres (Constable and Srnka, 2007; Ziolkowski and Slob, 2019). CSEM fields suffer from less variation due to the high repeatability of the source fields, and are characterised by high SNR due to the high source power (Myer et al., 2011). Overall, we purpose CSEM to monitor the resistivity changes in the TU Delft campus geothermal reservoir.

Several configurations can be used to collect CSEM monitoring data, such as surface-to-surface, surface-to-borehole, borehole-to-surface, and/or borehole-to-borehole. The surface-to-surface configuration allows for dense data coverage at relatively low cost. The target reservoir for the TU Delft campus geothermal reservoir lies at such a depth that CSEM fields carrying information about the resistivity change will be below the noise floor when collecting surface-based measurements. Furthermore, deploying the receivers at the surface makes them susceptible to high levels of both natural and anthropogenic noise. In surface-to-borehole and borehole-to-surface configurations, electric fields travel relatively short distances and can be measured with amplitudes above the noise floor. While the surface-to-borehole configuration is theoretically equivalent to the borehole-to-surface, practical applications indicate that the surface-to-borehole configuration offers a relatively higher SNR for two reasons: (1) The ability to achieve large dipole moments with surface sources, and (2) the borehole receivers are located away from EM noise near the surface (Colombo and McNeice, 2013, 2018). The borehole-to-borehole CSEM requires a borehole source, has a limited dipole moment, and only provides two-dimensional (2D) inter-well resistivity information.

In this chapter, we investigate the feasibility of CSEM monitoring for 4–8 $\Omega \cdot$m resistivity changes based on expected temperature differences between 25 and 50 °C in the deep low-enthalpy reservoir model of the TU Delft campus geothermal project. Considering the reasons mentioned above, we chose to use a surface-to-borehole configuration to determine time-lapse electric fields (i.e., fields with temporal intervals). Monitoring this low-enthalpy reservoir is a process that will be carried out over several decades, as the resistivity change is expected to progress laterally. We explore the potential of the

CSEM technique to monitor various lateral resistivity changes inside the TU Delft campus low-enthalpy reservoir. We also test the robustness of the CSEM monitoring of the reservoir against undesired effects, which can distort CSEM data when scattered by the reservoir. These effects include multiplicative random noise, survey repeatability errors, near-surface changes, and the influence of a steel-cased borehole. To date, there has been no investigation on the impact of the high magnetic permeability and the low electrical resistivity of a steel casing on surface-to-borehole CSEM data. Thus, we incorporated the magnetic and electric properties of the steel casing into the model, in order to study its effect on the vertical electric field. Due to the advantages that composite pipes have over steel ones during geothermal operations, composite pipes will replace steel pipes in the near future (Olufemi et al., 2020). To evaluate the effect of the composite casing on the CSEM response, we changed the properties of the casing from those of steel to fibreglass-reinforced epoxy. In general, this chapter details a forward modelling framework suggesting the feasibility of the CSEM monitoring of low-enthalpy reservoirs with distorted time-lapse data.

The remainder of this chapter is structured as follows. In Section 3.2, we give a brief description of the geological and electrical resistivity models of the TU Delft campus subsurface. In Section 3.3, we briefly mention the two CSEM forward-modelling approaches used in this study. In Section 3.4, we explore useful source locations for the CSEM monitoring of the TU Delft campus reservoir with preferential acquisition parameters; namely, the source–receiver setup and the source frequency. In Section 3.5, we assess the feasibility of using a time-lapse CSEM to track the time-lapse resistivity changes resulting from different return temperatures. In Section 3.6, we assess the robustness of CSEM monitoring when undesired effects corrupt the time-lapse signal. In Section 3.7, we discuss the merits and limitations of this feasibility study. In Section 3.8, we draw conclusions regarding the feasibility of CSEM monitoring the TU Delft campus low-enthalpy reservoir.

3.2 TU Delft campus geothermal project

The low-enthalpy reservoir of the TU Delft campus geothermal project lies in the West Netherlands Basin, an inverted rift basin. The stratigraphical setting of the West Netherlands Basin down to 3000 m depth and the resistivity of the layers (obtained from logs) are shown in Figure 3.1 (DeVault and Jeremiah, 2002). The target low-enthalpy reservoir is the Delft Sandstone Member, located at a depth of 2300 m. The porosity and permeability of the Delft Sandstone member reach 30 % and 1130 mD, respectively (Donselaar et al., 2015). Temperature logs from exploration wells in the region indicate a gradient of 30 °C/km. Therefore, the water temperature of the Delft Sandstone Member is expected

to be around 75 °C. Overall, the Delft Sandstone Member has aquifer qualities suitable for geothermal energy production.

Layer	[Ω.m]
Upper North Sea	3
Rupel	1.8
Landen	3
Ommelanden	2
Texel	1.5
Holland	2
Vlieland Sandstone	6
Rodenrijs	4
Delft Sandstone	7
Alblasserdam	3

Figure 3.1: Sub-surface layers under the TU Delft campus and their average depth and resistivity.

A geothermal doublet is planned to be installed on the campus of TU Delft, in order to supply heating to the campus buildings. The doublet design, as shown in Figure 3.2, involves a production well and an injection well that will be drilled vertically next to each other in the first 800 m. Then, the boreholes deviate from vertical with different dips and azimuths, until they reach the reservoir with 1500 m separation. After heating the campus buildings, the discharge water will be injected into the reservoir at a temperature between 30–50 °C, depending on the heat demand (Vardon et al., 2020).

The change in electrical resistivity of a pore-filling fluid with temperature can be determined from the following equation (Keller and Frischknecht, 1966):

$$R_{(T_2)} = R_{(T_1)} \left[1 + a \left(T_2 - T_1 \right) \right], \tag{3.1}$$

where $R_{(T_1)}$ and $R_{(T_2)}$ are the electrical resistivities at a base temperature, T_1, and a monitoring temperature, T_2, respectively; and a refers to the temperature coefficient of resistivity, which has a value of $0.025 \,^\circ\mathrm{C}^{-1}$ for most brines (Keller and Frischknecht, 1966). According to Equation (3.1), the electrical resistivity of the TU Delft campus reservoir will change from 7 Ω·m to 11 Ω·m with a temperature drop from 75 $^\circ$C to 50 $^\circ$C.
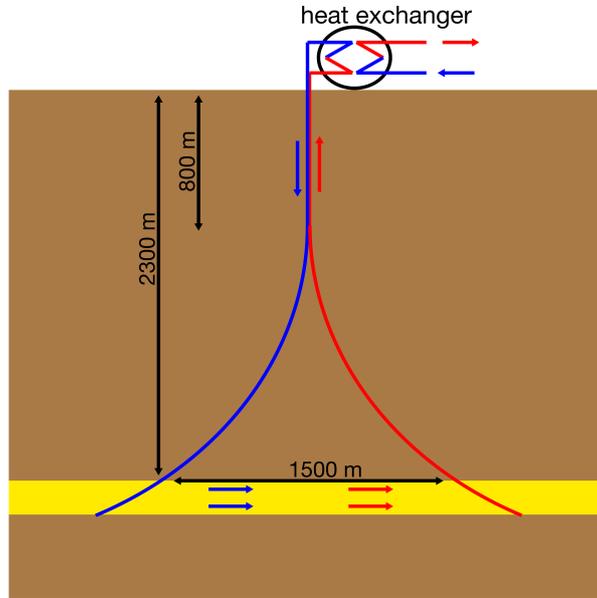
Figure 3.2: Doublet well design for TU Delft campus geothermal project. The well separation at the surface is 10 m. The red and blue arrows refer to the direction of hot and cold water, respectively.

3.3 Methods

We use two frequency-domain EM (FDEM) forward-modelling approaches to study the feasibility of CSEM monitoring the TU Delft campus reservoir: (1) A one-dimensional (1D) reflectivity formulation for a layered model (Hunziker et al., 2015), in order to find a preferential survey configuration and source frequency at a low computational cost. This approach is implemented by Werthmüller (2017); (2) a finite-integration technique to determine the electric field response in a three-dimensional (3D) medium, as coded by Heagy et al. (2017). We use the latter approach to investigate the source–receiver offsets, the sensitivity of CSEM data to volumetric and incremental changes, and the impacts of undesired effects.

To assess the CSEM detectability of the resistivity changes, we define confidence intervals for the difference between time-lapse electric fields. We treat differences below 1 % as undetectable, while differences between 1 % and 10 % offer low confidence, those between 10 % and 30 % moderate confidence, and differences greater than 30 % high confidence. We define these intervals based on the influence of the undesired effects in Section 3.6.

The difference $\triangle E$ between the electric field of the base state E_1 and the monitoring state E_2 is given by

$$\triangle E = \frac{\|E_2 - E_1\|}{\|E_1\|}, \tag{3.2}$$

where $\|\ldots\|$ refers to the absolute value. We mask the time-lapse electric fields and difference when the amplitude of E_1 or E_2 is below the noise floor. The noise floor of electric field data is frequency-dependent (Mittet and Morten, 2012). In Havsgård et al. (2011), it was shown that the noise floor decreases with increasing frequency until it reaches about 4×10^{-12} V/m for frequencies equal to or greater than 1 Hz. For simplicity, we set a noise floor of 10^{-12} V/m for all frequencies.

3.4 Source–injection–borehole offset

We consider the CSEM monitoring of the TU Delft campus reservoir with source offsets 1000, 2000, and 3000 m from the injection well, which has zero offset. The source is an x-directed electric dipole. We carried out 1D numerical experiments to evaluate the source frequency and sensitivity of the EM components to the resistivity change. The results indicate that the vertical electric field is the most sensitive to the changes, and that a source frequency around 1 Hz offers an adequate depth of propagation and resolving power. The resistivity change has a disk shape with 300 m radius, centred at the injection well. The radius of the change is one-fifth the distance between the injector and the producer. The survey domain was discretized with a uniform grid spacing of 50 m along the polar and longitudinal axes, while the azimuthal direction was divided into 40 segments of 9 °.

Figure 3.3 shows the z-component of the electric field for different source offsets. Changing the source offset from 1000 to 3000 m did not change the magnitude of the difference; however, it affected the amplitude of the electric fields reaching the resistivity change and, subsequently, the ability to monitor the 300 m resistivity change. At an offset of 1000 or 2000 m, the monitoring electric fields can cover the resistivity change and the area around it. A difference of moderate confidence was observed within and around the location of the resistivity change. As the time-lapse fields were scattered around the resistivity change, a difference of low confidence could be determined some distance away. A source offset of 3000 m led to a difference of the back-scattered field in a relatively small area. This limits the freedom of measurement for the difference of the forward-scattered field, especially in the case of cold fronts with larger radii. Consequently, we set a source offset in the range of 1000–2000 m with 1 Hz frequency to acquire vertical electric fields for the monitoring of resistivity changes in the TU Delft campus reservoir model.
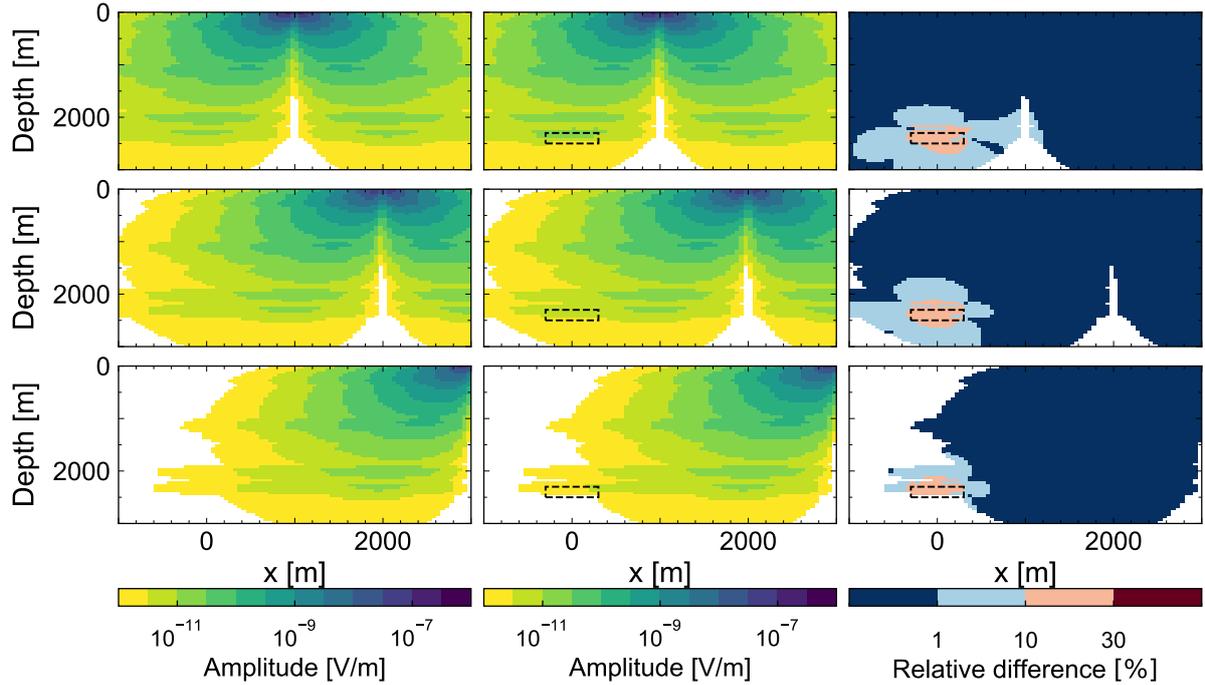
Figure 3.3: Time-lapse electric field response and difference at different source offsets (1000, 2000, or 3000 m from (top) to (bottom)). The (left column) shows the electric field response of the base model, the (middle column) shows that of the monitoring model, and the (right column) provides their relative difference. The dashed rectangle indicates the area of resistivity change in the monitor and the difference data. The time lapse data have been calculated by the 3D finite integration modelling.

3.5   Temperature effects

The CSEM method was able to detect the subtle resistivity changes in the TU Delft campus reservoir with the preferential acquisition setup, as shown in Figure 3.3. Thus, the CSEM monitoring of the TU Delft campus reservoir allows for tracking the growth of the resistivity change over decades. Hence, we checked whether the time−lapse electric field responses acquired with the surface-to-borehole setup were sensitive to an increased resistivity change radius. With an expected fluctuation in temperature of the injected water depending on heat demand, the quantity of the resistivity change will fluctuate as well; see Equation (3.1). Thus, we considered the monitoring of temperature effects under different volumes.

Figure 3.4 shows the difference in monitoring fields determined at a zero offset for different disk radii and magnitudes of the resistivity change. The source had a frequency of 1 Hz and was located with a 1000 m offset. At a certain return temperature, the difference in time−lapse fields increases when increasing the radius of the resistivity change; meanwhile, for a certain radius, the difference increases with temperature. Figure 3.4 indicates that the time-lapse electric fields acquired with the surface-to-borehole configuration are

sensitive to the growth and magnitude of the resistivity change. Considering these results, we next tested the robustness of CSEM monitoring in the presence of undesired effects.
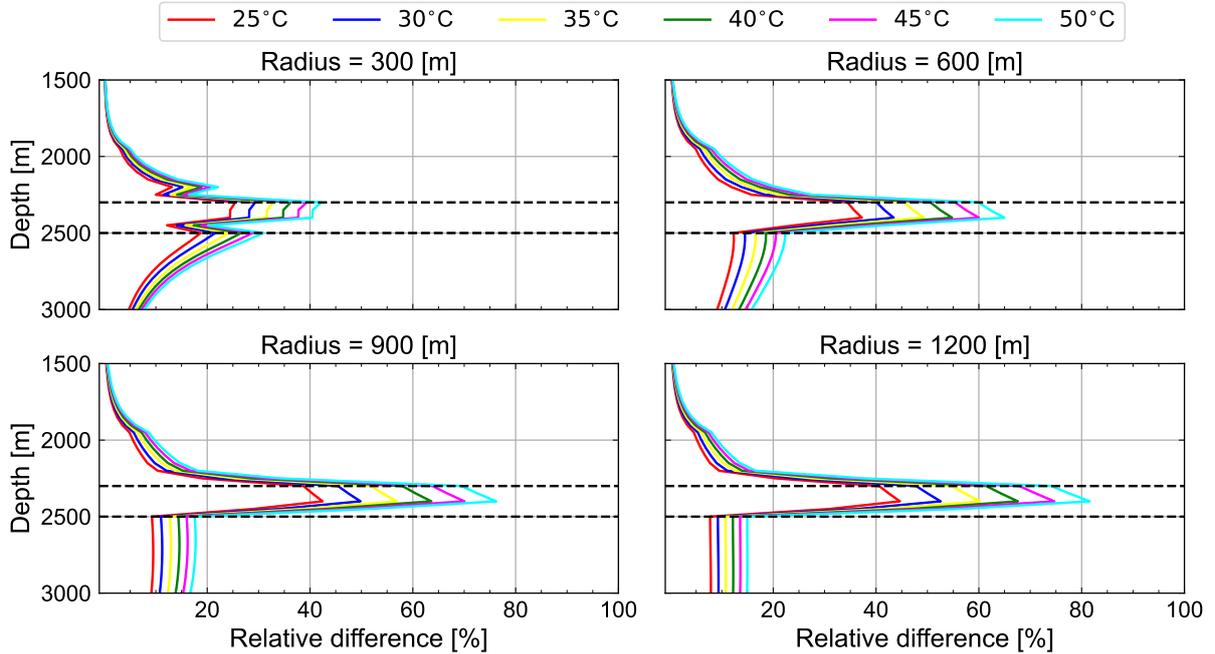

Figure 3.4: Sensitivity of time-lapse electric fields to volumetric and resistivity changes due to various temperature contrasts. The black dashed lines show the boundaries of the low-enthalpy reservoir at 2300 and 2500 m.

3.6 Undesired effects

Beside the change in resistivity, there are various effects that also create a difference in the time-lapse fields. As such, these effects may hinder the CSEM monitoring of the resistivity change inside the low-enthalpy reservoir. In this section, we study the impact of undesired effects on the CSEM monitoring of the 300 m radius resistivity change at a 25 °C temperature contrast, which gives the lowest difference. If a time-lapse CSEM can monitor this change in the presence of signal contamination, it will be able to monitor other scenarios of resistivity change, as detailed in Section 3.5. We consider the following commonly occurring undesired effects.

3.6.1 Recording noise

Recording noise involves receiver self-noise, natural, and anthropogenic noise. Receiver self-noise is random noise caused by the sensor thermal noise and the amplifier voltage noise. Receiver self-noise increases with decreasing source frequency, until it steadies at frequencies above 10^{-1} Hz (Mittet and Morten, 2012). Anthropogenic noise is periodic and/or random (Strack, 1992). Periodic noise is generated by power lines, buried metallic

cables, grounded electric devices, and so on. Most periodic noise can be heavily attenuated by applying digital filters to data. Random anthropogenic noise, on the other hand, can be caused by sources such as the motion of trains or trams on the rail tracks. Random noise can be diminished by stacking repeated measurements to increase the SNR. Increasing the source dipole moment also helps to increase the SNR.

To account for the recording noise that may not be removed via processing, we changed the amplitude of the electric field randomly in the range of ± 1 %, as follows:

$$\eta = 0.01 \left[n_1 \Re(E) + \mathrm{i} n_2 \Im(E) \right], \tag{3.3}$$

where n_1 and n_2 are random values between $-\sqrt{0.5}$ and $\sqrt{0.5}$; the two symbols $\Re(E)$ and $\Im(E)$ refer to the real and the imaginary parts of the calculated electric field response, respectively; and i refers to the imaginary unit. Different random multiplicative noise was added to the base and monitoring electric fields. The electric fields were determined using the setup detailed in Section 3.4.

As shown in Figure 3.5, the resistivity change presented a time-lapse difference that was generally stronger than that of the synthesized recording noise. Random noise in the base and monitoring electric fields can either add or subtract, leading to the amplification or cancellation of the noise in the difference. It is better to reduce the random noise in the data, in order to avoid any possible amplification when calculating the time-lapse difference. After describing the irregular errors arising from random noise, we analyse the errors arising from unrepeatable survey factors.
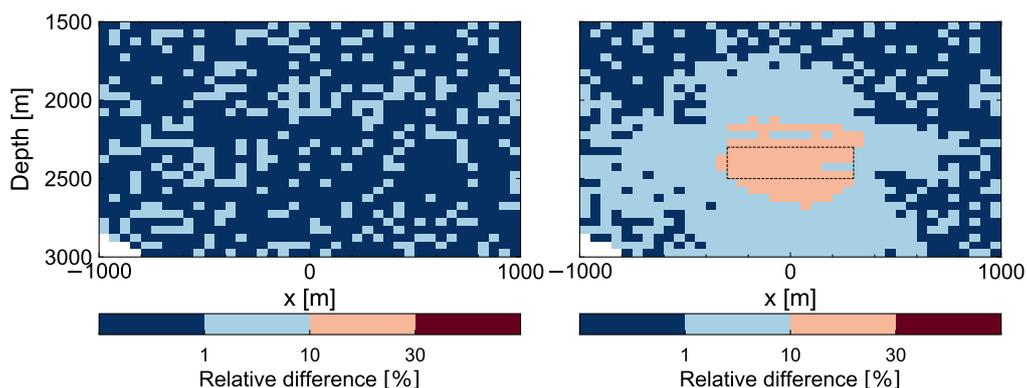
Figure 3.5: The influence of 1 % recording noise when monitoring the 300 m radius change. The (left plot) shows the relative difference due to the random noise, while the (right plot) shows the relative difference between the base and monitoring fields in the presence of the recording noise. The black dashed rectangle indicates the boundaries of the resistivity change.

3.6.2 Survey repeatability errors

Repeatability errors are generated by inexact positioning and/or orientation of the receivers and the source in time-lapse surveys. In a surface-to-borehole survey, wireline receivers are installed in a vertical monitoring well. Replacing aged borehole receivers may change the location of the receivers while their orientation remains fixed. Regarding the surface source, the location, azimuth, and frequency may change. The authors of Wirianto et al. (2010) added 1 % error relative to the signal amplitude to mimic repeatability errors in surface-to-surface surveys. Here, we adopt a different approach to study the impact of 1 % repeatability errors on a surface-to-borehole CSEM. We changed the source location, azimuth, and frequency by 10 m, 1 °, and 0.01 Hz, respectively, and arbitrarily changed the position of the receivers by 5 m.

Figure 3.6 shows that the difference resulting from the survey errors was typically in the range of 1–10 %, and even exceeded 10 % in the 200 m around the zero-crossing. This high error near the zero-crossing was caused by the source repeatability error, as the error decreased when moving away from the source. As the source was 700 m from the edge of the resistivity change, it would still be possible to detect a difference with moderate confidence due to the resistivity change. This implies that the impact of the source repeatability error is reduced when the source is at an adequate distance from the borehole receivers. Next, we examined data errors caused by seasonal near-surface changes.
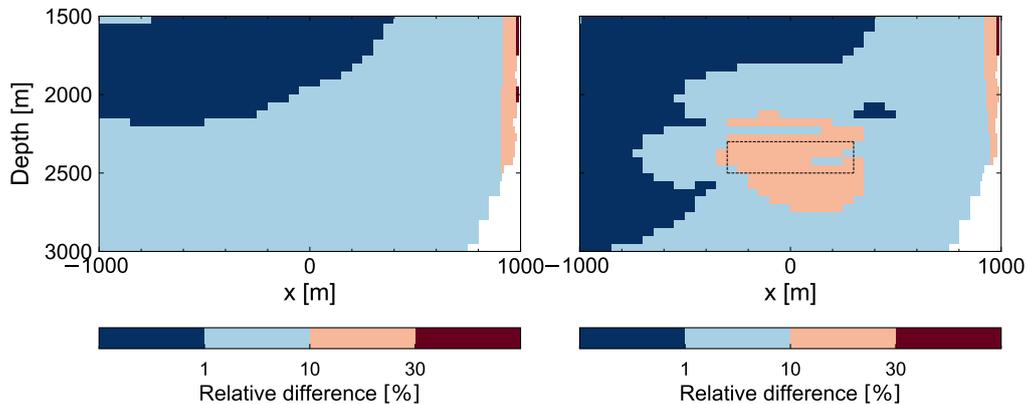
Figure 3.6: Time-lapse monitoring of the TU Delft campus reservoir with errors in the source and receiver parameters. The (left plot) shows the relative difference due to the repeatability error, while the (right plot) shows the difference due to the repeatability error and resistivity change.

3.6.3 Near-surface temperature change

Near-surface changes are commonly caused by seasonal variations in the temperature of the soil, which is in contact with the atmosphere. In particular, seasonal variation in the near-surface temperature alters the time-lapse electric field. In the Netherlands, the average minimum and maximum temperatures at 1 m depth are 8 °C and 17 °C, respectively, while the temperature gradient in the soil is about 4.2 °C/m (Jacobs et al., 2011). The temperature gradient takes a negative value in the summer and a positive value in the winter. At a depth of 2 m, the soil temperature remains almost the same through all seasons. To include the effect of seasonal near-surface variation, we increased the electrical resistivity in the first two meters of the upper layer by 112.5 % (see Equation (3.1)).

The effect of the near-surface resistivity change, as shown in Figure 3.7, did not reach the reservoir. The CSEM fields are sensitive to the conductivity–thickness product of the layers, and the near-surface change occurs over only a slight thickness. Therefore, it did not produce a large difference in time-lapse fields. More importantly, the near-surface change has a limited area of influence in the shallow sub-surface and, so, does not interfere with the monitoring of the low-enthalpy reservoir at depth. After examining the errors from near-surface changes, we investigated the impact of a steel casing on the electric field.
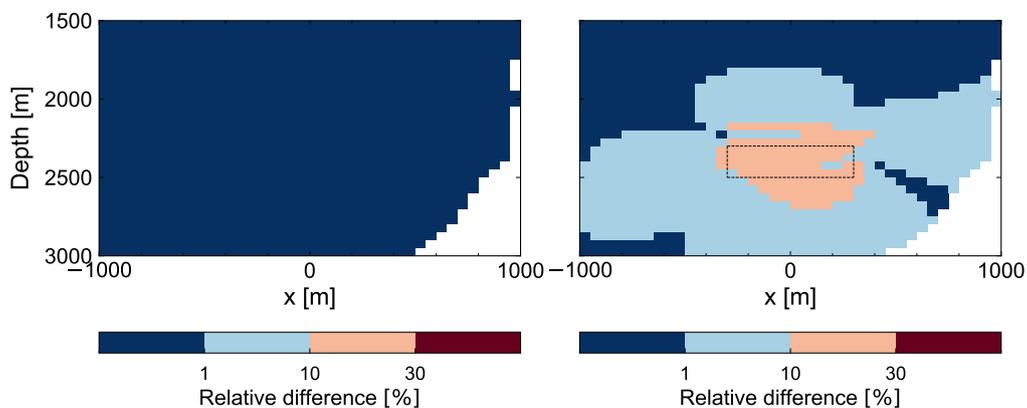
Figure 3.7: Time-lapse monitoring of the TU Delft campus reservoir in the presence of sub-surface changes. The (left plot) shows the relative difference due to the 9 °C seasonal variation in soil temperature, while the (right plot) shows the difference due to the seasonal variation and resistivity changes.

3.6.4 Casing effect

As mentioned in Section 3.2, the design of the TU Delft geothermal doublet includes two deviated steel-cased wells. The impact of the very low electrical resistivity of the steel casing on the EM field response is significant (Kaufman, 1990; Wu and Habashy, 1994;

Swidinsky et al., 2013; Orujov et al., 2022). In Heagy and Oldenburg (2019), it was shown that it is also important to take into account the high magnetic permeability of the steel casing when conducting CSEM forward modelling.

Thus, we incorporated the physical properties of a steel-cased vertical well into the TU Delft campus sub-surface model. The thickness of the casing wall is 2.5 cm and its diameter is 15 cm. The considered steel has an electrical resistivity and a relative magnetic permeability equal to 10^{-6} Ω·m and 100, respectively. The hollow of the casing was assumed to be filled with a brine of resistivity equal to 5.68×10^{-2} Ω·m. The physical properties of the casing do not change over time, corresponding to a non-corroded casing. The model was discretized on a cylindrical mesh. Thus, only the impact of one vertical-cased well could be modelled.

As shown in Figure 3.8, the modelled steel-cased well severely disturbed the electric field. The steel casing changed the field response by 30 % or more within 10 m of its vicinity. The footprint of the steel casing reduced with distance, ranging between 10 and 30 % within 100 m and less than 10 % further away. Close to the source location, the footprint of the casing was less than 1 %, except around the zero-crossing. This significant distortion in the electric field was caused by electric fields induced in the modelled steel medium. These fields propagate into the surrounding environment to distort the electric fields from the source. Figure 3.8 also shows that the detectability of the resistivity change decreased within 10 m around the steel casing, as well as some other areas within 100 m around the casing. Away from the casing, the resistivity change still created a sufficient difference.
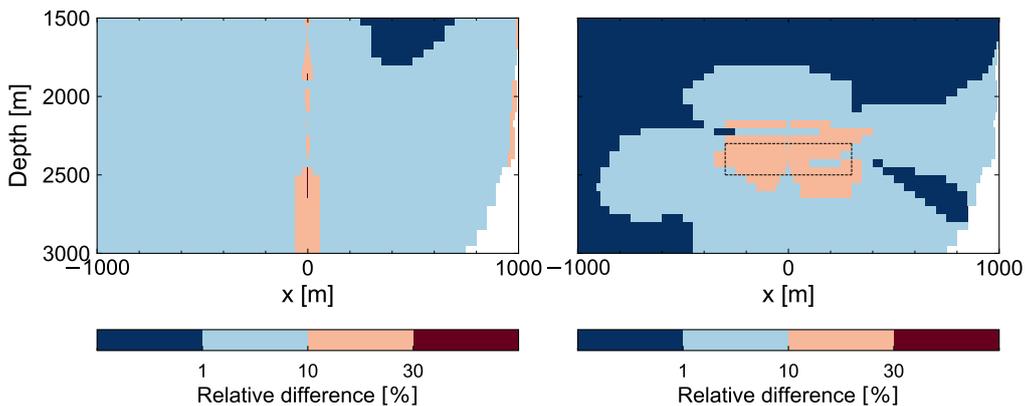

Figure 3.8: Time-lapse CSEM monitoring of the TU Delft campus reservoir in the presence of a steel casing. The (left plot) shows the effect of the steel casing on the electric field response, while the (right plot) shows the effect of the steel casing on the difference between time-lapse electric fields.

We changed the properties of the casing from steel to fibreglass-reinforced epoxy, which has resistivity of around 10^{16} Ω·m and unit magnetic permeability. The effect of the composite casing on the electric field was limited to the borehole, and is not observable

in Figure 3.9. Based on the right-hand plots in Figures 3.8 and 3.9, it seems that the composite casing had no influence on the electric field outside the casing, allowing for the CSEM monitoring of the geothermal reservoir close to the borehole. The negligible impact of the composite medium can be attributed to its very high electrical resistivity and no magnetization, therefore not producing induction fields.
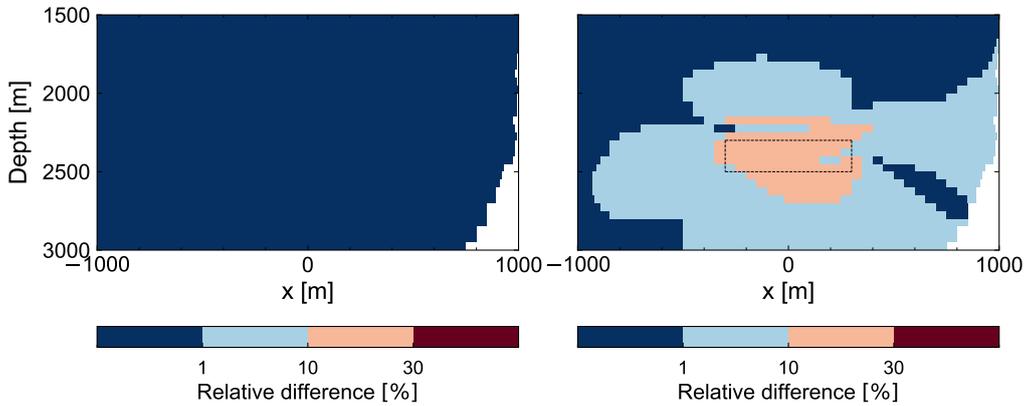

Figure 3.9: Time-lapse CSEM monitoring of the TU Delft campus reservoir in the presence of a composite casing. The (left plot) shows the effect of the composite casing on the electric field response, while the (right plot) shows the effect of the composite casing on the difference between time-lapse electric fields.

3.7 Discussion

We studied the feasibility of CSEM monitoring of resistivity changes in the TU Delft campus reservoir, which involves a custom surface-to-borehole setup. This setup requires the drilling of a monitoring well for the installation of borehole receivers. The forward modelling results did not identify an optimal location for such a monitoring well. An optimized experimental design may help to find such a location. When assessing the location of a monitoring well, the relatively high fluid flow between wells resulting from energy production should be considered. This high fluid flow would cause a sharp edge in the changes toward the production well, which should ideally be monitored.

The results of our study show—as can be observed in Figure 3.4—that the CSEM method is sensitive to resistivity changes inside the TU Delft geothermal reservoir model, regardless of their radius or magnitude. However, we found that changes of large radius and small magnitude provide the same difference as changes of a small radius and large magnitude, which introduces uncertainty into the interpretation of time-lapse CSEM data. As such, it may be necessary to combine CSEM data with other geophysical data; in particular, coupling it with sub-surface fluid flow models and local temperature and pressure measurements in the injection and monitoring wells is necessary to obtain better insights regarding the changes.

Undesired effects pose significant challenges for CSEM monitoring. These effects distort the field response and can make it difficult to detect resistivity changes. While random recording noise and near-surface changes have a minor impact, survey repeatability errors lead to more severe effects. Close to the source, repeatability errors may generate a difference greater than the difference due to the resistivity change. The steel casing also has a severe impact, heavily damping the vertical electric field in its vicinity. To reduce the sensitivity of CSEM data to severe undesired effects, the data should be collected at least 200 m away from the source and 100 m from steel-cased boreholes. Our results suggest that the CSEM method can provide valuable information about the resistivity changes inside the TU Delft campus reservoir, despite the presence of undesired effects.

3.8   Conclusions

We demonstrated the feasibility of using the CSEM method to monitor the subtle resistivity changes inside the TU Delft campus low-enthalpy reservoir model. In this feasibility study, we determined a survey design—including the survey configuration, source frequency, and source offset—that allows for the CSEM monitoring of the resistivity changes in the TU Delft campus reservoir with sufficient confidence. The results of the study indicated that the z-component determined with a surface-to-borehole CSEM is sensitive to resistivity changes of different volumes and contrasts, suggesting its suitability for monitoring changes in the reservoir due to heat production over decades.

Through this study, we showed that the CSEM monitoring of the TU Delft campus geothermal reservoir seems possible, even in the presence of undesired effects. Among these effects, survey repeatability errors had the largest impact on CSEM monitoring. The effect of the steel casing was negligible 100 m away from it. When we changed the properties of the casing from steel to composite, we found that the electric field response was only affected within the casing. Generally speaking, the CSEM method with a customized acquisition setup can be used to detect small resistivity changes in the TU Delft campus low-enthalpy reservoir with high confidence, which will not be obscured by undesired effects.

Overall, the results of this feasibility study demonstrate that the CSEM has high potential as a viable technology for monitoring and managing low-enthalpy geothermal reservoirs, such as the TU Delft campus reservoir. The results of our study indicate that time-lapse CSEM surveys can provide information to make well-informed management decisions, possibly extending the production lifetime of low-enthalpy reservoirs. The approach followed in this study can serve as a framework for future CSEM field tests and, when successful, eventually for monitoring campaigns. This also includes monitoring high-enthalpy geothermal reservoirs.

References

Abdelfettah, Y., Sailhac, P., Larnier, H., Matthey, P., and Schill, E. (2018). Continuous and time-lapse magnetotelluric monitoring of low volume injection at Rittershoffen geothermal project, northern Alsace–France. Geothermics, 71:1–11.

Axelsson, G., Stefánsson, V., Björnsson, G., and Liu, J. (2005). Sustainable management of geothermal resources and utilization for 100–300 years. In Proceedings World Geothermal Congress, volume 8.

Axelsson, G., Stefánsson, V., and Xu, Y. (2003). Sustainable management of geothermal resources. In Proceedings of the International Geothermal Conference, pages 40–48.

Balasco, M., Lapenna, V., Rizzo, E., and Telesca, L. (2022). Deep electrical resistivity tomography for geophysical investigations: the state of the art and future directions. Geosciences, 12(12):438.

Barbier, E. (2002). Geothermal energy technology and current status: an overview. Renewable and sustainable energy reviews, 6(1-2):3–65.

Bödvarsson, G. S. and Tsang, C. F. (1982). Injection and thermal breakthrough in fractured geothermal reservoirs. Journal of Geophysical Research: Solid Earth, 87(B2):1031–1048.

Bruhn, D. F., Wolf, K., Woning, M., Nick, H. M., Willems, C., et al. (2015). The Delft Aardwarmte Project (DAP): providing renewable heat for the university campus and a research base for the geothermal community.

Chandrasekharam, D. and Bundschuh, J. (2008). Low-enthalpy geothermal resources for power generation. CRC press.

Chave, A. D. and Jones, A. G. (2012). The magnetotelluric method: Theory and practice. Cambridge University Press.

Colombo, D. and McNeice, G. W. (2013). Quantifying surface-to-reservoir electromagnetics for waterflood monitoring in a Saudi Arabian carbonate reservoir. Geophysics, 78(6):E281–E297.

Colombo, D. and McNeice, G. W. (2018). Surface to borehole CSEM| for waterflood monitoring in Saudi Arabia: Data analysis. In SEG Technical Program Expanded Abstracts 2018, pages 868–872. Society of Exploration Geophysicists.

Constable, S. and Srnka, L. J. (2007). An introduction to marine controlled-source electromagnetic methods for hydrocarbon exploration. Geophysics, 72(2):WA3–WA12.

DeVault, B. and Jeremiah, J. (2002). Tectonostratigraphy of the nieuwerkerk formation (delfland subgroup), west Netherlands basin. AAPG bulletin, 86(10):1679–1707.

Donselaar, M. E., Groenenberg, R. M., and Gilding, D. T. (2015). Reservoir geology and geothermal potential of the Delft Sandstone Member in the West Netherlands Basin. In Proceedings world geothermal congress, page 9.

Egbert, G. D. (1997). Robust multiple-station magnetotelluric data processing. Geophysical Journal International, 130(2):475–496.

Eltayieb, M., Werthmüller, D., Drijkoningen, G., and Slob, E. (2023). Feasibility study of controlled-source electromagnetic method for monitoring low-enthalpy geothermal reservoirs. Applied Sciences, 13(16):9399.

European Commission (2011). Communication from the Commission to the European Parliament, the Council, the European Economic and Social Committee and the Committee of the Regions Youth Opportunities Initiative.

Fraser Smith, A. and Coates, D. (1978). Large-amplitude ULF electromagnetic fields from BART. Radio Science, 13(4):661–668.

Havsgård, G. B., Jensen, H. R., Kurrasch, A., Jones, H., Austin, P., and Thompson, A. (2011). Low noise Ag/AgCl electric field sensor system for marine CSEM and MT applications. Geoservices ASA.

Heagy, L. J., Cockett, R., Kang, S., Rosenkjaer, G. K., and Oldenburg, D. W. (2017). A framework for simulation and inversion in electromagnetics. Computers & Geosciences, 107:1–19.

Heagy, L. J. and Oldenburg, D. W. (2019). Modeling electromagnetics on cylindrical meshes with applications to steel-cased wells. Computers & Geosciences, 125:115–130.

Hunziker, J., Thorbecke, J., and Slob, E. (2015). The electromagnetic response in a layered vertical transverse isotropic medium: A new look at an old problem. Geophysics, 80(1):F1–F18.

Jacobs, A. F., Heusinkveld, B. G., and Holtslag, A. A. (2011). Long-term record and analysis of soil temperatures and soil heat fluxes in a grassland area, The Netherlands. Agricultural and Forest Meteorology, 151(7):774–780.

Kaufman, A. A. (1990). The electrical field in a borehole with a casing. Geophysics, 55(1):29–38.

References

Kaya, E., Zarrouk, S. J., and O'Sullivan, M. J. (2011). Reinjection in geothermal fields: A review of worldwide experience. Renewable and sustainable energy reviews, 15(1):47–68.

Keller, G. V. and Frischknecht, F. C. (1966). Electrical methods in geophysical prospecting.

Lake, A., Rezaie, B., and Beyerlein, S. (2017). Review of district heating and cooling systems for a sustainable future. Renewable and Sustainable Energy Reviews, 67:417–425.

Martín-Gamboa, M., Iribarren, D., and Dufour, J. (2015). On the environmental suitability of high-and low-enthalpy geothermal systems. Geothermics, 53:27–37.

Mazhar, A. R., Liu, S., and Shukla, A. (2018). A state of art review on the district heating systems. Renewable and Sustainable Energy Reviews, 96:420–439.

Mittet, R. and Morten, J. P. (2012). Detection and imaging sensitivity of the marine CSEM method. Geophysics, 77(6):E411–E425.

Muffler, P. and Cataldi, R. (1978). Methods for regional assessment of geothermal resources. Geothermics, 7(2-4):53–89.

Munoz, G. (2014). Exploring for geothermal resources with electromagnetic methods. Surveys in geophysics, 35(1):101–122.

Myer, D., Constable, S., and Key, K. (2011). Broad-band waveforms and robust processing for marine CSEM surveys. Geophysical Journal International, 184(2):689–698.

Nabighian, M. N. (1988). Electromagnetic Methods in Applied Geophysics: Voume 1, Theory. Society of Exploration Geophysicists.

Nabighian, M. N. (1991). Electromagnetic methods in applied geophysics: Volume 2, Application, Parts A and B.

Olasolo, P., Juárez, M., Morales, M., Liarte, I., et al. (2016). Enhanced geothermal systems (EGS): A review. Renewable and Sustainable Energy Reviews, 56:133–144.

Olufemi, O., Bello, O., Olaywiola, O., Teodoriu, C., Salehi, S., and Osundare, O. (2020). Geothermal heat recovery from matured oil and gas fields in nigeria–well integrity considerations and profitable outlook. In Proceedings of the 45th Workshop on Geothermal Reservoir Engineering, Stanford, CA, USA, pages 10–12.

Orujov, G., Streich, R., and Swidinsky, A. (2022). Modeling and inversion of electromagnetic data collected over steel casings: An analysis of two controlled field experiments in colorado. The Leading Edge, 41(2):114–121.

O'Sullivan, M. J., Pruess, K., and Lippmann, M. J. (2001). State of the art of geothermal reservoir simulation. Geothermics, 30(4):395–429.

Pirouti, M., Bagdanavicius, A., Ekanayake, J., Wu, J., and Jenkins, N. (2013). Energy consumption and economic analyses of a district heating network. Energy, 57:149–159.

Poulsen, S., Balling, N., and Nielsen, S. (2015). A parametric study of the thermal recharge of low enthalpy geothermal reservoirs. Geothermics, 53:464–478.

Schön, J. H. (2015). Physical properties of rocks: Fundamentals and principles of petrophysics. Elsevier.

Stefansson, V.-đ. (1997). Geothermal reinjection experience. Geothermics, 26(1):99–139.

Strack, K.-M. (1992). Exploration with deep transient electromagnetics, volume 373. Elsevier Amsterdam.

Swidinsky, A., Edwards, R. N., and Jegen, M. (2013). The marine controlled source electromagnetic response of a steel borehole casing: Applications for the NEPTUNE Canada gas hydrate observatory. Geophysical Prospecting, 61(4):842–856.

Vardon, P., Bruhn, D., Steiginga, A., Cox, B., Abels, H., Barnhoorn, A., Drijkoningen, G., Slob, E., and Wapenaar, K. (2020). A Geothermal Well Doublet for Research and Heat Supply of the TU Delft Campus. arXiv preprint arXiv:2003.11826.

Virieux, J. and Operto, S. (2009). An overview of full-waveform inversion in exploration geophysics. Geophysics, 74(6):WCC1–WCC26.

Wang, Y., Voskov, D., Khait, M., Saeid, S., and Bruhn, D. (2021). Influential factors on the development of a low-enthalpy geothermal reservoir: A sensitivity study of a realistic field. Renewable Energy, 179:641–651.

Werthmüller, D. (2017). An open-source full 3D electromagnetic modeler for 1D VTI media in Python: empymod. Geophysics, 82(6):WB9–WB19.

Wirianto, M., Mulder, W., and Slob, E. (2010). A feasibility study of land CSEM reservoir monitoring in a complex 3-D model. Geophysical Journal International, 181(2):741–755.

Wu, X. and Habashy, T. M. (1994). Influence of steel casings on electromagnetic signals. Geophysics, 59(3):378–390.

Ziolkowski, A. and Slob, E. (2019). Introduction to Controlled-source Electromagnetic Methods: Detecting Subsurface Fluids. Cambridge University Press.

Chapter 4

FWI of VSP Data for Munich Geothermal Reservoir Monitoring

Tracking temperature changes caused by heat production in geothermal reservoirs is crucial to establish effective management strategies and prevent early thermal breakthroughs. Utilizing variations in the elastic subsurface properties is a practical choice for such an application. However, the corresponding variations are quite small, and thus require seismic characterization with high resolution. To this end, seismic full waveform inversion (FWI) is a potentially powerful tool. We parameterized the properties of the subsurface for acoustic impedance. The FWI for impedances faces challenges in capturing subtle variations due to crosstalk and trade-offs with other parameters, specifically P-wave velocity (V_P). To address this problem, we have developed a novel acoustic FWI algorithm that is suitable for vertical seismic profiling (VSP) data. We start with a traveltime inversion for obtaining an initial plane layered V_P model, followed by a FWI, in which we refine the velocities. Before we apply a FWI for acoustic impedance, we perform a phase resemblance correction, which mitigates the propagation of errors from a V_P model into an impedance model. Inversion experiments with synthetic data validated our approach by demonstrating its ability to identify impedance variations greater than 1 %, supporting its applicability to detect realistic variations caused by temperature changes in a low-enthalpy reservoir. Building on these promising results, we applied the approach to the baseline VSP data recorded until a depth of 2580 m, lying in a low-enthalpy reservoir in Munich, Germany. The application to the field VSP data confirmed the robustness of our approach and improved the seismic characterization at the geothermal site. The FWI-estimated velocities and impedances reveal a striking contrast at a depth of 2300 m, delineating the boundary between marls and limestone, and the oscillatory nature of these estimated properties suggest the presence of vertical transverse isotropy (VTI). This 1D study establishes a foundation for advanced seismic characterization frameworks,

paving the way for sophisticated FWI of 2D and 3D impedance models, enabling seismic monitoring of low-enthalpy reservoirs.

4.1 Introduction

Low-enthalpy geothermal reservoirs are a crucial source of green energy for district heating. These reservoirs consist of permeable rocks saturated with geothermal fluids at temperatures between 50 and 150 °C (Muffler and Cataldi, 1978; Moeck, 2014). Heat is extracted from these fluids on the surface, after which they are re-injected at lower temperatures (Randolph and Saar, 2011; Martín-Gamboa et al., 2015). Over time, the re-injected fluids cool a growing volume of the reservoir at a rate determined by the production rate (Bödvarsson and Tsang, 1982; Axelsson et al., 2003; Kaya et al., 2011). When this cooled volume reaches production wells, the energy output can decline to uneconomic levels, threatening the sustainability of heat production (Sanyal et al., 1995).

Tracking temperature changes in low-enthalpy reservoirs over time is therefore essential to optimize production and help economic viability, as well as resource sustainability (Poulsen et al., 2015). However, direct temperature measurements within the volume of a geothermal reservoir are generally not feasible (Grant, 2013). Elastic properties are inversely proportional to temperature, and their variations can serve as an indicator of heat production (Cammarano et al., 2003). Zhang et al. (2020) showed a linear decrease in acoustic velocity and density of dry sandstones as a function of temperature. Zou et al. (2022) studied the effect of temperature on the elastic moduli of dry sandstones, where increasing the temperature from 20 to 140 °C decreased the bulk and the shear modulus by 3 % and 16 %, respectively. In addition to the rock matrix, the saturating fluids are also affected by temperature (Batzle and Wang, 1992; Poletto et al., 2018). In water saturated sandstones, Wang and Nur (1988) indicated a reduction in P- and S-wave velocities (V_P and V_S) by 130 and 150 m/s for 100 °C increase from room temperature. Using the ultrasonic wave pulse method, Qi et al. (2021) showed a moderate variation in the P-wave impedance with temperature in water-saturated carbonate rocks, including dolomite. Detecting such variations inside low-enthalpy reservoirs requires seismic data that allow for high resolution over wide inter-well volumes.

Seismic data can be acquired with surface, crosswell, or vertical seismic profiling (VSP) configurations. Surface data can cover large areas, but often suffer from limited resolution and poor signal-to-noise ratio (SNR) at large depths, especially in areas with complex overburden (Krampe et al., 2021). Crosswell data offer high resolution in the plane between wells with limited coverage elsewhere, making them unsuitable for studying interwell volumes (Musil et al., 2003; Ernst et al., 2007). VSP data provide a balance between covering wide regions of the reservoir and maintaining high resolution with high

SNR (Reiser et al., 2017). The proximity of receivers to reservoirs reduces attenuation and scattering effects (Eltayieb et al., 2023), making VSP suitable for characterization and monitoring.

Here, we focus on the VSP data collected at an urban geothermal site in the city of Munich. At this site, the low-enthalpy reservoir is composed of carbonate rocks, predominantly calcite dolomite (Krumbholz et al., 2024). According to Qi et al. (2021), the P-wave impedance is expected to vary in a measurable way compared to velocity as a result of heat production. There are mainly three strategies for detecting variations with the VSP data (Raknes et al., 2013): (1) Inversion of baseline and monitor datasets separately and subtract the estimated models (Hicks et al., 2016), (2) using the estimated model from the baseline data as an initial model in the inversion of the monitor data, which should capture the difference (Routh et al., 2012; Maharramov and Biondi, 2015; Oghenekohwo et al., 2015; Raknes and Arntsen, 2015), and (3) the double difference strategy that depends on using the estimated model from the baseline data to invert the difference between the data from two repeated surveys (Denli and Huang, 2009; Yang et al., 2015). Generally speaking, all mentioned strategies necessitate estimating a base model (characterization) of acoustic impedance with high resolution (Asnaashari et al., 2012; Eikrem et al., 2019), which can be achieved through reconstruction methods.

Traditional reconstruction methods, such as traveltime tomography and reflection imaging, face significant drawbacks in this geothermal application. Traveltime tomography provides effective velocities over depth intervals based on the arrival time of direct waves (Schmelzbach et al., 2008), but it neglects information on impedances. Reflection seismic imaging effectively gives subsurface structures based on acoustic impedances (Brodic et al., 2021). Proper migration is necessary for imaging, which requires data from many source positions (Verschuur and Berkhout, 2011). In addition to the expensive cost associated with data acquisition and processing, it has limited resolution at large depths and inherent ambiguities in interpretation (Zhang et al., 2001). By utilizing all the information in recorded seismic data, that is, phases and amplitudes, full waveform inversion (FWI) can estimate models independently of the acquisition geometry in contrary to the former approach (Zhou et al., 2015). Therefore, FWI has the potential to invert the VSP data for high-resolution characterization of the acoustic impedance in the subsurface of the Munich geothermal site, including the low-enthalpy reservoir.

P-wave impedance is the product of V_P and density, ρ, of a medium, describing its resistance to propagation of compressional waves (Kinsler et al., 2000). Hence, the FWI of the P-wave impedance is associated with that of the V_P and the ρ. Simultaneous FWI of these two acoustic properties causes crosstalk and trade-offs between them (Egorov et al., 2017). The cross-talk effect occurs when different properties exert a similar influ-

ence on seismic data, leading to inaccurate model updates (Virieux and Operto, 2009). In addition, seismic waveforms are inherently more sensitive to velocity contrasts than to impedance contrasts, which tends to prioritize recovery of V_P at the expense of density (Pan et al., 2018, 2019). Sequential FWI can be a solution to mitigate these issues by decoupling the inversion processes (Sirgue and Pratt, 2004). However, propagation of phase errors from estimated acoustic velocity to impedance parameters is still a critical issue (Kamei and Lumley, 2017).

This study introduces a novel acoustic FWI approach designed for inverting VSP data. The proposed approach addresses key challenges in estimating a layered P-wave impedance structure, allowing the detection of subtle variations related to temperature changes in the low-enthalpy reservoir. This is achieved through an advanced inversion approach based on Gauss-Newton optimization. The inversion process is sequential, recovering V_P prior to recovering the P-wave impedance. Large velocity contrasts were difficult to recover and caused errors that propagated to the subsequent inversion. To solve this problem, we introduce an intermediate step called temporal phase resemblance.

The remainder of this chapter is organized as follows; Section 4.2 describes the Munich geothermal site, the VSP data acquisition setup, and the key challenges. Section 4.3 details the 1D FWI methodology, including forward modeling and inversion techniques. Section 4.4 outlines the data preprocessing workflow. Sections 4.5.1 and 4.5.2 validate the proposed approach with synthetic data and demonstrate its successful application to field data. Finally, Section 4.6 discusses the merits and limitations of the proposed FWI approach, and Section 4.7 represents the conclusions on the recovery of the P-wave impedance for more robust seismic characterization that can be useful for future monitoring of the Munich geothermal reservoir and low-enthalpy reservoirs in general.

4.2 Munich VSP data

4.2.1 Munich geothermal site

The study area is the Schäftlarnstraße geothermal site in the city of Munich (Pfrang et al., 2022; Jeßberger et al., 2025), the largest of its kind in Europe (Flechtner et al., 2020). It produces approximately 50 MW_{th} environmentally friendly district heating for 80,000 households, reducing CO_2 emissions by approximately 350,500 metric tons per year. The low-enthalpy reservoir is the Malm Formation in the Molasse foreland basin (Bachmann et al., 1987). The Malm Formation is composed of carbonate rocks, i.e. limestones and dolomites (Meyer and Schmidt-Kaler, 1990). These carbonate rocks are highly permeable (Hörbrand et al., 2025) although examination of the rock samples in the laboratory show rather low permeabilities (Bohnsack et al., 2020). The high thermal conductivity and

the elevated heat flow in the region contribute to a significant geothermal anomaly in the Malm layer (Agemar et al., 2012; Schölderle et al., 2023). Heat is extracted from geothermal fluids via three producers at around 100 °C. These fluids are then reinjected at 60 °C. Based on the experimental study by Qi et al. (2021) of a similar lithology, a change of 40 °C in the temperature would result in a variation of V_{P}, V_{S} and P-wave impedance of approximately 1 %, 1 %, and 12 %, respectively.

4.2.2 Acquisition setup

In 2020, a VSP survey was conducted in a production well, Th1. The well is drilled deviated in the reservoir interval and crosses a fault plane at 2100 m. A seismic vibrator was deployed at 185.79 m and 24.4 ° northeast of the well head, as shown in Fig. 4.1. The vibrator emitted 12 s sweeps with frequencies in the range of 12-110 Hz. The sweeps were repeated five times to increase the SNR. The signal was recorded by Sercel slimwave geophones lowered in Th1, a production well with a deviated trajectory. For these geophones to record signal, the borehole diameter should be between 0.057 and 0.330 m. For the first 800 m, the diameter of the Th1 well is 0.508 m so the geophones could not couple to the borehole wall and therefore could not record proper signal. Between 811 to 2580 m, the receivers were placed every 15.2 m.
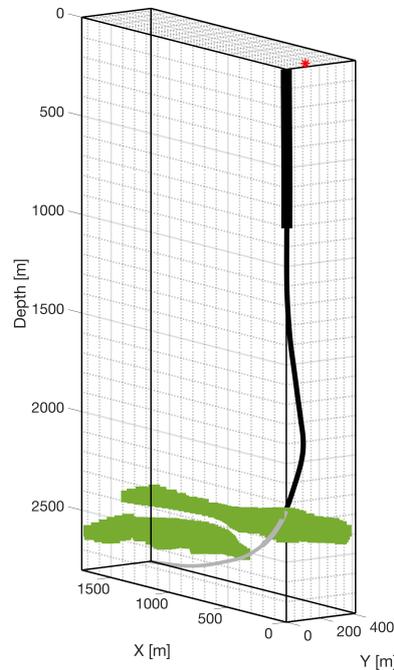
Figure 4.1: Setup of the VSP survey at the Munich geothermal site. The red star indicates the vibrator location. The curved line represents the geometry of the Th1 borehole, with different line widths indicating different borehole diameters while the grey segment indicates production liner. The green planes indicate the upper reservoir boundary. The discontinuity in the boundary indicates a normal fault.

4.3 Acoustic FWI approach

4.3.1 Time domain waveform modeling

Prior to inversion, it is required to calculate seismic waveforms propagating in a representative model of the subsurface, allowing their comparison with observed waveforms. The lack of data from many source locations limits the ability to reconstruct a two-dimensional (2D) or three-dimensional (3D) model in the urban geothermal site of Munich with sufficient resolution. Moreover, the VSP data in Fig. 4.6 do not exhibit waves scattered by geological complexity that demand a 2D or a 3D model. Therefore, we assume that the geological layers can be well approximated by a plane-layered medium. In this case, seismic wave propagation can be modeled efficiently and accurately using algorithms based on propagator matrices (Kennett and Kerry, 1979). The model parameters include V_{P}, ρ, and layer thickness. The solution to these matrices can be analytically obtained in the frequency–horizontal–wavenumber domain. Here, we use the implementation of this method by Herrmann (2013) in Computer Programs in Seismology (CPS).

4.3.2 Time domain waveform inversion

FWI is an ill-posed inverse problem (Tarantola, 2005) to find an acceptable model (m) that minimizes the data residuals contained in the vector δd (Fichtner, 2010),

$$\delta d = d_{obs} - d_{calc}, \tag{4.1}$$

where d_{obs} are the preprocessed observed data and d_{calc} are the calculated data. The residuals and thus the inversion can be evaluated in the time domain or in the frequency domain. We choose the time domain because it allows: (1) a cost-effective inversion by fitting a broad range of frequencies at once, and (2) an improved accuracy by directly linking between different waveform events and the impedance model. The fit between d_{obs} and d_{calc} is quantified by the relative data error (ϵ_d),

$$\epsilon_d = \frac{||\delta d||}{||d_{obs}||}, \tag{4.2}$$

where $||\cdots||$ refers to the Euclidean norm. To solve the FWI inverse problem, we use the Levenberg-Marquardt (LM) algorithm with a smoothing term as follows (Menke, 2018):

$$m^{(i+1)} = m^i + \left[\left(\mathbf{J}^{(i)} \right)^T \mathbf{J} + \left(\alpha \mathbf{S}^{(i)} \right)^2 + \beta^2 \mathbf{L}^T \mathbf{L} \right]^{-1} \mathbf{J}^{(i)} \delta d^{(i)}, \tag{4.3}$$

where i is the iteration number, $\mathbf{J}$ is the Jacobian matrix of dimensions $N \times M$, with N the number of data points in seismic traces and M the number of layers, the superscript

T refers to matrix transpose, $\mathbf{S}$ is a diagonal scaling matrix of the damping parameter α, $\mathbf{L}$ is the Laplacian smoothing operator while β is the smoothing parameter. $\mathbf{S}$ determines weights of α for each parameter of m using sensitivities as (Nuber et al., 2015)

$$\mathbf{S} = diag \left(\frac{max \left(\sum_p J_{pq}^2 \right)}{\sum_p J_{pq}^2 + \delta} \right), \qquad (4.4)$$

with $p = 1, 2, \cdots, N$, $q = 1, 2, \cdots, M$, and δ equals 10^{-6} added to the dominator to ensure numerical stability. To calculate the sensitivities in $\mathbf{J}$, we use the perturbation approach. In this approach, each model parameter m_q is perturbed by a small amount $\Delta m_q^{(i)}$, then data $(d_{\Delta m_q}^{(i)})$ are calculated. The sensitivity is determined by

$$J_q^{(i)} = \frac{d_{calc}^{(i)} - d_{\Delta m_q}^{(i)}}{\Delta m_q^{(i)}}. \qquad (4.5)$$

The LM scheme is a local optimization approach, whose performance depends on the initial model, especially for V_P. An initial model near the global minimum helps to avoid cycle skipping and ensures convergence to an optimal model with quadratic convergence.

This initial model is estimated via traveltime tomography, which relies on fitting calculated arrival times to picked arrival times. We develop a traveltime tomography algorithm to determine an initial layered model from VSP data. We use Eq. 4.3 to find a model that fits the calculated V_P arrivals to the picked arrivals. To calculate the arrival times and the lengths of the ray paths, we use the 3D fast marching method for ray tracing (Sethian, 1996; Rawlinson and Sambridge, 2005) as coded by Chen et al. (2023). In the two inversions—traveltime tomography and FWI—the choice of regularization parameters is crucial. Appropriate regularization, determined with synthetic data by trial and error, reduces the roughness of the model space without flattening and uplifting the global minimum.

4.3.3   Estimation of source time function

An integral part of our FWI approach is the accurate estimation of the source time function (STF). This estimation can be done in the frequency domain by spectral division or in the time domain by deconvolution or inversion. STF inversion in the time domain strictly preserves the phase information, which offers the accuracy needed for high-resolution characterization. We invert the STF in the time domain with the LM algorithm, Eq. 4.3. A reasonable duration of the wavelet should be selected that is not shorter than the duration of the first arrival. The STF is updated iteratively based on sensitivity kernels, which are calculated through perturbations, Eq. 4.5.

4.3.4 Temporal phase resemblance and P-impedance inversion

After FWI of V_{P}, impedance model updates rely on fitting the amplitudes of analogous phases. However, some phases are not fully matched as shown in Fig. 4.2, because the residuals are too small to offer velocity updates, or the updates increase the mismatch and are not accepted. This issue may arise because of excessive regularization, leading to over-smoothed global minimum or deficient regularization leading to an irregular global minimum. In general, the cross correlation R_r defined by the following equation would not have a maximum at zero lag as shown in Fig. 4.3,

$$R_r[k] = \sum_{t=-\infty}^{\infty} d_{\mathrm{obs},r}[t]\, d_{\mathrm{calc},r}[t+k], \qquad (4.6)$$

where r is the receiver index, t is the time index, and k is the lag. To advance FWI of P impedance, we propose phase resemblance of seismic waveforms. By achieving coherence between the observed and modeled waveforms, amplitude fitting will result in accurate updates of impedance. From Eq. 4.6, we determine the amount of lag (g). To let g going to zero, the traces can be shifted forward or backward, and zero padding is applied at the end or the front. Otherwise, a cyclical shift equal to the amount of lag can be used, which is more convenient for implementation. To achieve the highest possible coherence, we cyclically shift all the phases on the calculated traces by the lag amount as follows:

$$d_{\mathrm{calc},r}'[t] = d_{\mathrm{calc},r}[(t-g) \mod t_d], \qquad (4.7)$$

whereby mod ensures circular shifting by constraining values within a fixed range $[1, t_d]$. When a value exceeds the total time of a seismic trace, t_d, it wraps around the beginning, and when it drops 1, it cycles back to the end. Fig. 4.3 shows the cross correlation before and after phase resemblance. The last step is the FWI of the P-wave impedance. A complete workflow of our approach is described in Fig. 4.4.
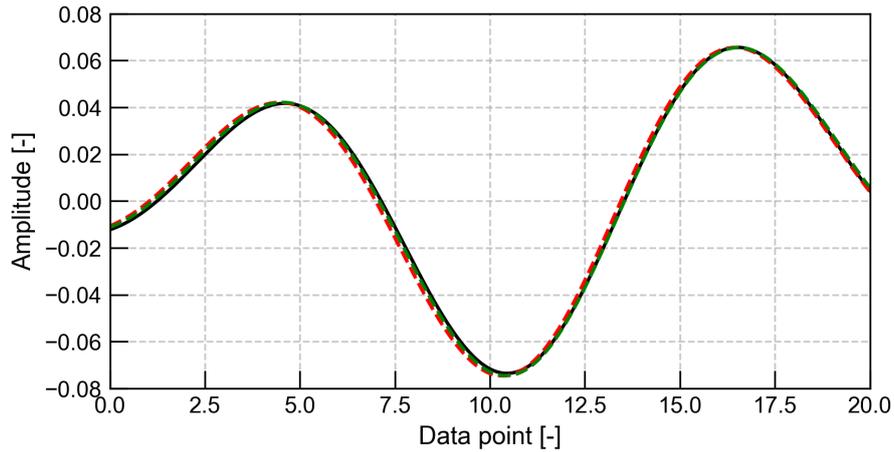
Figure 4.2: A comparison between the first arrival waveform of an observed trace (black), a modeled trace after velocity inversion (dashed red), and the same modeled trace after temporal phase resemblance (dashed green). A tiny phase lag between the waveforms—the black and red lines—gives rise to errors in the impedance inversion.
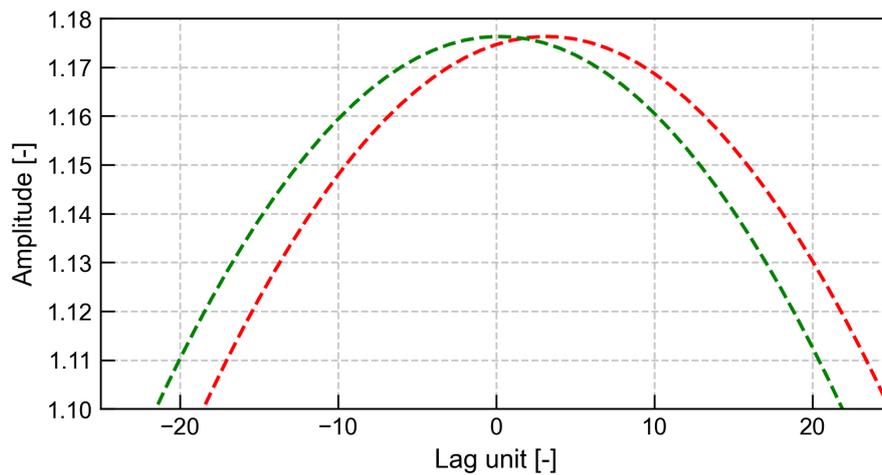
Figure 4.3: Cross-correlation of the observed and the modeled traces in Fig. 4.2 between -25 and 25 lag units before (red) and after (green) phase correction. The peak of the red curve is not at zero lag while that of the green curve is at zero lag.
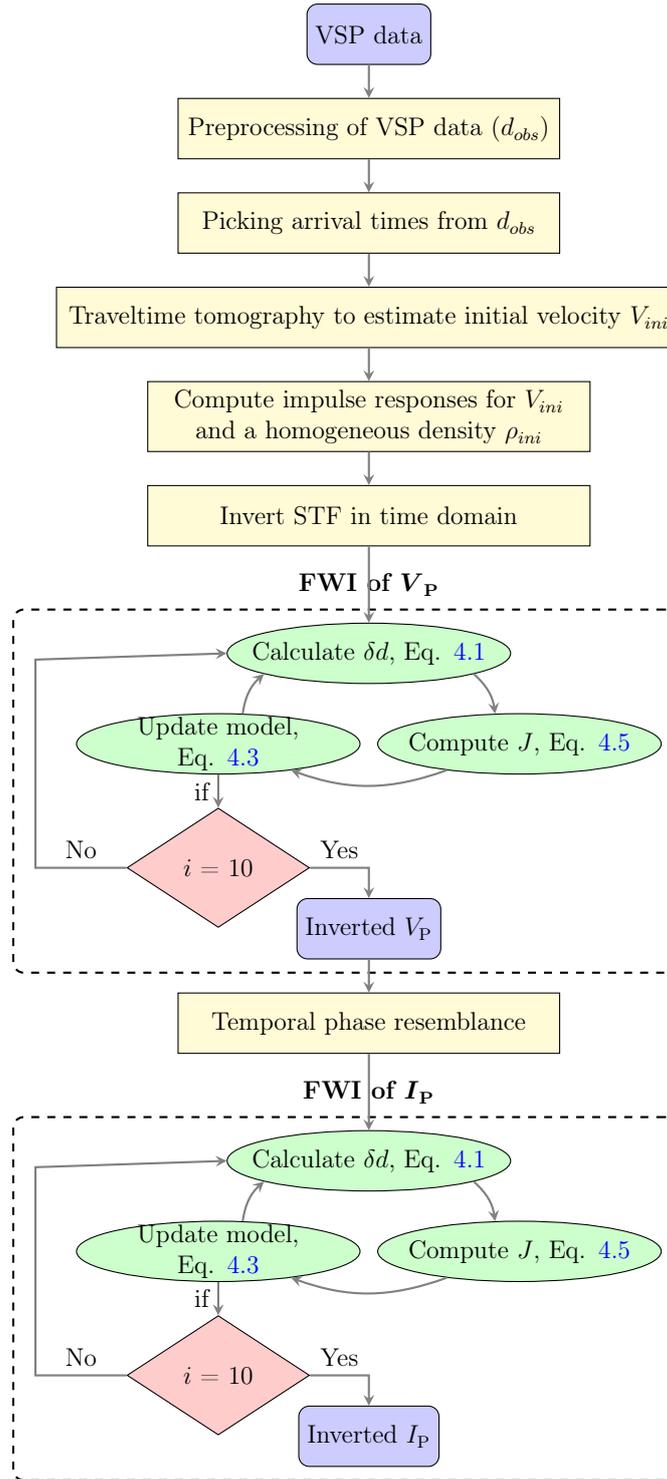
Figure 4.4: Flowchart of the FWI approach, starting from raw VSP data. STF stands for source time function. The yellow rectangles indicate processes while the green ovals indicate repeated processes. The number of iterations (i) in each FWI algorithm is arbitrary.

4.4 Preprocessing

We first followed a standard preprocessing workflow for the vertical component of the seismic vibrator data, as outlined in Table 4.1. The preprocessed data in Fig. 4.5 show clear transmitted and reflected P waves, multiples, and weak transmitted S waves. Given the proximity of the vibrator location to the well, a significant amount of seismic energy was transferred to the borehole fluid, generating tube waves with a velocity of around 1.5 km/s. These tube waves obscure the S waves and some of the reflected P waves.

Various methods have been developed to remove tube waves, differing in complexity and efficiency depending on seismic data (Hardage, 1981; Hu and McMechan, 1987; Falk et al., 1996; Herman et al., 2000). We adopted a straightforward and effective approach based on the separation and subtraction of tube waves. As can be seen in Fig. 4.5, most of the seismic energy is concentrated in the transmitted P-waves and the reverberations shortly after. These events occur earlier than the tube waves, which facilitates their separation. To obtain the tube waves, we applied a mute in the time-distance (t-x) domain starting at 0.56 s on the first trace and linearly increasing to 1.1 s on the last trace. The tube waves remain intertwined with other seismic events, including reflected P waves, multiples, and S waves.

To suppress the tube waves and other sources of noise, i.e. random and liner noise, we transformed the muted data to the frequency-wavenumber (f-k_z) domain, where they were dispersed across a broad spectrum of frequencies and wavenumbers. More importantly, the remaining body waves were separated and restricted to a small area. By masking this confined body waves energy, we got an estimate of the tube waves and noise. Given that seismic traces are the sum of different signals, unwanted tube waves and noise were removed by a simple subtraction from the f-k_z transform of the preprocessed data in Fig. 4.5. Finally, the data were transformed back into the (t-x) domain, as shown in Fig. 4.6. Direct S waves are now traceable at the depths where they were previously masked by the tube waves, and the noise from the production liner between 2340 and 2410 m has been significantly reduced. The random noise on the 1520 m trace has also been heavily attenuated. Importantly, the P-wave amplitudes are preserved after this preprocessing step, ensuring the integrity of the data.

The preprocessing steps described above have prepared the field VSP data for FWI by increasing the SNR, having amplitudes of vertical component. The tube waves cannot be exactly modeled and they will be a source of noise impacting the SNR of the VSP data if not removed. In the next section, we will describe the methodology for inverting the preprocessed data, focusing on leveraging the entire waveform in seismic data to extract detailed P-wave velocity and impedance models.

Processing step	Benefit
Stacking data from multiple sweeps	Increases SNR
Correlation with vibrator sweep	Enhances temporal resolution and increases SNR
Correction for geophone azimuth and inclination	Gives purely vertical particle velocity
Filtering out tube waves	Increases SNR and revealing subsurface seismic events

Table 4.1: Preprocessing steps of the vertical component of the Munich VSP data. The first three steps are standard. The proximity of the source to the well gives rise to tube waves, which necessitates the fourth step.
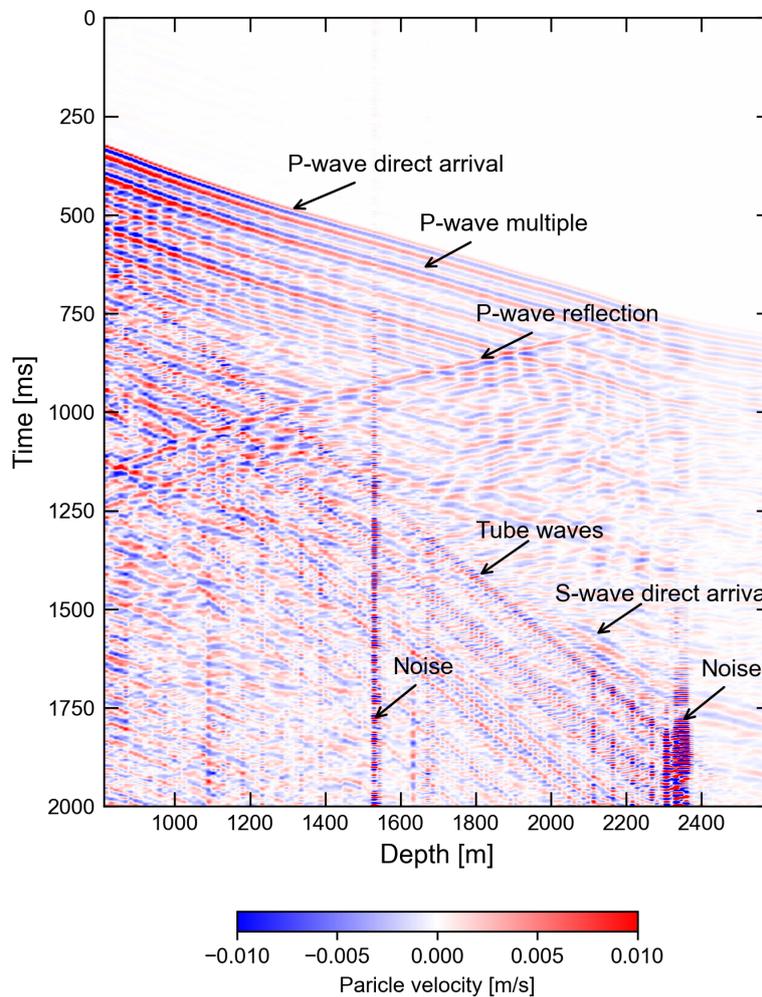
Figure 4.5: Vertical component of the Munich VSP data after the first three preprocessing steps in Tab. 4.1. In order to better visualize the later arrivals, a time-dependent linear gain function has been applied to this data and all following data. Reverberations (multiples) are noticed shortly after the direct arrival. They were generated in the 800 m where data are absent. A strong reflection is created at 2250 m, below which the direct P wave is weaker and wider due to the absence of high frequencies. The S waves are mostly covered or hidden by stronger tube waves. Noise at 2300 m is due to the well completion.
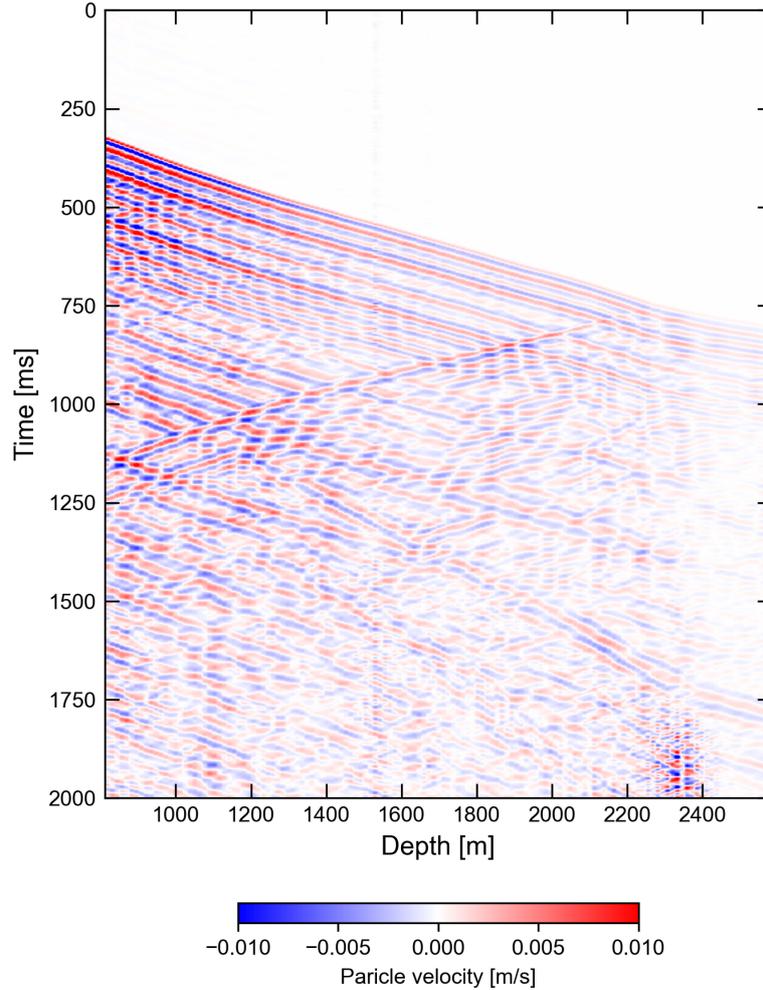
Figure 4.6: Vertical component of the Munich VSP data after tube waves removal. The S waves can be tracked from 1100 m downwards. Noise at 2300 m is significantly reduced.

4.5 FWI results

4.5.1 Approach validation - synthetic data

In this section, we validate our approach by inverting elastic synthetic data with the same source-receiver geometry as the field data. To generate such data, V_P and V_S models are determined from the sonic logs by smoothing with a 201 points Gaussian filter and correcting for dispersion. Fig. 4.9 shows the resulting V_P profile. The ρ model is calculated using Gardner's relationship for sedimentary rocks, i.e. $\rho = 0.31\,V_P^{0.25}$ (Gardner et al., 1974). To produce synthetic waveforms, impulse responses are generated with a sampling interval (dt) and a number of samples (N_s) equal to 0.004 s and 512, respectively. The impulse responses are then convolved with a Klauder wavelet. This Klauder wavelet $K(t)$ has a frequency range similar to the field data, 10 to 80 Hz, and is given by Geldart and

Sheriff (2004),

$$K(t) = real \left[\frac{sin(\pi t \Delta f \, (t_d - t)}{\pi t \Delta f} e^{2\pi i t f_0} \right], \tag{4.8}$$

where t denotes time, Δf equals 35 Hz and defines the rate of change of frequencies with the duration (t_d), which is equal to 2 s. f_0 is the frequency average and equals 45 Hz. We bandpass-filter the synthetic data between frequencies of 10 and 35 Hz to get the data shown in Fig. 4.7.

Acoustic FWI of elastic synthetic data

For an initial model, we use traveltime tomography of the arrival times calculated for the true model. This inversion starts with a homogeneous average velocity of 2.9 km/s below 800 m, while above is set to the true model, Fig. 4.9. The regularization parameters α and β equal 0.05 and 0.5, respectively. After 50 iterations, the inverted V_P profile, see Fig. 4.9, reduces the arrival-time error ϵ_d from 0.13 to 0.0005. Although a high data fit was achieved, the tomographic model shows small contrast between layers. After estimating the STF from the filtered synthetic data, initial full-waveform data are modeled for the tomography V_P profile with a homogeneous ρ of 2400 kg/m^3 as shown in Fig. 4.7.

We investigate the performance of the FWI algorithm in retrieving V_P from the elastic data in Fig. 4.7 using acoustic modeling. We set α and β values both to 10^{-3}. The perturbation amount Δm_q is 10^{-4} and does not change with iterations. We tested values ranging from 10^{-6} to 10^{-1} and noted that small values led to low sensitivities and minimal updates, whereas large values caused large updates and cycle skips. Fig. 4.8 shows the calculated data for the final model obtained from FWI, with all the reflections recovered. The quantity ϵ_d decreased from 0.173 to 0.138 by the first iteration and stayed around 0.137 from the fourth to the tenth iteration. This convergence behavior indicates the nearly linear behavior of the inverse problem; moreover, the inverted model is close to a global minimum. Fig. 4.9 shows a comparison between the true, initial, and inverted models. Moderate model errors are in the depth interval 2300 to 2500 m, where the velocity contrast with the top layer is more than 2 km/s resulting in strong reflections and weaker transmissions. In addition, this interval has the deepest receivers with normally the lowest amplitudes.
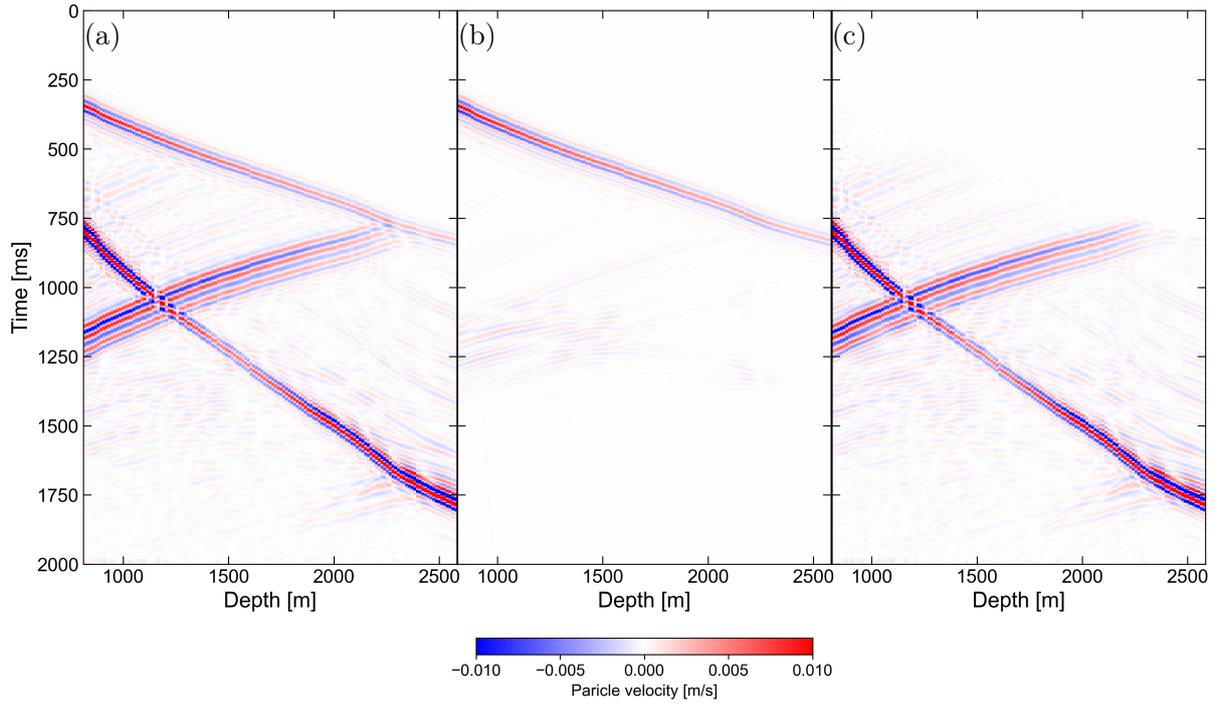
Figure 4.7: Vertical component of the elastic synthetic/true data after applying a band-pass filter from 10 to 35 Hz (a), initial data (b) and their difference (c). In the true data, there are several P reflections. Strong reflections appear at 2200 m despite the decrease in reflections strength with depth. The initial data does not have all reflections. Because of the selected length of the time window to estimate the STF, a slight difference is encountered before the direct arrival.
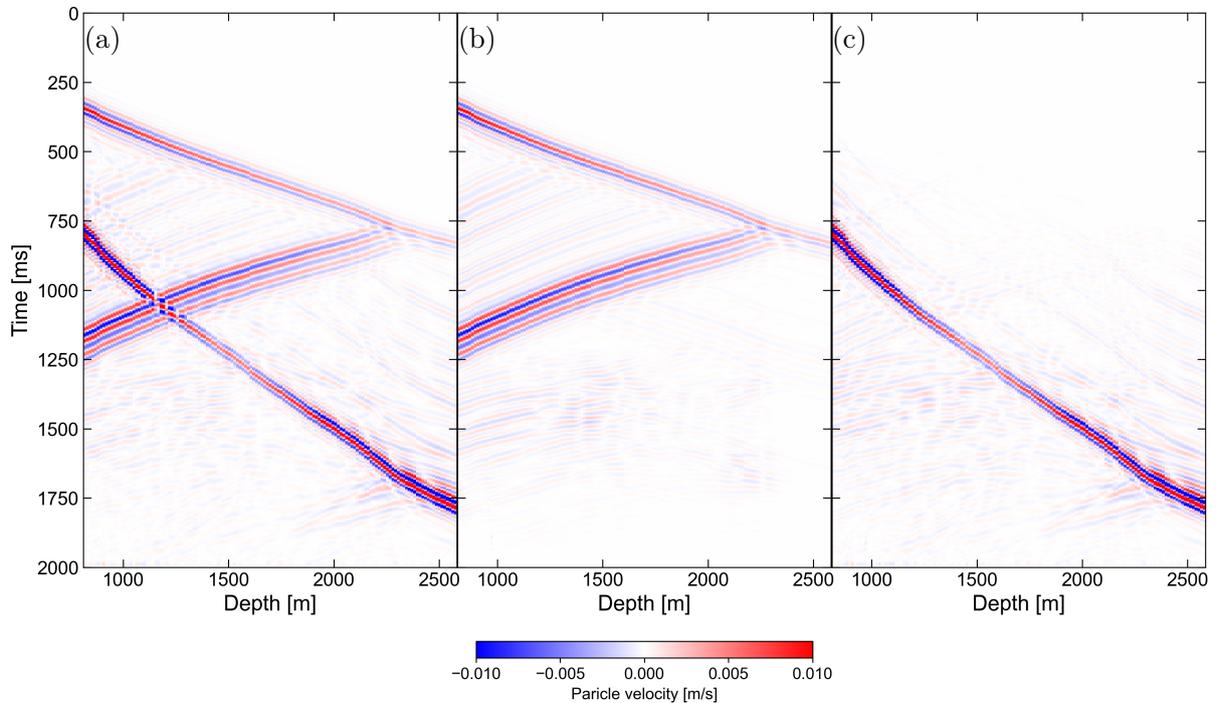

Figure 4.8: The true data in Fig. 4.7 (a), inverted/calculated data (b) and their difference (c). The calculated data exhibits P reflections, which reduces the difference of these events with the true data. The difference of the direct P-waves has also been reduced. In general, phase errors occur regardless of the significant model fit.
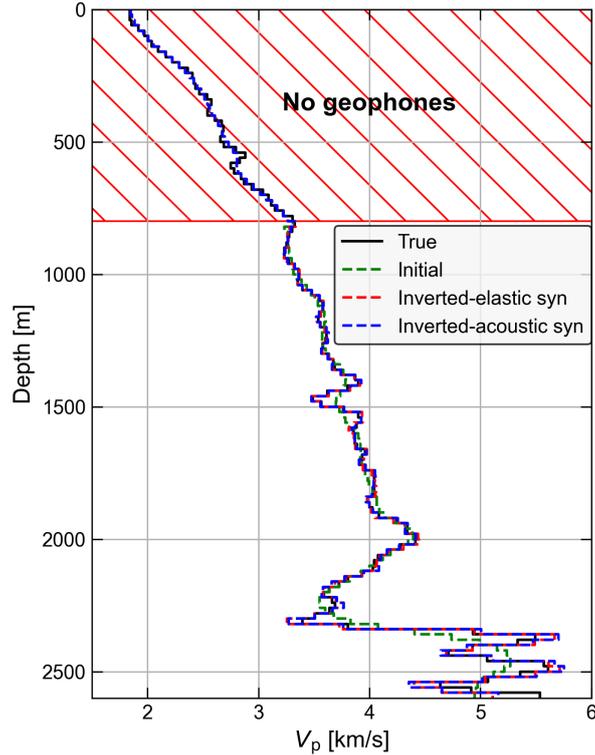
Figure 4.9: The true, initial, and inverted V_P models from elastic and acoustic synthetic data. In the shallow 800 m, the model is kept fixed because there are no receivers. The initial model shows a low resolution to the inverted models. The FWI of both elastic and acoustic true data achieves a superior fit to the true model.

In a regular sequential approach, the FWI of P-wave impedance is performed directly after V_P. To calculate the sensitivities, V_P is perturbed by 10^{-4} and ρ by 10^{-2}. The larger perturbation of density is required to balance the higher sensitivity of seismic data to velocity. We adjust α and β to 1 and 10, respectively. We show in Fig. 4.11 that following such an approach can give mixed results, depending on the errors from the former inversion. Above the reservoir, the velocity is estimated with slight errors, which is the same as for the impedance. The high velocities of the reservoir, 4.7-5.5 km/s, were difficult to estimate accurately, Fig. 4.9. For both the elastic and the acoustic true data, the total error in the estimation of the P-wave impedance in the area representing the reservoir is approximately 6.50 % and can be greater than 12 % in a few layers. Such errors values are above the tolerance level that is required in real-world applications, emphasizing the need for more advanced FWI approaches.

We apply temporal phase resemblance to eliminate the effects of small phase-shift errors. The data misfit ϵ_d is reduced by 0.42 % with the first iteration and by 0.44 % with further iterations. Regardless of this small percentage, the calculated data in Fig. 4.10 fit visibly better. The resulting P-impedance model from acoustic FWI of elastic true data is in Fig. 4.12, which shows 98.8 % fit with the true model. The most significant improvement is

between 1500 and 2600 m depth, especially in the reservoir area. Crucially, the inverted model is not affected by the fixed values in the shallow 800 m, which are higher than the true values. The robust estimation of the STF helps to cancel the errors due to these fixed values.
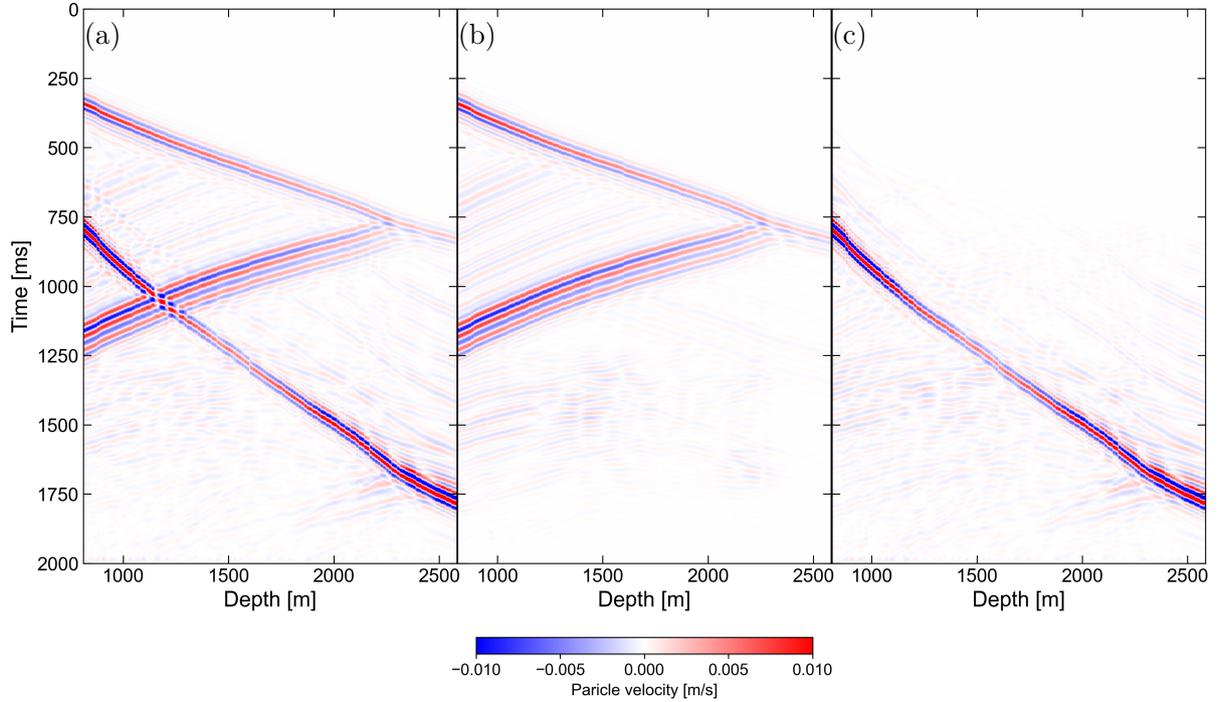
Figure 4.10: The true data in Fig. 4.7 (a), the calculated data after acoustic FWI (b) and their difference (c). The difference of the direct P-arrival is negligible. Deep reflections also show smaller difference compared to Fig. 4.8.

Acoustic FWI of acoustic synthetic data

We also investigate FWI of V_P from acoustic true data to see how the resulting model compares to that of the previous inversion. In this case, ϵ_d decreases from 0.115 to 0.039 in one iteration, then stays around 0.022 after the third iteration. FWI with acoustic synthetics achieves 1.97 % higher data fit than that with elastic synthetics. This is expected because acoustic inversions of acoustic data do not suffer from the P-to-S mode conversions present in the elastic data. Still, the model fit in the two cases is more or less the same as demonstrated in Fig. 4.9. Hence, the acoustic approximation is appropriate for FWI of V_P, significantly saving computation time. Next, we examine the validity of the acoustic approximation for FWI of P impedance.
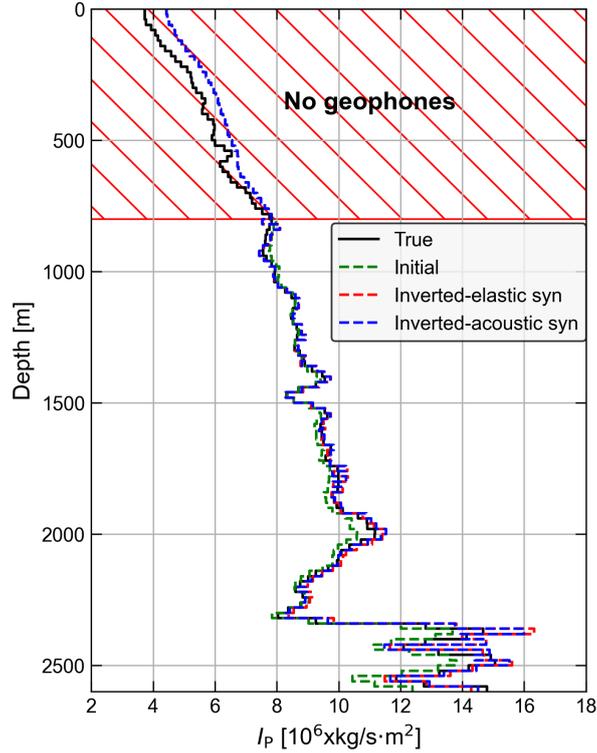
Figure 4.11: The true, initial, and inverted impedance models without applying phase resemblance. In the shallow 800 m, the model is kept fixed due to missing data and the impedance is put higher than the actual one because the initial ρ is 2400 kg/m^3. The inverted values within the reservoir are largely in mismatch with the true values.

Continuing with acoustic true synthetics, we use the temporal phase resemblance approach to eliminate the further effect of small phase-shift errors, which reduces ϵ_d to 0.02. The FWI of acoustic impedance further reduces the data misfit to 0.015. A reduction in the data misfit by 0.005, Fig. 4.10, improved the model by 4 %, as seen in Fig. 4.12. The most significant model improvement is also between 1500 and 2600 m deep. A comparison of the inverted models in Fig. 4.12 shows that our approach to the impedance FWI is independent of the nature of the true data. Thus, acoustic FWI of P impedance from elastic true data is a valid assumption.
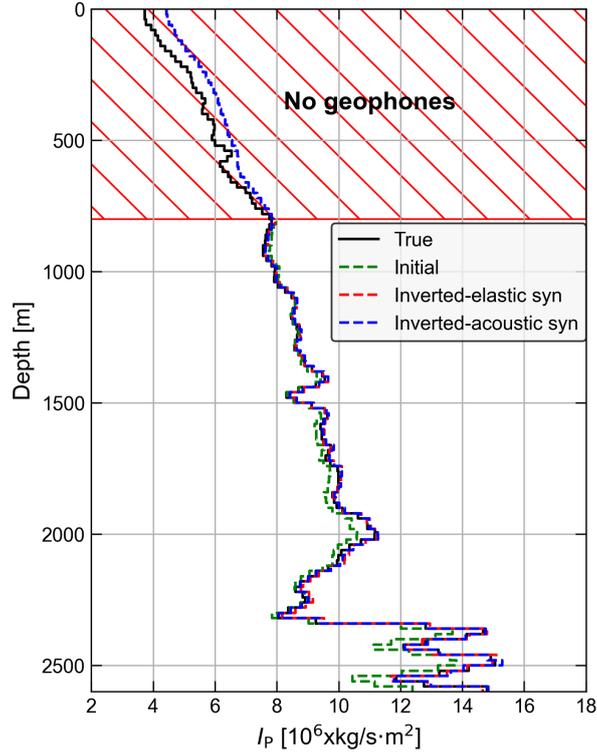
Figure 4.12: The true, initial, and inverted impedance models. In the shallow 800 m, the model is kept fixed due to missing data and the impedance is put higher than the actual one because the initial ρ is 2400 kg/m^3. The initial model is close to the true model from 800 to 1500 m deep and relatively far from the true model below 1500 m. The inverted impedance model has a greater fit to the true model.

4.5.2 Field data application

As demonstrated in Section 4.5.1, the influence of V_S on the estimation of acoustic impedance using FWI is negligible. Thus, we consider S waves in the Munich VSP (field) data to be undesired noise because (1) they have relatively low sensitivity to temperature changes, (2) their direct arrival has low amplitudes—intricate recovery of a high-resolution V_S model via FWI, and (3) using simplified V_S models, for example from traveltime tomography, will not fit P-to-S modes, and in turn the residuals and the gradients will be erroneous for the FWI of acoustic impedance. When it comes to the short-time multiples, they start appearing some 0.1 s with large amplitudes after the transmitted P wave, Fig. 4.6. Although these multiples carry some information on the shallow, 800 m, subsurface, relying solely on them would not provide a robust model estimation. Moreover, they interfere with the reflections, limiting the value of these latter events as a source of information for FWI. To remove the S waves and the multiples, we filter out their distinct energy patterns in the f-k_z domain, as shown in Fig. 4.14.

Building on the promising results from the inversion experiments with synthetic data,

we applied the methodology to the VSP data collected at the Munich geothermal site. The band-pass filtered data in the frequency range 10 to 35 Hz are shown in Fig. 4.14. We choose the lowest possible frequency range because the attenuation effect is relatively minimal, and so we can assume a lossless medium. Reflections starting from depths that are not covered by the receivers array are removed. As a starting model, traveltime tomography uses picked arrival times to estimate the velocity between 800 and 2600 m deep. the shallow part is fixed to a velocity increasing downwards during the tomography. The initial V_{P} in Fig. 4.17 is achieved with 50 iterations and reducing ϵ_d to 0.004.

For the V_{P} FWI, a homogeneous ρ of 2400 kg/m^3 is assumed. Computed impulse responses are used to estimate the STF in Fig. 4.13. As shown in the middle of Fig. 4.14, the initial waveform data do not have any of the reflections as observable in the field data (left of Fig. 4.14). Moreover, the waveform differences in the direct arrivals exhibit systematic patterns, indicating poor data fit. During the FWI process, ϵ_d is minimized from 0.217 to 0.0983 within 5 iterations, as shown in Fig. 4.15. The calculated data with the inverted model fit the field data well and have most of the reflections present. Reflections from the geothermal reservoir change paths—suddenly bend—as they travel upwards. This might be due to subsurface heterogeneity that cannot be resolved by a stratified model. The recovered reflections are generated by velocity contrasts in the inverted model, Fig. 4.17. In the depth range 800 and 2000 m, the velocity contrast increases with depth from 0.5 to 1 km/s, however, the reflectivity decreases. Interestingly, all these reflections down to the top of the geothermal reservoir are recovered, thereby indicating the high resolution.

Accurate estimation of impedance from the field data should give more insights into the Munich geothermal site. As shown in Fig. 4.16, there are several waveforms that have not been fitted completely. Temporal phase resemblance further reduces ϵ_d to 0.0875—1 % better fit of the data by reducing phase errors. This percentage is larger than the influence of impedance on seismic data as expected from the results in section 4.5.1. This FWI begins with the starting model in Fig. 4.19. After the first iteration, ϵ_d decreases to 0.0864 and stays around this value for subsequent iterations. The actual value of ϵ_d is difficult to calculate because of the numerical noise (i.e. multiples) that increases by updating the impedance. A small reduction in ϵ_d is in line with the synthetic experiments. In addition, the difference between the initial data and the data calculated for the final model is about 1.5 %. The impedance is updated by temporal phase resemblance of 4 % as shown in Fig. 4.19. The largest updates are observed within the reservoir. The impedance structure is mostly in agreement with the velocity structure, thereby building confidence in the estimated properties. Within the reservoir, impedances show clearer layering than velocities.
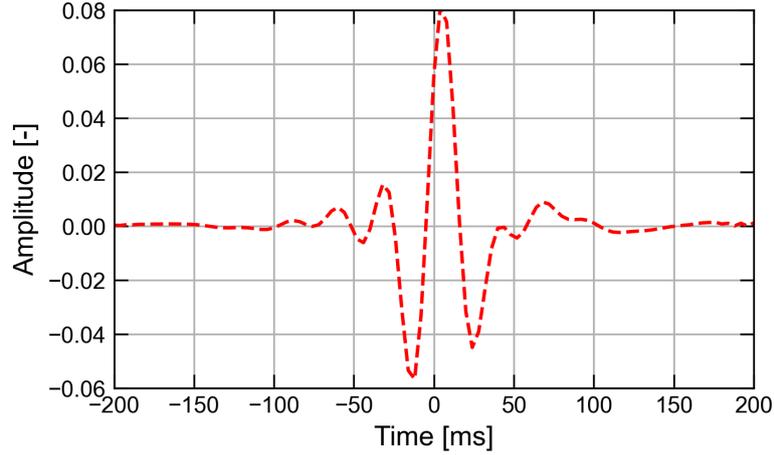
Figure 4.13: The inverted STF from the field VSP data. The wavelet does not have zero lag because of the attenuation of high frequencies.
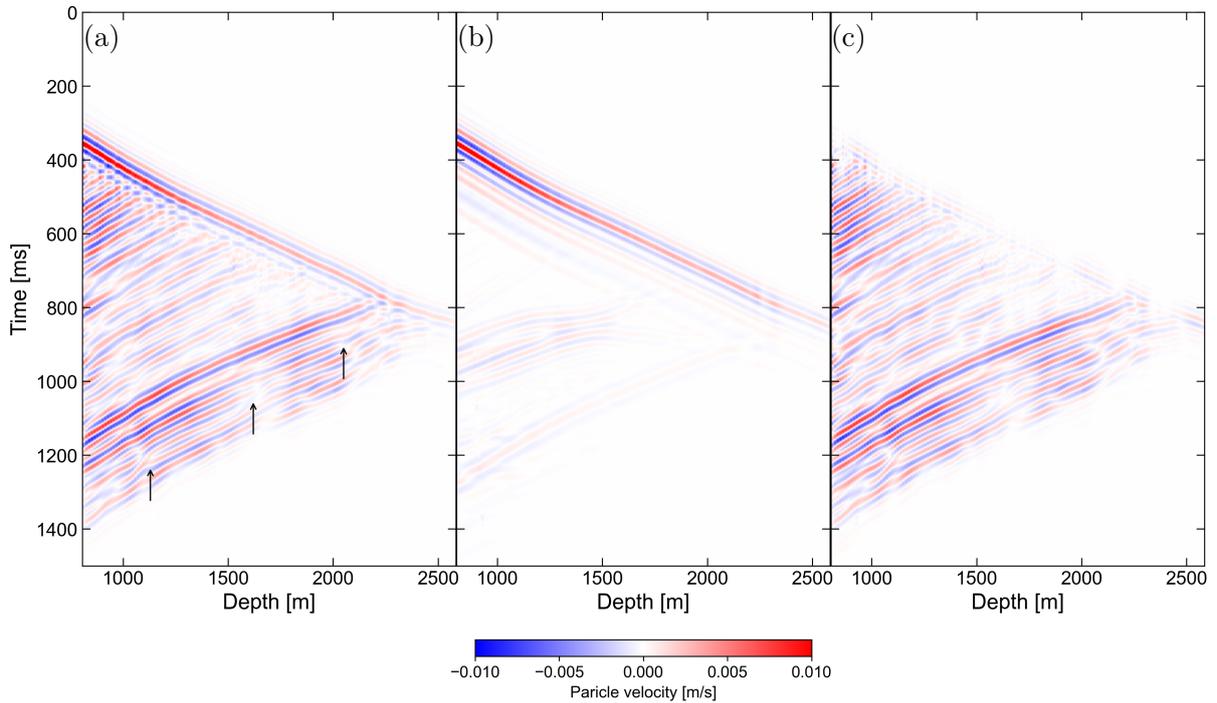

Figure 4.14: Comparison between field data and initial data with V_P from traveltime tomography. The preprocessed field data after applying a 10–35 Hz Butterworth filter (a), initial waveform data after traveltime V_P inversion (b) and their difference (c). The filter, which passes frequencies in the range of 10 to 35 Hz, has an order of 4 to lessen Gibb's phenomenon (Pinsky, 2023). A strong reflection appears at 2200 m. Latter reflections appear weaker and split with time as pointed in some places by the black arrows. The initial data do not have reflections.
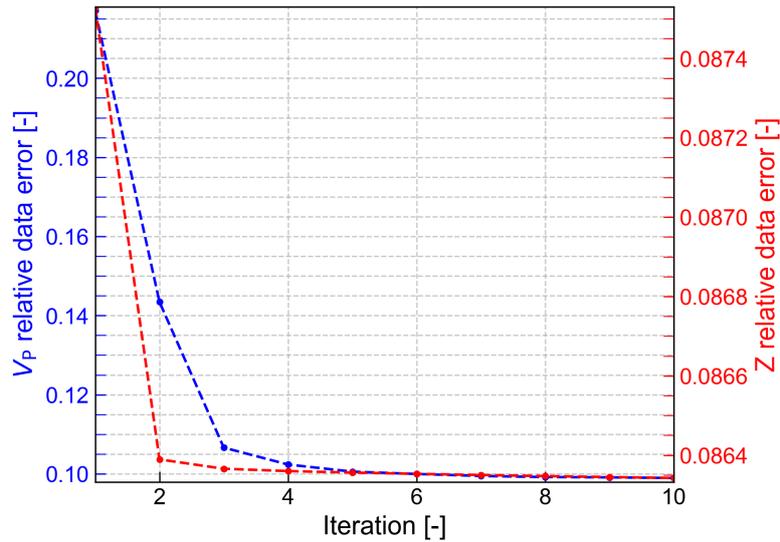
Figure 4.15: The behavior of ϵ_d with iterations during FWI of V_P (blue line) and P-impedance (red line). The blue line needs five iteration to become flat—indicating non linearity of V_P inversion. The red line becomes almost flat after the first iteration—indicating linear P-impedance inversion.
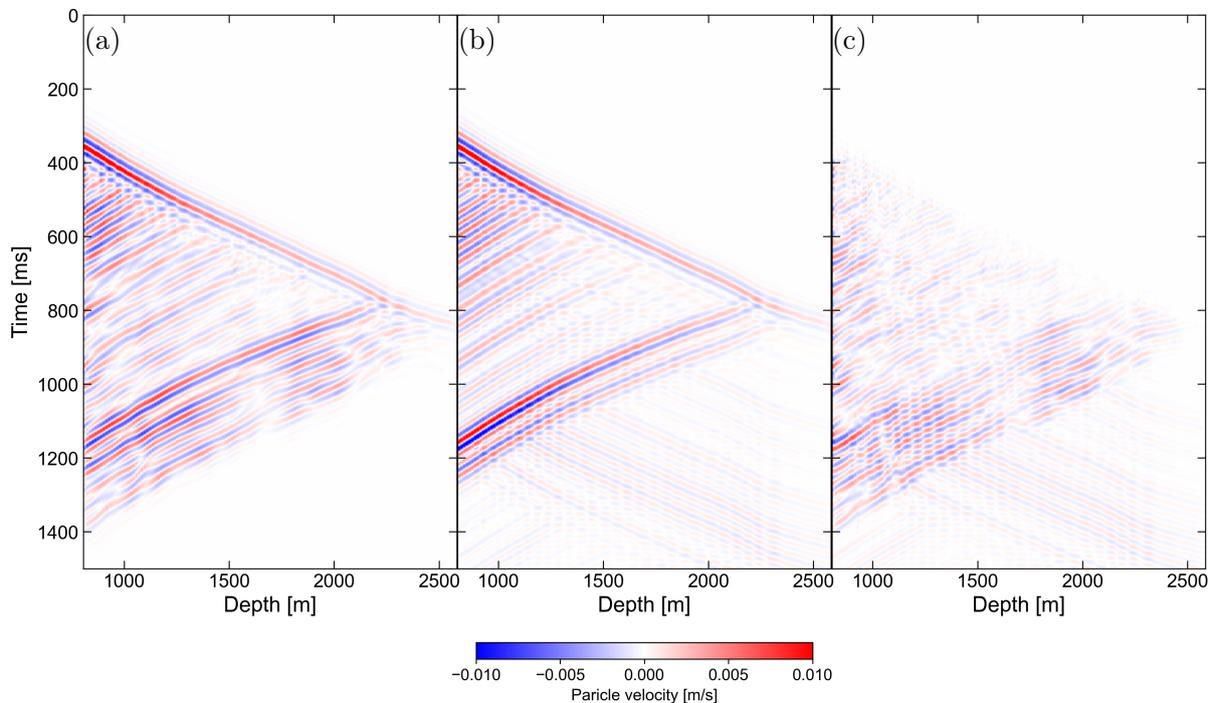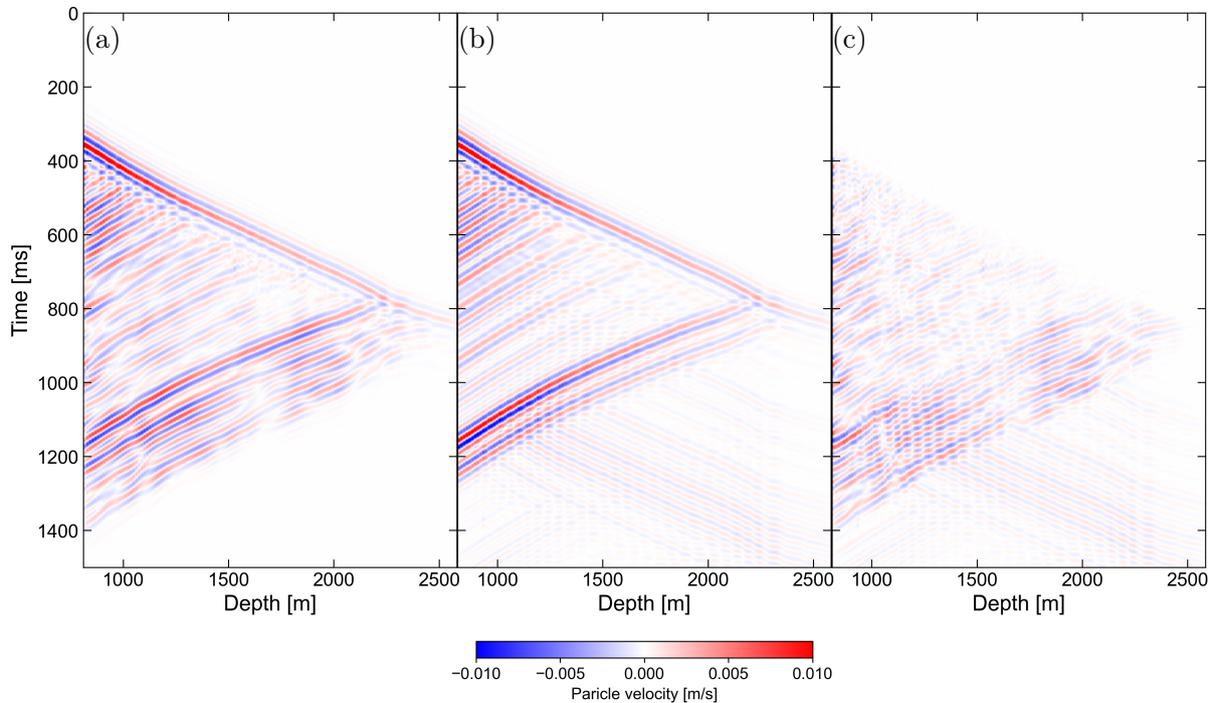

Figure 4.16: Data comparison after V_P FWI. The preprocessed field data after applying 10–35 Hz Butterworth filter (a), calculated data with inverted V_P (b) and their difference (c). The calculated data show most of the reflections in addition to some multiples. The difference has no distinct pattern on the direct arrival and the majority of reflections, proving adequate fit.
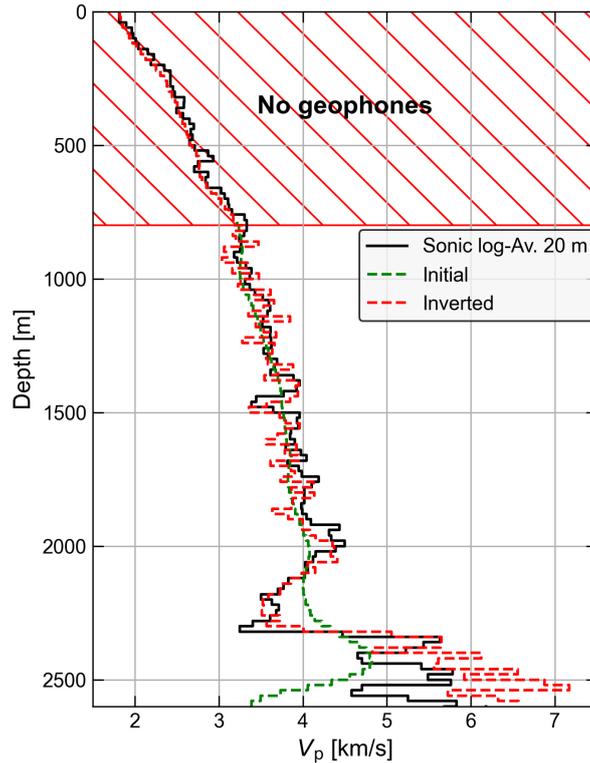
Figure 4.17: The initial and full-waveform-inverted V_P models, where the shallow 800 m is identical. The initial velocity develops smoothly as a function of depth, indicating low resolution. The inverted model has many velocity contrasts and has significantly large velocities in the reservoir area, typical of carbonate rocks.

Figure 4.18: Data comparison after impedance FWI. The preprocessed field data after applying 10–35 Hz Butterworth filter (a), calculated data with inverted impedance (b), and the difference (c). The calculated data show many exacerbated multiples. The differences are small on the location of the direct arrival and some reflections.
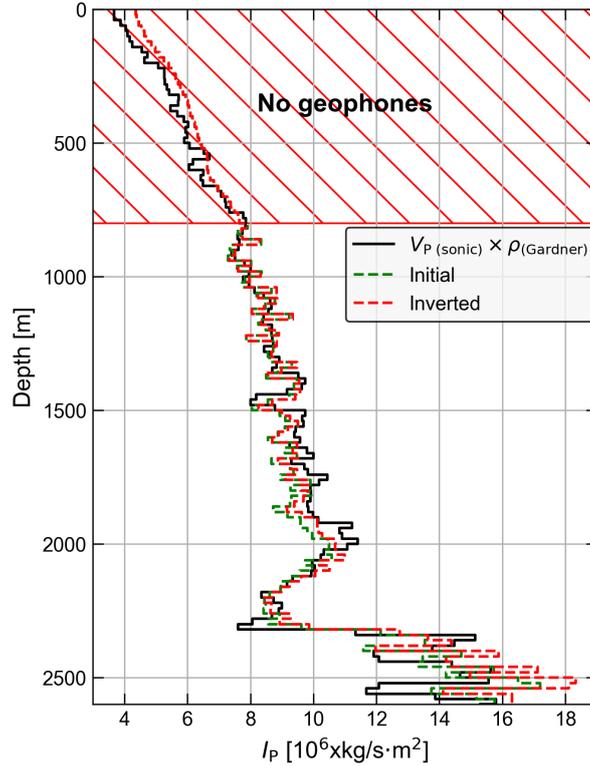
Figure 4.19: The initial, and inverted acoustic impedance models. In the shallow 800 m, the model is identical. Impedance is updated at different depths, the most significant in the area around 2000 m and within the reservoir.

4.6 Discussion

The application of our FWI approach to the Munich VSP data provided more information on the subsurface velocity and impedance structures. Updating the initial model resulting from traveltime tomography achieved 55 % improvement in data fit within just a few iterations. Deep reflections from the reservoir were not all recovered due to their complex wavefront trajectory, suggesting the presence of heterogeneities that are not resolvable with a layered model. All other reflections in the overburden were accurately captured with a layered V_P model. A decrease in velocity between 2000 and 2300 m is probably linked the lithology alteration from sandstones to marls. This is followed by a 2 km/s velocity contrast, marking the transition into the carbonate Lithothamnium Kalk formation, which was not recovered by traveltime tomography. The Purbeck-Malm reservoir starts at a depth of around 2420 m and only the uppermost 160 m section is covered by the data, where there is generally an increase in average velocity from around 4.5 to 6.5 km/s. This general trend is intercalated by velocity deviations of approximately 0.5 km/s. However, it is difficult to predict the productive zones from the seismic data alone, as significant diagenesis occurred. Because the sonic logs within the reservoir have poor data quality, the velocity could not be correlated with the porosity data.

The impedance model further improved the seismic characterization at the Munich geothermal site. The impedances, Fig. 4.19, have a clear correspondence with the velocities, Fig. 4.17. The use of temporal phase resemblance was very important in cancelling the phase errors, which are greater than 1 %, and if not corrected, a meaningful impedance model of the Munich geothermal site would not have been estimated. The faster convergence of the impedance FWI is attributed to the linearity of the inverse problem; see Fig. 4.15. The recovered impedance provided additional details, particularly within the reservoir zone, where the values below 14×10^6 kg/s·m^2 are typical of permeable and saturated carbonate rocks. Higher impedance values are coinciding with higher velocities, further referring to compact rocks. This further emphasized the reliability of the FWI approach in characterizing the subsurface in the context of seismic monitoring of low-enthalpy reservoirs. The effectiveness of this approach should be further examined when multi-offset-VSP data is used in conjunction with 2D and 3D heterogeneous media to allow tracking volumetric changes of temperature over time.

This study aimed at demonstrating the effectiveness of our sequential FWI approach in retrieving layered impedance models from field VSP data. The inversion experiments based on synthetic data were used for validation. In these experiments, the true model had more than 2.5 km/s contrast between the deepest 300 m and the overburden, as well as 1 km/s fluctuations within the deepest area itself, posing significant challenges for velocity recovery. In the final inverted model, the values in the deepest part m are either overestimated or underestimated by 0.2 km/s (3.4 %) on average, probably due to several factors: (1) the initial mass density (ρ) is lower than its actual values, resulting in matching uncorrelated phases, (2) low sensitivity due to low amplitudes of the waveforms, and (3) limited data constraints with a smaller number of direct arrivals in that area. Jointly inverting velocity and impedance could potentially tackle the first issue. At the same time, it may also amplify errors if impedance is updated with already uncorrelated waveforms.

These errors in the inverted V_P profile are significant and will prevent the capture of a 1 % velocity change. Fig. 4.20 shows the base and monitor states, as well as their inverted models. The inverted V_P has 3.8 % disagreement with the true monitor model. More importantly, the difference between the inverted models for the two states does not also give the variation. On other hand, the variation in impedance is larger, making it more relevant to geothermal applications. Our FWI approach does not rely on estimating relative impedances, rather on absolute ones, which abolishes the necessity for incorporating S-wave information as in approaches that depend on the Zoeppritz equations (Shuey, 1985; Wang, 1999). However, it was not clear whether an error in impedance at a certain depth that is not related to cross-talk or trade-off would affect deeper impedance.
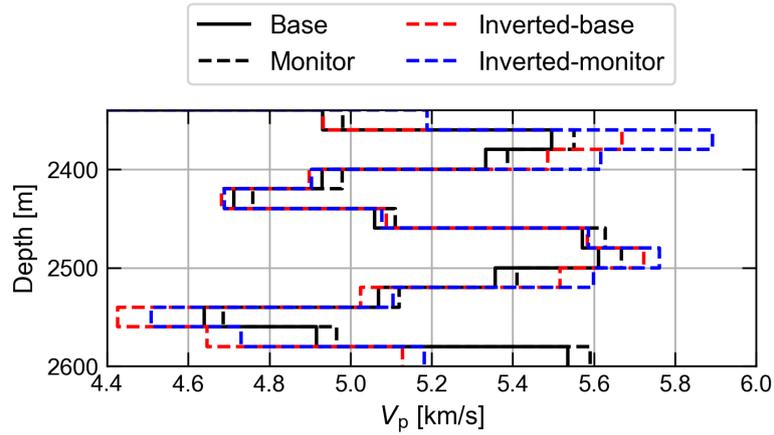
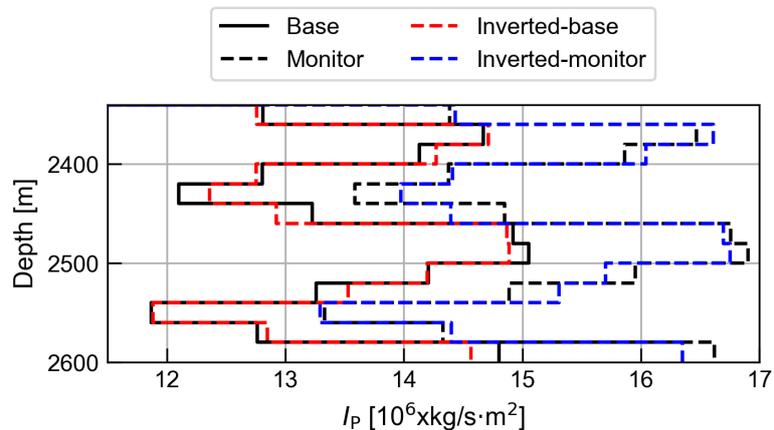**Figure 4.20:** A comparison between the base and the monitor velocity state as well as their inverted models. The inverted models, especially for the monitor case, have a large errors from the true models. This errors vary among layers, moreover, they are not correlated between the inverted models.

The data acquisition setup does not have constraints in the upper 800 m, where fixed impedance values were assumed. A robust STF estimation helped cancel the shortcomings associated with such an assumption and preventing deviation from the actual values, as shown in Fig. 4.12. In the synthetic experiments, we characterize the impedance in the layers representing the geothermal reservoir—last 240 m—with an error less than 1 %. Assuming a monitor state where impedance increases by 12 % in the last 240 m, we can still detect the variation as shown in Fig. 4.21. The difference between the inverted base and monitor states is 12.3 % and has slightly less than 2 % disagreement with the actual difference. These findings highlight the potential of FWI to detect and quantify impedance variations, which would give the amount of temperature change.

Figure 4.21: A comparison between the base and the monitor impedance state as well as their inverted models. The inverted models have a minor divergence from the true models. This divergence varies among layers within a model, however, it is mostly correlated between the inverted models.

Overall, our study highlighted the potential of sequential FWI combined with phase resemblance in the delivery of high-quality acoustic impedance models. The successful inversion of the observed synthetic and field data confirms the robustness of the method and its applicability to complex subsurface structures such as those found at the Munich geothermal site. The ability to extract accurate velocity and impedance profiles has significant implications for understanding geothermal reservoirs, which can provide key information for heat production.

4.7 Conclusions

We have successfully developed a sequential FWI approach combined with temporal phase resemblance to retrieve layered impedance models of the Munich geothermal site. The numerical experiments with the same survey setup (i.e., only a single source location was deployed) proved that our approach can achieve approximately 99 % accuracy in estimating the acoustic impedance. The acoustic impedance was better resolved than the velocity, making it more relevant seismic property for the monitoring of geothermal energy production. The deployment of initial models from traveltime tomography ensures the convergence of FWI to optimal V_{P} models, even in the presence of substantial contrasts. Thus, the computational time of FWI is significantly reduced. Acoustic FWI is applicable to elastic VSP data, when the goal is to recover acoustic properties. Thus, the efficiency of our FWI approach is high and suitable for real-world applications in retrieving complex 2D or 3D models with multiple source locations.

The FWI of the VSP data provided more details than traveltime tomography, proving its value in high-resolution seismic characterization of the Munich geothermal site. The assumption of a 1D model is valid for the overburden of the Munich geothermal reservoir. Consequently, future monitoring can be target-oriented with a stratified overburden. Our method holds significant potential and warrants further research to incorporate multi-offset data to offer more detailed models (2D or 3D heterogeneous structure) of low-enthalpy reservoirs, needed for optimizing geothermal heat production and further supporting the energy transition.

References

Agemar, T., Schellschmidt, R., and Schulz, R. (2012). Subsurface temperature distribution in Germany. Geothermics, 44:65–77.

Asnaashari, A., Brossier, R., Garambois, S., Audebert, F., Thore, P., and Virieux, J. (2012). Time-lapse imaging using regularized FWI: a robustness study: 82nd Annual International Meeting, SEG, Expanded Abstracts, 1–5.

References

Axelsson, G., Stefánsson, V., and Xu, Y. (2003). Sustainable management of geothermal resources. In Proceedings of the International Geothermal Conference, pages 40–48. Citeseer.

Bachmann, G., Müller, M., and Weggen, K. (1987). Evolution of the molasse basin (Germany, Switzerland). Tectonophysics, 137(1-4):77–92.

Batzle, M. and Wang, Z. (1992). Seismic properties of pore fluids. Geophysics, 57(11):1396–1408.

Bödvarsson, G. S. and Tsang, C. F. (1982). Injection and thermal breakthrough in fractured geothermal reservoirs. Journal of Geophysical Research: Solid Earth, 87(B2):1031–1048.

Bohnsack, D., Potten, M., Pfrang, D., Wolpert, P., and Zosseder, K. (2020). Porosity–permeability relationship derived from Upper Jurassic carbonate rock cores to assess the regional hydraulic matrix properties of the Malm reservoir in the South German Molasse Basin. Geothermal Energy, 8:1–47.

Brodic, B., Ras, P., de Kunder, R., Drijkoningen, G., and Malehmir, A. (2021). Seismic imaging using an e-vib—A case study analyzing the signal properties of a seismic vibrator driven by electric linear synchronous motors. Geophysics, 86(3):B223–B235.

Cammarano, F., Goes, S., Vacher, P., and Giardini, D. (2003). Inferring upper-mantle temperatures from seismic velocities. Physics of the Earth and Planetary Interiors, 138(3-4):197–222.

Chen, Y., Chen, Y., Fomel, S., Savvaidis, A., Saad, O. M., and Oboué, Y. A. S. I. (2023). Pyekfmm: a python package for 3D fast-marching-based traveltime calculation and its applications in seismology. Seismological Research Letters, 94(1):2050–2059.

Denli, H. and Huang, L. (2009). Double-difference elastic waveform tomography in the time domain. In SEG International Exposition and Annual Meeting, pages SEG–2009. SEG.

Egorov, A., Pevzner, R., Bóna, A., Glubokovskikh, S., Puzyrev, V., Tertyshnikov, K., and Gurevich, B. (2017). Time-lapse full waveform inversion of vertical seismic profile data: Workflow and application to the CO2CRC Otway project. Geophysical Research Letters, 44(14):7211–7218.

Eikrem, K. S., Nævdal, G., and Jakobsen, M. (2019). Iterated extended Kalman filter method for time-lapse seismic full-waveform inversion. Geophysical Prospecting, 67(2):379–394.

Eltayieb, M., Werthmüller, D., Drijkoningen, G., and Slob, E. (2023). Feasibility Study of Controlled-Source Electromagnetic Method for Monitoring Low-Enthalpy Geothermal Reservoirs. Applied Sciences, 13(16):9399.

Ernst, J. R., Maurer, H., Green, A. G., and Holliger, K. (2007). Full-waveform inversion of crosshole radar data based on 2-D finite-difference time-domain solutions of Maxwell's equations. IEEE Transactions on Geoscience and remote Sensing, 45(9):2807–2828.

Falk, J., Tessmer, E., and Gajewski, D. (1996). Tube wave modeling by the finite-difference method with varying grid spacing. Pure and Applied Geophysics, 148:77–93.

Fichtner, A. (2010). Full seismic waveform modelling and inversion. Springer Science & Business Media.

Flechtner, F., Loewer, M., and Keim, M. (2020). Updated stock take of the deep geothermal projects in Bavaria, Germany (2019). In Proceedings World Geothermal Congress, pages 1–10.

Gardner, G., Gardner, L., and Gregory, A. (1974). Formation velocity and density—The diagnostic basics for stratigraphic traps. Geophysics, 39(6):770–780.

Geldart, L. P. and Sheriff, R. E. (2004). Problems in exploration seismology and their solutions. Society of Exploration Geophysicists.

Grant, M. (2013). Geothermal reservoir engineering. Elsevier.

Hardage, B. (1981). An examination of tube wave noise in vertical seismic profiling data. Geophysics, 46(6):892–903.

Herman, G. C., Milligan, P. A., Dong, Q., and Rector, J. W. (2000). Analysis and removal of multiply scattered tube waves. Geophysics, 65(3):745–754.

Herrmann, R. B. (2013). Computer programs in seismology: An evolving tool for instruction and research. Seismological Research Letters, 84(6):1081–1088.

Hicks, E., Hoeber, H., Houbiers, M., Lescoffit, S. P., Ratcliffe, A., and Vinje, V. (2016). Time-lapse full-waveform inversion as a reservoir-monitoring tool—A North Sea case study. The Leading Edge, 35(10):850–858.

Hörbrand, T., Beichel, K., Bendias, D., Savvatis, A., and Kohl, T. (2025). Karst control on reservoir performance of a developed carbonate geothermal reservoir in Munich, Germany. Geological Society, London, Special Publications, 548(1):SP548–2024.

Hu, L.-Z. and McMechan, G. A. (1987). Wave-field transformations of vertical seismic profiles. Geophysics, 52(3):307–321.

References

Jeßberger, J., Uhrmann, H., Schölderle, F., Pfrang, D., Heberle, F., Zosseder, K., and Brüggemann, D. (2025). Medium-deep geothermal resources in the Molasse Basin: A geological, techno-economic, and ecological study of large-scale heat pump integration. Renewable Energy, 248:123147.

Kamei, R. and Lumley, D. (2017). Full waveform inversion of repeating seismic events to estimate time-lapse velocity changes. Geophysical Journal International, 209(2):1239–1264.

Kaya, E., Zarrouk, S. J., and O'Sullivan, M. J. (2011). Reinjection in geothermal fields: A review of worldwide experience. Renewable and Sustainable Energy Reviews, 15(1):47–68.

Kennett, B. L. N. and Kerry, N. J. (1979). Seismic waves in a stratified half space. Geophysical Journal International, 57(3):557–583.

Kinsler, L. E., Frey, A. R., Coppens, A. B., and Sanders, J. V. (2000). Fundamentals of acoustics. John wiley & sons.

Krampe, V., Edme, P., and Maurer, H. (2021). Optimized experimental design for seismic full waveform inversion: A computationally efficient method including a flexible implementation of acquisition costs. Geophysical Prospecting, 69(1):152–166.

Krumbholz, J., Krumbholz, M., Wadas, S., and Tanner, D. (2024). Characterisation of the fracture-and karst-controlled geothermal reservoir below Munich from geophysical wireline and well information. Geothermal Energy, 12(1):9.

Maharramov, M. and Biondi, B. (2015). Robust simultaneous time-lapse full-waveform inversion with total-variation regularization of model difference. In 77th EAGE Conference and Exhibition 2015, volume 2015, pages 1–5. European Association of Geoscientists & Engineers.

Martín-Gamboa, M., Iribarren, D., and Dufour, J. (2015). On the environmental suitability of high-and low-enthalpy geothermal systems. Geothermics, 53:27–37.

Menke, W. (2018). Geophysical data analysis: Discrete inverse theory. Academic press.

Meyer, R. K. and Schmidt-Kaler, H. (1990). Paleogeography and development of sponge reefs in the Upper Jurassic of Southern Germany—an overview. Facies, 23:175–184.

Moeck, I. S. (2014). Catalog of geothermal play types based on geologic controls. Renewable and sustainable energy reviews, 37:867–882.

Muffler, P. and Cataldi, R. (1978). Methods for regional assessment of geothermal resources. Geothermics, 7(2-4):53–89.

Musil, M., Maurer, H., and Green, A. (2003). Discrete tomography and joint inversion for loosely connected or unconnected physical properties: application to crosshole seismic and georadar data sets. Geophysical Journal International, 153(2):389–402.

Nuber, A., Manukyan, E., and Maurer, H. (2015). Enhancement of near-surface elastic full waveform inversion results in regions of low sensitivities. Journal of Applied Geophysics, 122:192–201.

Oghenekohwo, F., Kumar, R., Esser, E., and Herrmann, F. J. (2015). Using common information in compressive time-lapse full-waveform inversion. In 77th EAGE Conference and Exhibition 2015, volume 2015, pages 1–5. European Association of Geoscientists & Engineers.

Pan, W., Geng, Y., and Innanen, K. A. (2018). Interparameter trade-off quantification and reduction in isotropic-elastic full-waveform inversion: Synthetic experiments and Hussar land data set application. Geophysical Journal International, 213(2):1305–1333.

Pan, W., Innanen, K. A., Geng, Y., and Li, J. (2019). Interparameter trade-off quantification for isotropic-elastic full-waveform inversion with various model parameterizations. Geophysics, 84(2):R185–R206.

Pfrang, D., Schölderle, F., Bohnsack, D., Beichel, K., Dirner, S., and Zosseder, K. (2022). Geophysical Reservoir Characterization of the Upper Jurassic in the Bavarian Molasse Basin – from a Detailed Study to Field-Wide Conclusions. In Proceedings of the European Geothermal Congress (EGC), Berlin, Germany. European Geothermal Energy Council. 17–21 October 2022.

Pinsky, M. A. (2023). Introduction to Fourier analysis and wavelets, volume 102. American Mathematical Society.

Poletto, F., Farina, B., and Carcione, J. M. (2018). Sensitivity of seismic properties to temperature variations in a geothermal reservoir. Geothermics, 76:149–163.

Poulsen, S., Balling, N., and Nielsen, S. (2015). A parametric study of the thermal recharge of low enthalpy geothermal reservoirs. Geothermics, 53:464–478.

Qi, H., Ba, J., and Müller, T. M. (2021). Temperature effect on the velocity-porosity relationship in rocks. Journal of Geophysical Research: Solid Earth, 126(1):e2019JB019317.

Raknes, E. B. and Arntsen, B. (2015). A numerical study of 3D elastic time-lapse full-waveform inversion using multicomponent seismic data. Geophysics, 80(6):R303–R315.

References

Raknes, E. B., Weibull, W., and Arntsen, B. (2013). Time-lapse full waveform inversion: Synthetic and real data examples. In SEG International Exposition and Annual Meeting, pages SEG–2013. SEG.

Randolph, J. B. and Saar, M. O. (2011). Combining geothermal energy capture with geologic carbon dioxide sequestration. Geophysical Research Letters, 38(10).

Rawlinson, N. and Sambridge, M. (2005). The fast marching method: an effective tool for tomographic imaging and tracking multiple phases in complex layered media. Exploration Geophysics, 36(4):341–350.

Reiser, F., Schmelzbach, C., Maurer, H., Greenhalgh, S., and Hellwig, O. (2017). Optimizing the design of vertical seismic profiling (VSP) for imaging fracture zones over hardrock basement geothermal environments. Journal of Applied Geophysics, 139:25–35.

Routh, P., Palacharla, G., Chikichev, I., and Lazaratos, S. (2012). Full wavefield inversion of time-lapse data for improved imaging and reservoir characterization. In SEG International Exposition and Annual Meeting, pages SEG–2012. SEG.

Sanyal, S. K., Granados, E. E., and Menzies, A. J. (1995). Injection-related problems encountered in geothermal projects and their mitigation: the United States experience. In Proceedings World Geothermal Congress, pages 2019–2022.

Schmelzbach, C., Zelt, C., Juhlin, C., and Carbonell, R. (2008). P-and SV-velocity structure of the South Portuguese Zone fold-and-thrust belt, SW Iberia, from traveltime tomography. Geophysical Journal International, 175(2):689–712.

Schölderle, F., Pfrang, D., and Zosseder, K. (2023). Inverse flow zone characterization using distributed temperature sensing in a deep geothermal production well located in the Southern German Molasse Basin. Advances in Geosciences, 58:101–108.

Sethian, J. A. (1996). A fast marching level set method for monotonically advancing fronts. Proceedings of the National Academy of Sciences, 93(4):1591–1595.

Shuey, R. (1985). A simplification of the Zoeppritz equations. Geophysics, 50(4):609–614.

Sirgue, L. and Pratt, R. G. (2004). Efficient waveform inversion and imaging: A strategy for selecting temporal frequencies. Geophysics, 69(1):231–248.

Tarantola, A. (2005). Inverse problem theory and methods for model parameter estimation. SIAM.

Verschuur, D. and Berkhout, A. (2011). Seismic migration of blended shot records with surface-related multiple scattering. Geophysics, 76(1):A7–A13.

Virieux, J. and Operto, S. (2009). An overview of full-waveform inversion in exploration geophysics. Geophysics, 74(6):WCC1–WCC26.

Wang, Y. (1999). Approximations to the Zoeppritz equations and their use in AVO analysis. Geophysics, 64(6):1920–1927.

Wang, Z. and Nur, A. (1988). Effect of temperature on wave velocities in sands and sandstones with heavy hydrocarbons. SPE Reservoir Engineering, 3(01):158–164.

Yang, D., Meadows, M., Inderwiesen, P., Landa, J., Malcolm, A., and Fehler, M. (2015). Double-difference waveform inversion: Feasibility and robustness study with pressure data. Geophysics, 80(6):M129–M141.

Zhang, J., Verschuur, D., and Wapenaar, C. (2001). Depth migration of shot records in heterogeneous, transversely isotropic media using optimum explicit operators. Geophysical Prospecting, 49(3):287–299.

Zhang, R., Ma, D., Su, Q., and Huang, K. (2020). Effects of temperature and water on mechanical properties, energy dissipation, and microstructure of argillaceous sandstone under static and dynamic loads. Shock and Vibration, 2020(1):8827705.

Zhou, W., Brossier, R., Operto, S., and Virieux, J. (2015). Full waveform inversion of diving & reflected waves for velocity model building with impedance inversion based on scale separation. Geophysical Journal International, 202(3):1535–1554.

Zou, G., Zeng, H., Gong, F., Yin, C., Li, S., Peng, S., and Xu, Z. (2022). Effects of temperature and water saturation on the elastic moduli of sandstone and mudstone from the Lufeng geothermal field: experimental results and theoretical model. Geophysical Journal International, 230(2):1147–1165.

Chapter 5

FWI of DAS Versus Geophone Data for Vertical Seismic Profiling

Seismic characterization of geothermal reservoirs at high resolution helps to study the dynamics associated with heat production, necessary to mitigate premature thermal depletion and monitor possible induced seismicity. To this end, the full waveform inversion (FWI) of vertical seismic profiling (VSP) data offers a viable approach to achieve such a resolution. Emerging distributed acoustic sensing (DAS) technology enables VSP acquisition with significantly higher spatial sampling compared to conventional geophones. DAS VSP data were acquired using an optical fibre cable deployed inside a deep deviated well at a geothermal site in Munich, Germany. The recordings exhibit a low signal-to-noise ratio (SNR), which poses substantial challenges for FWI. Here, we evaluate the application of FWI with models that only show variations in the vertical direction, i.e., plane-layered media. FWI is applied to these DAS data using various inversion schemes, including one based on full records (with a length of 2 s) and another focused solely on (windowed) direct arrivals. The resulting P-wave velocity models are compared with those derived from a geophone-based VSP in a nearby well and co-located sonic logs. While the FWI of the full-record signal yields improved resolution over traveltime tomography, the most accurate results were obtained using windowed direct arrivals constrained by spatially adjacent channels. These findings highlight both the potential and limitations of in-casing-deployed DAS for high-resolution FWI and underscore the importance of developing new acquisition and processing strategies for geothermal reservoir characterization.

5.1 Introduction

High-resolution subsurface characterization is essential for various applications, particularly geothermal energy production (Lucia et al., 2003; Ma et al., 2021; Junker et al.,

2025). Sustainable development of geothermal resources requires a comprehensive knowledge of the reservoir, including the spatial distribution of thermal capacity, structural controls, and hydrogeological properties (Rybach, 2003; Grant and Bixley, 2011; Huenges and Ledru, 2011). In addition, evaluating the reservoir integrity is critical to mitigate operational risks such as induced seismicity (Simiyu, 2000; Webster et al., 2013). Seismic data provide essential information on subsurface structures, petrophysical properties, and fluid pathways (Molenaar et al., 2012; Staněk et al., 2022), making them instrumental in helping to optimize geothermal production with a reduced risk (Ali and Jakobsen, 2011; Lüschen et al., 2014; Bredesen et al., 2020; Yasin et al., 2023).

Seismic surveys may be conducted using surface, cross-well, or vertical seismic profiling (VSP) configurations (Verschuur and Neumann, 1999; Söding et al., 2024; Hardage, 1985). Although surface data cover large areas, their resolution decreases at large depths, especially in complex geological settings, due to the attenuation of high frequencies (Berkhout and Verschuur, 2008; Davydenko and Verschuur, 2017). Cross-well measurements capture high-frequency signals by placing sources and receivers inside the well, but their spatial coverage is limited to two-dimensional (2D) planes (Ernst et al., 2007; Raji et al., 2017), leaving substantial reservoir volumes unresolved (Daley et al., 2010). VSP methods offer a balance by combining surface sources with borehole receivers to achieve higher resolution at larger depths, while maintaining sufficient spatial coverage (Reiser et al., 2017, 2020; Kasahara et al., 2024). This makes VSP especially well suited for geothermal applications.

Full Waveform Inversion (FWI) of VSP data has emerged as a powerful tool for estimating high-resolution seismic velocity models (Virieux et al., 2017; Warner et al., 2013). Conventionally, VSP acquisition is based on geophones attached to wireline tools deployed at multiple depth intervals (Balch et al., 1982; Hardage, 1985). For each depth interval, a seismic source is activated several times at the surface (Yilmaz, 2001; Hartog et al., 2014). To cover an entire well, the source may have to be activated a few hundred times.

The recent advent of distributed acoustic sensing (DAS) with fibre-optic cables has opened up new possibilities for seismic data acquisition in deep and/or slanted wells (Parker et al., 2014; Fernández-Ruiz et al., 2020; Jousset et al., 2022; Mateeva et al., 2014; Willis et al., 2016a; Mad Zahir et al., 2023). Using coherent backscattered signals, DAS records the strain rates along overlapping fibre segments, functioning as an array of virtual sensors activated concurrently (Lindsey et al., 2020; Paitz et al., 2021). Thus, it offers several benefits over conventional velocity sensors, including single-pass deployment (Fang et al., 2012; Zhan, 2020; Udd and Spillman Jr, 2024; Barrias et al., 2016) and dense spatial data sampling along the wellbore (Mateeva et al., 2014; Willis et al., 2016a; Mad Zahir et al., 2023).

Despite these advantages, the quality of DAS data is highly dependent on the cable

installation method. There are two main ways of deployment: (1) cementing the fibre behind the casing (Al Shoaibi et al., 2022), which ensures good coupling and a high signal-to-noise ratio (SNR) suitable for FWI (Willis et al., 2016b; Qu et al., 2024); and (2) deploying the cable inside the casing (Martuganova et al., 2022; Schölderle et al., 2021), which is more common in deviated or existing wells, but this often results in variable coupling and poor data quality (Lipus et al., 2021; Henninges et al., 2021; Ge et al., 2025). Martuganova et al. (2021) showed that DAS data, recorded inside the well at a geothermal site, had mild resonances, which could be removed by filtering.

This study focuses on DAS VSP data acquired with a fibre-optic cable installed inside a 3000 m deep deviated well in an urban geothermal site in Munich, Germany. The cable was deployed using sucker rods, which introduces uncertainty due to rod buckling and imprecise channel positioning. In addition, poor coupling led to strong noise contamination, e.g. resonances and tube waves, especially after the first arrivals. These issues pose significant challenges for a successful application of FWI.

In this chapter, we present a plane-layered-model FWI scheme tailored with respect to the features of this DAS dataset. The inversion employs Gauss–Newton optimization and computes synthetic strain rates to match the DAS measurements. First, we evaluate the performance of FWI using a full 2-seconds record length to recover a P-wave velocity (V_P) model to fit layer reflections. We then investigate the advantages of isolating direct arrivals and incorporating information from densely sampled adjacent channels. The resulting models are validated against sonic logs and velocity estimates from a conventional geophone-based VSP acquired in a nearby well.

5.2 Munich data setup

5.2.1 Munich geothermal site

The study area is an urban geothermal site in Munich, located within the North Alpine Foreland Basin (Pfiffner, 1986; Barnolas et al., 2019). This basin contains sedimentary deposits from the Quaternary and Tertiary periods (Kuhlemann and Kempf, 2002). The combined effects of sedimentation, tectonic deformation, and glacial activity have produced a complex structural setting with faulting and folding (Crampton and Allen, 1995; Schlunegger and Kissling, 2024). A moderate geothermal gradient of approximately 30 °C/km yields subsurface temperatures around 100 °C at a depth of 2.5 km (Przybycin et al., 2017), forming favorable conditions for geothermal heat extraction (Moeck et al., 2019). Although the region is seismically active due to the ongoing stress transfer between the Alps and the foreland basin, seismicity remains low in magnitude (Kastrup et al., 2004, 2007).

5.2.2 Munich VSP survey

A VSP survey was conducted at the Munich geothermal site in April 2020. Four Sercel's Slimwave® geophones were deployed using a wireline system in the production well Th1 (see Fig. 5.1), which allowed covering depth intervals of 60.8 m with 15.2 m receiver spacing. These geophones can only be lowered when the deviation is less than 60 °. Thus, the maximum depth at which they were deployed in Th1 was 2584 m. Furthermore, they could not record subsurface signals at depths above 800 m because the well diameter of 0.508 m is larger than the maximum threshold for the geophones to ensure a good coupling, which is 0.330 m for this system.

In parallel, a fibre-optic cable attached to sucker rods has already been pushed into the production well Th4 (see Fig. 5.1). It must be assumed that there was variable buckling of the rods, leading to uncertainty about the exact geometry of the cable inside the casing. However, this cable had a length of 3744 m, which should allow recording along the entire Th4 well. This installation setup relied on gravitational force for coupling with the borehole wall. Given the Th4 well design (diameter and deviation), the cable had sufficient coupling at depths below 800 m.

A seismic vibrator was placed 185.79 m away from the Th1 well head at an azimuth of 24.4 °, as shown in Fig. 5.1. It injected sweeps into the ground with frequencies ranging from 12 to 110 Hz. For each geophones' level, the sweeps were repeated five times to increase the SNR. Consequently, the DAS data were measured for 235 shots with a gauge length of 10 m and a channel spacing of 1 m as illustrated in Fig. 5.2. The spatial coordinates of each channel are assigned to the midpoint of the corresponding gauge length. To correct for depth inconsistencies, the surveyors had to reconcile the measured depth with optical distance— shorter by 45 m —likely due to an incorrect setting of the refractive index in the iDAS system (Parker et al., 2014).
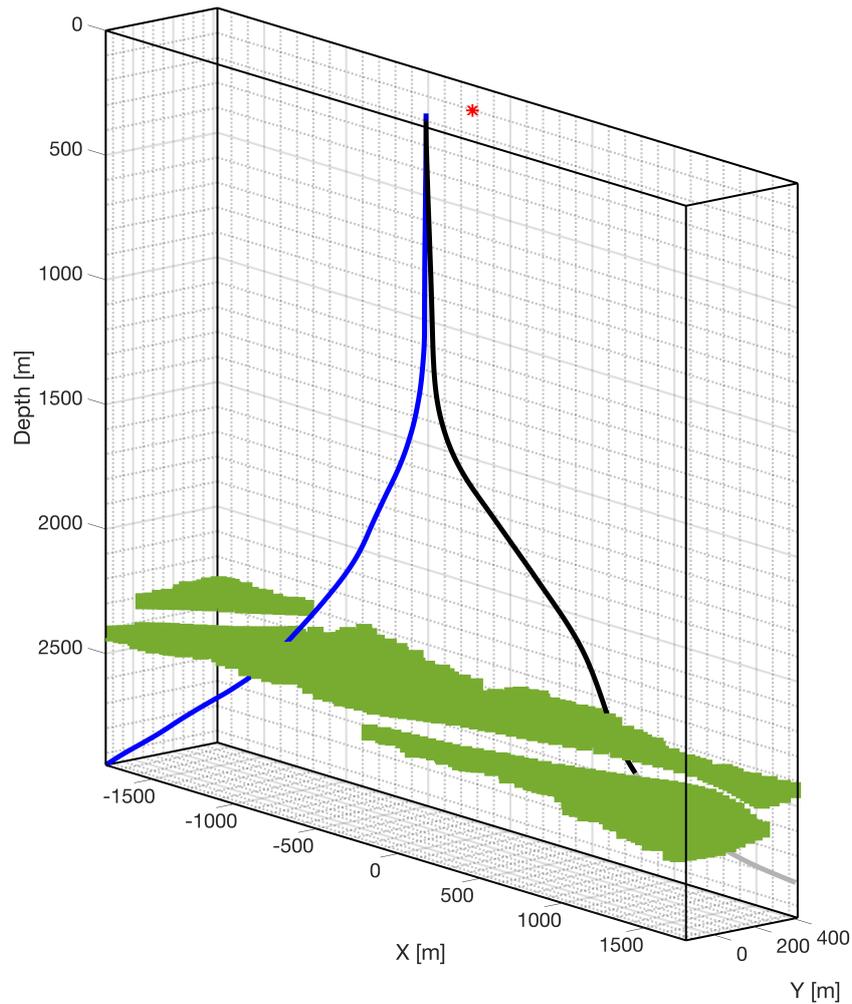
Figure 5.1: Setup of Munich geothermal site VSP survey. The red star indicates the vibrator location at the surface. The black line represents Th1 borehole geometry with deployed geophones while the bottom gray line does not have geophones due to too-high deviation. The blue line represents Th4 with DAS cable. The green planes draw the top of the reservoir.
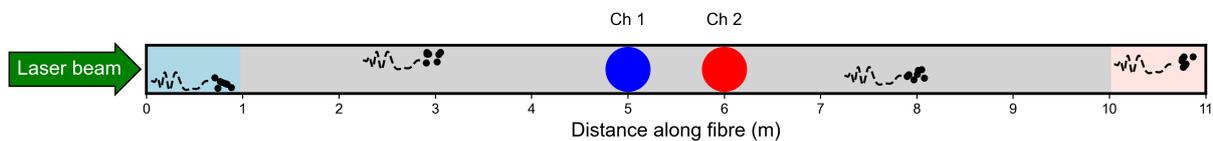

Figure 5.2: A conceptual model of a fibre-optic cable recording DAS data. A laser pulse is emitted into the cable. Impurities (black dots) back scatter the light which is reshaped by a propagating ground displacement as indicated by (black dashed line). The optical signal over the first 10 m distance (light blue and gray area) is summed to give the signal in the middle point (Ch1—blue dot). The signal at Ch2 (red dot) is the sum of the scattered signal over 10 m shifted by 1 m (light red and gray area).

The correlated and stacked DAS data, averaged over 160 shots, are shown in Fig. 5.3. Unlike the geophone data in Fig. 4.5, the DAS signal was recorded throughout the reser-

voir section. However, coherent seismic events are not observed across the full depth profile: the direct P-wave arrival is not discernible from the surface down to a depth of approximately 150 m. After that, it is discontinuous (i.e., a stepwise function) down to a depth of around 800 m, which is physically unrealistic. This renders the direct arrival unreliable in the previously mentioned sections. Other downgoing P-waves, such as multiples, appear incoherent and irregular, probably because of the interference of upgoing P-waves. As illustrated in Fig. 5.3, S-waves are absent and the overall SNR is low. The noise, including strong tube waves and background instrumental and coupling-related distortions, originate from many sources.
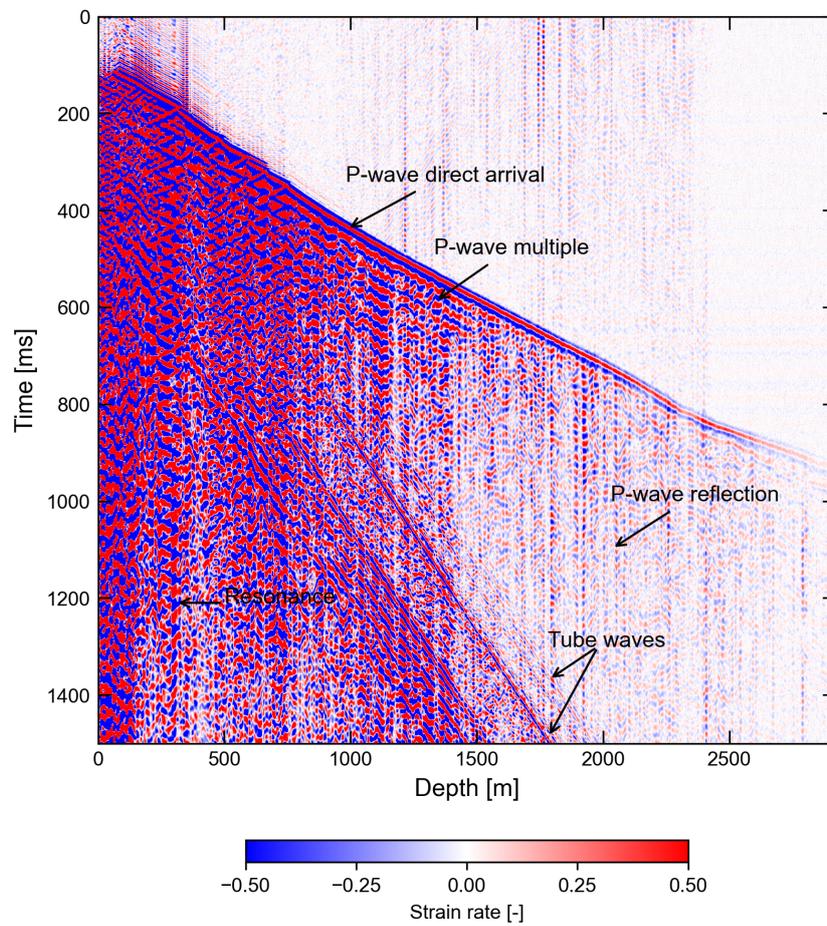
Figure 5.3: Raw measurements of strain rates recorded at Th4 at the Munich geothermal site. The limits of the colorbar are lower than the largest amplitude values to increase the visibility of weak events. In the first 100 m, the DAS cable did not pick up the direct arrival. Until a depth of 800 m, the direct arrival as well as later events are distorted, reducing their usefulness for further (pre-)processing and inversion. At later times than the direct arrival, reverberations like multiples and resonances appear. Strong tube waves of a slope corresponding to a velocity of 1.5 km/s are clearly visible.

5.3 FWI Approach

5.3.1 Time domain waveform modelling

A fibre-optic senses dynamic strain; see, for example, Al Hasani and Drijkoningen (2023), which is a projection of the 3D strain tensor on the cable axis, as shown in Fig. 5.4.
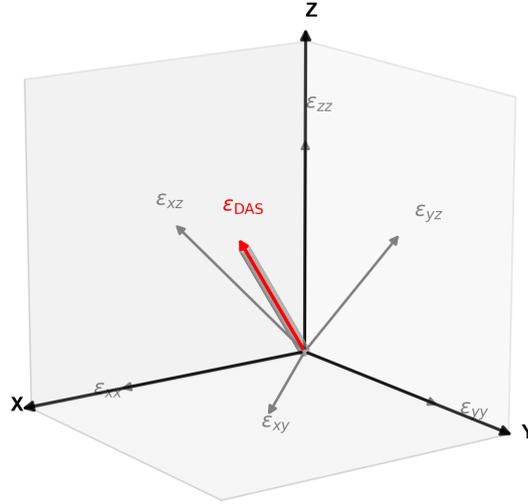
Figure 5.4: Representation of the six independent components of the strain tensor (gray axes) in 3D Cartesian space (black axes). The directional sensing of the cable is given by the red arrow, with the gray cylinder indicating the cable itself.

For a unit vector, $\boldsymbol{n} = [n_x, n_y, n_z]^T$, the strain measured along the fibre, $\varepsilon_{\mathrm{DAS}} = \boldsymbol{n}^T \boldsymbol{\varepsilon}_{\mathrm{Cart}} \boldsymbol{n}$, expands to

$$\varepsilon_{\mathrm{DAS}} = n_x^2 \varepsilon_{xx} + n_y^2 \varepsilon_{yy} + n_z^2 \varepsilon_{zz} + 2n_x n_y \varepsilon_{xy} + 2n_x n_z \varepsilon_{xz} + 2n_y n_z \varepsilon_{yz}, \qquad (5.1)$$

where ε_{xx}, ε_{yy}, ε_{zz}, ε_{xy}, ε_{xz} and ε_{yz} are the six independent components of the symmetric strain tensor in Cartesian coordinates, $\varepsilon_{\mathrm{Cart}}$:

$$\boldsymbol{\varepsilon}_{\mathrm{Cart}} = \begin{bmatrix} \varepsilon_{xx} & \varepsilon_{xy} & \varepsilon_{xz} \\ \varepsilon_{xy} & \varepsilon_{yy} & \varepsilon_{yz} \\ \varepsilon_{xz} & \varepsilon_{yz} & \varepsilon_{zz} \end{bmatrix}.$$

In CPS, the strain tensor is given in cylindrical coordinates. To transform this tensor from a cylindrical (r, ϕ, z) to a Cartesian (x, y, z) system, we apply

$$\boldsymbol{\varepsilon}_{\mathrm{Cart}} = \mathbf{T}\, \boldsymbol{\varepsilon}_{\mathrm{cyl}}\, \mathbf{T}^T, \qquad (5.2)$$

where $\mathbf{T}$ is the rotation matrix:

$$\mathbf{T} = \begin{bmatrix} \cos\theta & \sin\theta & 0 \\ -\sin\theta & \cos\theta & 0 \\ 0 & 0 & 1 \end{bmatrix} \tag{5.3}$$

with θ being the angle $\theta = \tan^{-1}(y/x)$.

The components of $\boldsymbol{\varepsilon}_{\mathrm{cyl}}$ are related to displacements in cylindrical coordinates, u_r, u_ϕ, and u_z, as described in Sollberger et al. (2020):

$$\varepsilon_{rr} = \frac{\partial u_r}{\partial r}$$
$$\varepsilon_{r\phi} = \frac{1}{2}\left(\frac{1}{r}\frac{\partial u_r}{\partial \phi} + \frac{\partial u_\phi}{\partial r} - \frac{u_\phi}{r}\right)$$
$$\varepsilon_{\phi\phi} = \frac{1}{r}\left(\frac{\partial u_\phi}{\partial \phi} + u_r\right)$$
$$\varepsilon_{rz} = \frac{1}{2}\left(\frac{\partial u_z}{\partial r} + \frac{\partial u_r}{\partial z}\right)$$
$$\varepsilon_{\phi z} = \frac{1}{2}\left(\frac{\partial u_\phi}{\partial z} + \frac{1}{r}\frac{\partial u_z}{\partial \phi}\right)$$
$$\varepsilon_{zz} = \frac{\partial u_z}{\partial z}.$$

In the reflectivity or Haskell-matrix method (Meehan, 2018), the six components of the strain tensor can be calculated in the horizontal-wavenumber domain (assuming plane-layered media), and integrated over the horizontal wavenumbers to get to the spatial-domain responses, and then inverse-FFT'ed over the frequencies to obtain the time-domain responses. We use the wave-number integration technique as coded by Herrmann (2013) to determine the strain tensor $\boldsymbol{\varepsilon}_{\mathrm{Cart}}$ due to a vertical point force. This code does not allow to define a gauge length for the calculation of the strain. Therefore, we assume that the strain recorded with a gauge length of 10 m is sufficiently accurate modelled as a point strain. After that, we determine the strain $\varepsilon_{\mathrm{DAS}}$ at a point along the fiber direction using Eq. 5.1. Finally, the strain $\varepsilon_{\mathrm{DAS}}$ is numerically differentiated to obtain the strain rate, which is the quantity delivered by the iDAS system.

5.3.2 Time-domain waveform inversion

FWI of observed data, d_{obs}, is an ill-posed inverse problem mainly because d_{obs} is noisy and/or have uncertainties. The solution to such an inverse problem — model that reproduces the data — is non-unique. Therefore, we want to find a simple model (m) that

minimizes the data residual (δd),

$$\delta d = d_{obs} - d_{calc}, \tag{5.4}$$

where d_{calc} is the calculated data. The residuals and the optimization can be evaluated in the time domain or in the frequency domain. We choose the time domain because it allows: (1) a cost-effective inversion by fitting a broad range of frequencies at once. The fit between d_{obs} and d_{calc} is quantified by the relative data error (ϵ_d),

$$\epsilon_d = \frac{||\delta d||}{||d_{obs}||}, \tag{5.5}$$

where $||\cdots||$ refers to the Euclidean norm. To solve the FWI inverse problem, we use the Levenberg-Marquardt (LM) algorithm with a smoothing term as follows:

$$m^{(i+1)} = m^i + \left[\left(\mathbf{J}^{(i)} \right)^T \mathbf{J} + \left(\alpha \mathbf{S}^{(i)} \right)^2 + \beta^2 \mathbf{L}^T \mathbf{L} \right]^{-1} \mathbf{J}^{(i)} \delta d^{(i)}, \tag{5.6}$$

where i is the iteration number, $\mathbf{J}$ is the Jacobian matrix of dimensions $N \times M$ with N being the number of data points in a seismic trace and M being the number of layers, the superscript T refers to matrix transpose, $\mathbf{S}$ is a diagonal scaling matrix of the damping parameter α, $\mathbf{L}$ is the Laplacian smoothing operator, and β is a scalar value (smoothing parameter). The casling matrix $\mathbf{S}$ contains the weights of α for each parameter of m using sensitivities by

$$\mathbf{S} = diag \left(\frac{max \left(\sum_p J_{pq}^2 \right)}{\sum_p J_{pq}^2 + \delta} \right), \tag{5.7}$$

with $p = 1, 2, \cdots, N$, $q = 1, 2, \cdots, M$, and δ is a very small value added to the dominator to avoid dividing by zero. To calculate the sensitivities in the Jacobian matrix $\mathbf{J}$, we use the perturbation approach. In this approach, each model parameter m_q is perturbed by a small amount $\Delta m_q^{(i)}$, 10^{-4} is used here, then data ($d_{\Delta m_q}^{(i)}$) are generated. The sensitivity is calculated by

$$J_q^{(i)} = \frac{d_{calc}^{(i)} - d_{\Delta m_q}^{(i)}}{\Delta m_q^{(i)}}. \tag{5.8}$$

The performance of the LM scheme in FWI is sensitive to the initial model, especially for V_P. An initial model close to the true model ensures convergence to the global minima with a reasonable computational time per number of iterations. A good initial model can be estimated from traveltime tomography, which fits calculated arrival times to picked arrival times. For that purpose, we have developed a suitable algorithm. The arrival times and the ray traces in 3D space necessary to define the calculated data and the sensitivities are calculated based on solving the eikonal equation using the fast-marching method

(Sethian, 1996; Rawlinson and Sambridge, 2005). We adopted the implementation of the fast-marching method from Chen et al. (2023), and constrain the traveltime inversion to give a 1D velocity model. We use Eq. 5.6 for the traveltime inversion to find an initial model which minimizes the misfit, Eq. 5.9, between calculated and picked $V_{\rm P}$ arrivals.
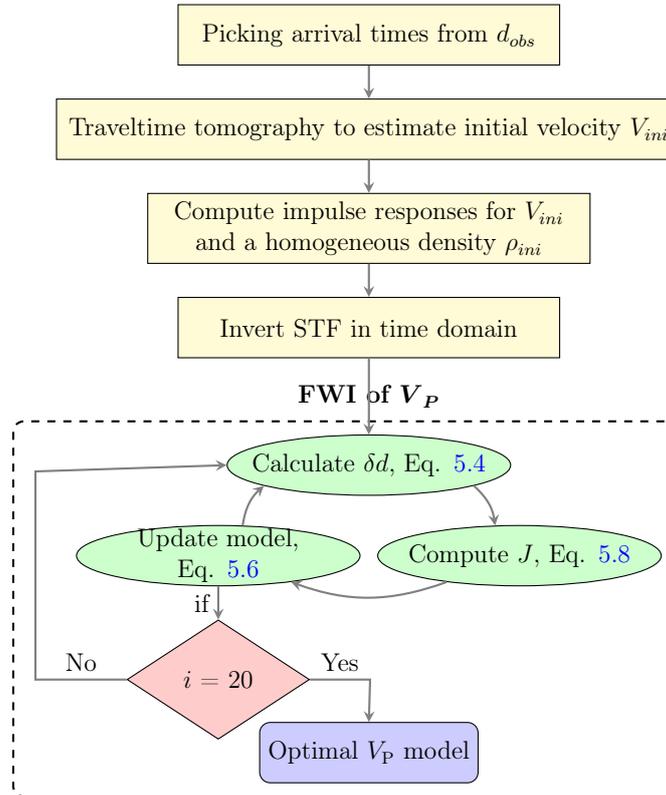

Figure 5.5: Flowchart of the FWI approach for the DAS data. STF = Source Time Function. The number of iterations is arbitrarily set at 20.

5.4 Data preprocessing

The raw data in Fig. 5.3 contain unwanted events, such as tube waves. In the context of FWI, matching these undesired events is neither necessary—since they do not contribute to constructing the $V_{\rm P}$ model—nor feasible, as their accurate modelling is not supported in the current framework. Therefore, we chose to pre-process them before applying FWI. The strain-rate measurements of Fig. 5.3 exhibit strong tube waves between depths of 800 and 2920 m. We followed the same approach for removing the tube waves as in Section 4.4. As shown in Fig. 5.6, in addition to the removal of tube waves, the nearly horizontal events caused by vibrations of the recording instrument were also filtered out in

the frequency—vertical-wavenumber (f, k_z) domain. We also muted all the signals before the first arriving P-waves. Other seismic events, e.g. the down- and up-going waves after the direct arrival, have now become (more) coherent. These events are attributed to a combination of the acquisition setup, the axial sensitivity of the fiber-optic, and the paths of wave propagation. However, the mechanism of their generation is unknown. In the VSP gather in Fig. 5.6, the tube waves have been removed, and the down- and up-going waves are now more coherent. Unexpectedly, events between 1000 and 1500 m arriving after 1000 ms have an increased amplitude. Comparison of the DAS data in Fig. 5.6 with the geophone data in Fig. 4.6 indicates the absence of coherent P-wave reflections from the reservoir, as well as a lower quality of coupling indicated by inconsistency of amplitudes in the former data set.
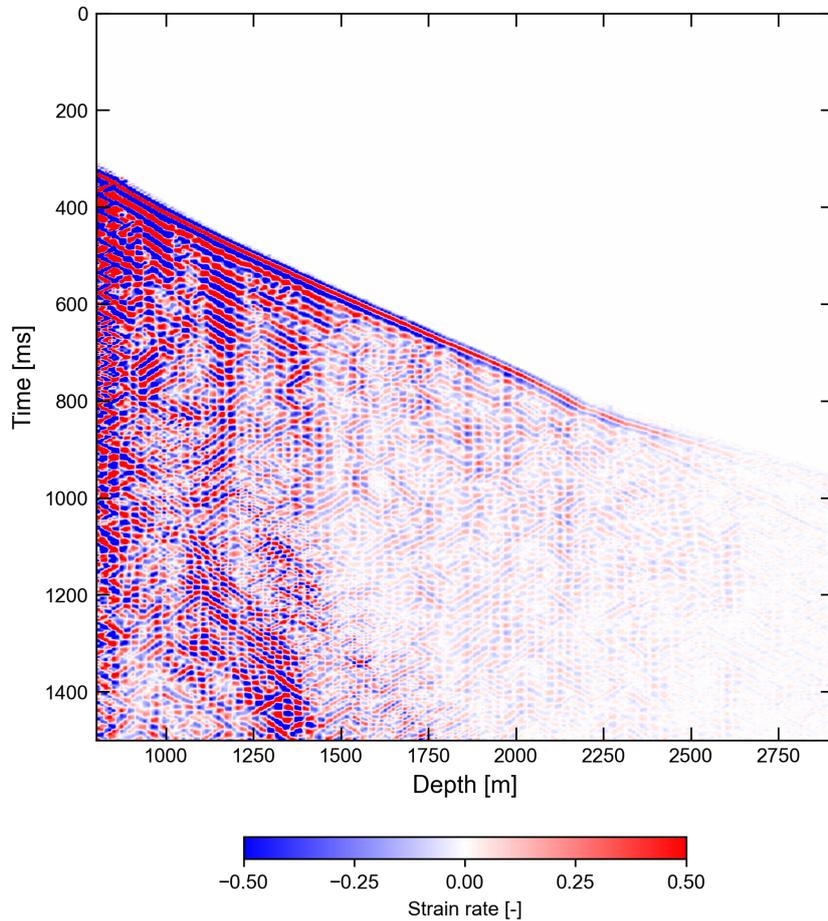
Figure 5.6: Strain-rate measurements in well Th4 at the Munich geothermal site between a depth of 800 and 2920 m, after removal of unwanted seismic events and muting noise before the direct arrival.

5.5 Results

5.5.1 FWI of DAS Vs. Geophones

For the inversion of the pre-processed DAS data of the Munich geothermal site, we discretized the model with 146 layers of 20 m thickness. We updated V_{P} only in the depth range 800 to 2920 m. According to Eq. 5.8, calculating the sensitivity matrix requires 106 separate waveform modellings for every iteration in the inversion. The computational time of each modelling thus increases proportionally with the number of receivers. Including all channels in the DAS data, around 2120, will make the computational time of FWI prohibitive. Since the 1 m channel spacing and the 10 m gauge length mean that neighboring measurements are more or less physically dependent, we choose channels such that the gauge lengths are not overlapping. So we spatially downsampled the data and keep a strain-rate trace per 15 m, which is the same receiver sampling as for the geophone VSP data. Hence, the number of traces per layer would be equal. The DAS data have also been filtered to have the same frequency band, 10 to 35 Hz, as used in the FWI of the geophone data, see Section 4.5.2. Thus, a comparison between the models estimated from particle velocity versus strain rate measurements is judged to be acceptable.

FWI of full records (with a length of 2 s)

Via traveltime tomography, an initial V_{P} model is obtained, as shown in Fig. 5.11. Then, the impulse response of the strain along the DAS cable is calculated according to Section 5.3.1, where ρ is assumed to be homogeneous, at a value of of 2400 kg/m^3. To model waveforms, it is necessary to convolve the impulse responses with a source-time function (STF). The STF is inverted from a 0.1 s time window around the direct arrival by deploying all the 190 strain-rate traces resulting from spatial downsampling. Fig. 5.7 shows a comparison of the inverted STF from the geophones and the DAS data and their amplitude spectra. These wavelets are almost centered around zero lag and have similar onset—time window -0.075 to -0.020 s. The geophone-drived STF shows relatively broader lobes and reduced peak amplitude, indicating low-frequency content compared to the other STF. This can be attributed to the high SNR of the geophone data where high frequencies are attenuated as they travel through the subsurface. On the other hand, the naturally attenuated high frequencies in the DAS data with low SNR gets revived because of noise. This is also confirmed by analyzing the amplitude spectra, with the wavelet inverted from the fibre-optic data also has relatively high amplitudes of frequencies in the range of 0 – 10 Hz, which are not generated by the vibrator. The geophone data gives a wavelet with a higher fidelity, where the amplitudes of the previously mentioned frequency range have very low amplitudes.
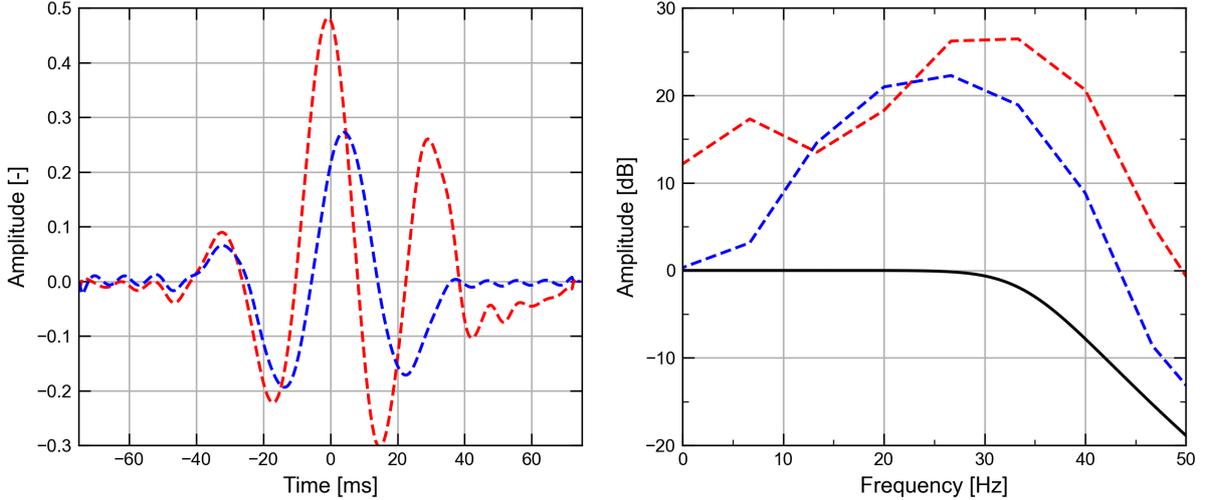
Figure 5.7: A comparison of inverted STFs (left plot) from the geophone data (blue line) and the DAS data (red line) as well as their amplitude spectra (right plot), where the same color coding applies. The amplitude response of the low pass filter used to filter the data is also displayed (black line).

From Fig. 5.6 it can be determined that the deepest traces have around two orders of magnitude lower amplitudes compared to the shallowest traces. Thus, the sensitivity of the inversion, whether it is STF or FWI, would be greater for the shallowest traces. To compensate for this, we normalized every trace by the maximum of the envelope of the direct arrival for both the observed and the calculated data. Thus, the effects of attenuation (Q_{P}) are not included in the modelling. Fig. 5.8 shows the normalized field and initial data, which are calculated from the V_{P} obtained from the traveltime tomography.

We have chosen α and β values of $1 \cdot 10^3$ and $5 \cdot 10^3$, respectively, based on FWI trials with the shallowest 20 channels from 800 to 1120 m. β is larger than the α to reduce oscillations in inverted models due to imprecise channels coordinates, as mentioned in Sec. 5.2.2. After 20 iterations with 190 channels from 800 to 2920 m, FWI results in strain-rate data shown in the middle panel of Fig. 5.9, which have reflections similar to the particle velocity data in Fig. 4.16. None of these reflections are fitted to the reflections in the observed DAS data. On the other hand, the direct arrivals show an improved fit, where the difference became less coherent, see right of Fig. 5.9.

Fig.5.10 shows the relative data error and shows an overall reduction of 3 %, approximately two-thirds of it in the first three iterations. The relative data error of later iterations has a lower rate of change with a continued decrease. Thus, more iterations are likely to lead to updates in the model. Fig. 5.11 shows that the V_{P} model inverted with FWI of the DAS data has a higher resolution than that estimated with traveltime tomography (initial model). The former V_{P} model agrees fairly well with the model inverted from the

conventional geophone VSP data, especially in the depth range 800 to 1900 m. At a depth of 1950 m, there is a rise in the velocity recovered by the DAS data that is in agreement with the sonic log, averaged over 10 m. FWI of these DAS data with a record length of 2 s does not resolve the upper boundary of the reservoir well, where small updates from the initial model are noticeable. Within the reservoir, the updates were large, reaching 750 m/s, resulting in a structure similar to that of the sonic log or the geophones.

By comparing the observed and inverted data in Fig. 5.9, it becomes clear that the main event contributing to correct model updates is the direct transmitted wave. Other inverted events, reflections and multiples, do not fit well to other transmitted and reflected waves in the observed data. Thus, we consider the direct arrival the only useful event in the observed DAS data. Consequently, we focus on the feasibility of FWI with only the direct arrivals in the DAS data.
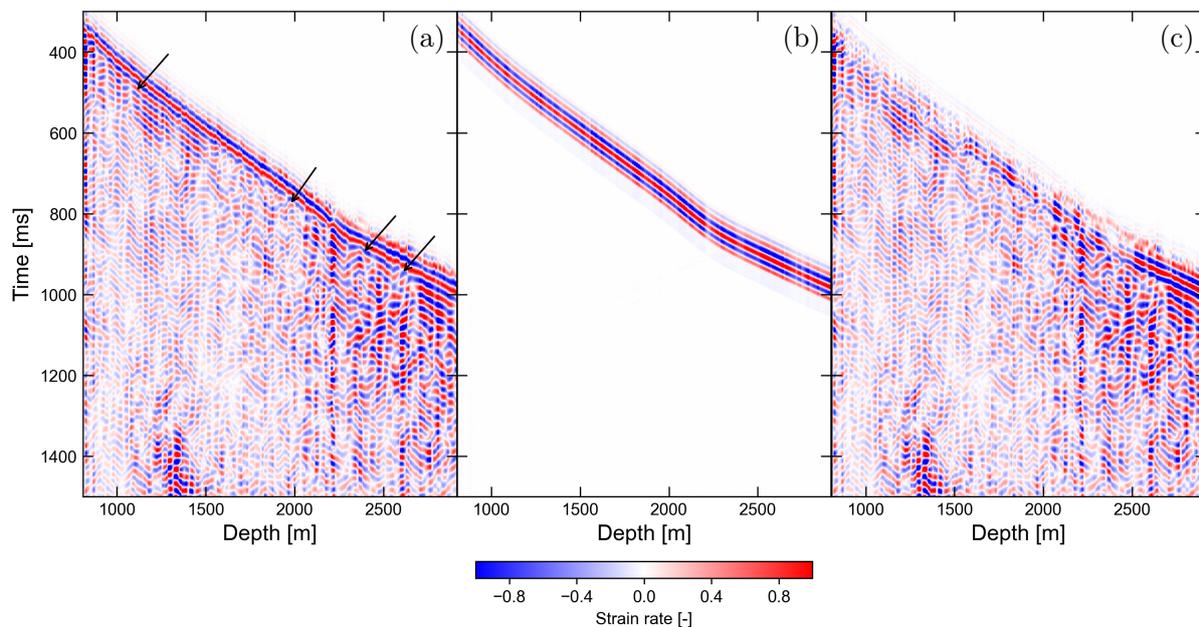
Figure 5.8: Trace-normalized observed pre-processed DAS data (a), trace-normalized initial synthetic data (b) and their difference (c). In the observed data, there are weak reflections, some of them are pointed out by black arrows. The initial data only show the direct arrivals. The difference in the first break between the observed and the initial data has systematic errors, indicating the ability to achieve better fits.
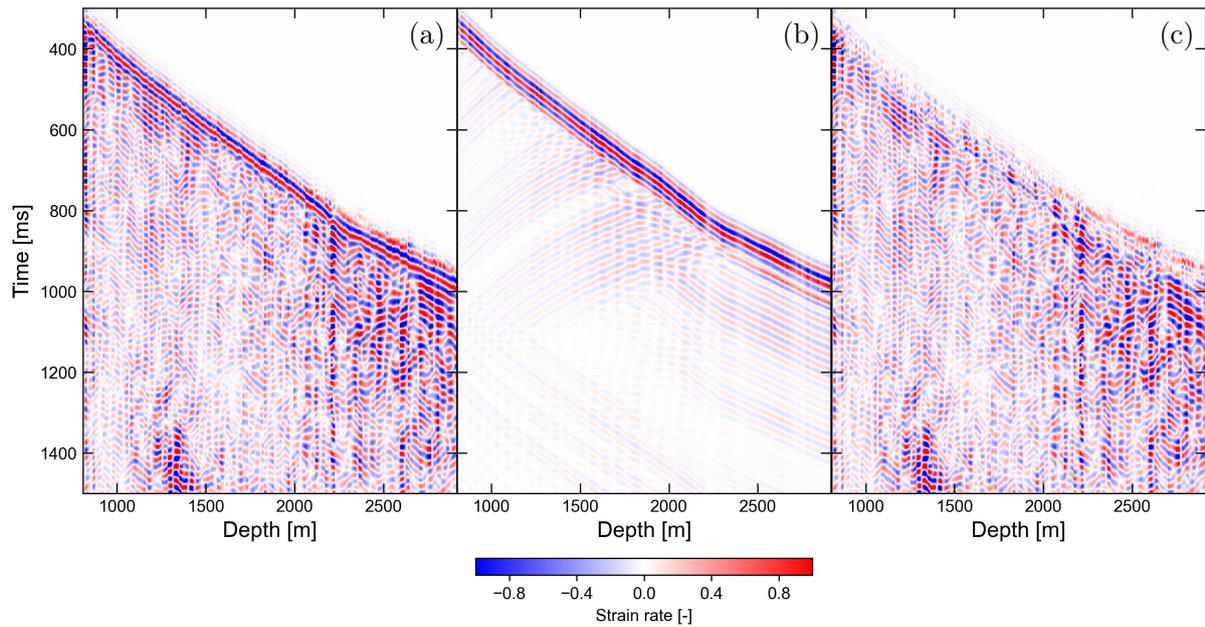
Figure 5.9: Observed DAS data after applying a band-pass filter from 10 to 35 Hz (a), synthetic data with model from inversion (b) and their difference (c). The difference in the first break between the observed and the synthetic data with the optimal velocity model has less systematic errors, indicating more fit. The reflections in the synthetic data with the optimal velocity model are not matching the reflections in the observed data, where the difference stays the same.
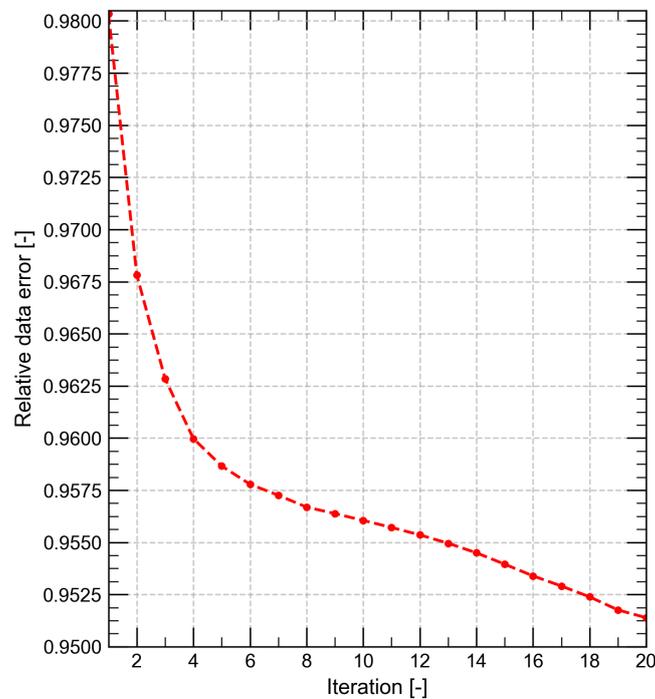
Figure 5.10: Relative data error of 20 FWI iterations. In the first three iterations, the misfit is reduced considerably compared to later iterations, where the rate of change of the misfit slows down.
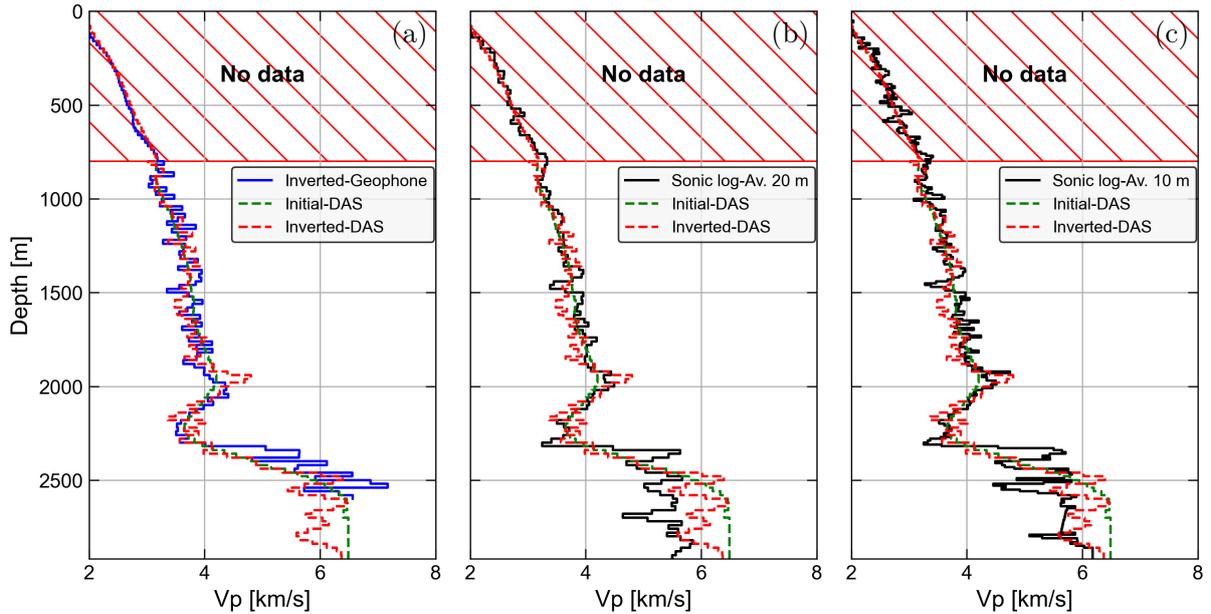
Figure 5.11: Comparison between the inverted V_P model from 2-s DAS data with the inverted V_P from the geophone data (a), the sonic-log data in Th4 averaged over 20 m (b) and averaged over 10 m (c). The inverted models in the first 800 m are not updated due to the lack of reliable data.

FWI focused on (windowed) direct transmitted arrival

First, we extract the direct arrival in the $t-z$ domain, as shown in Fig. 5.12. Consequently, the SNR of the observed data is increased, allowing a reduction in regularization by an order of magnitude. In this case, α and β could be set to $1 \cdot 10^2$ and $5 \cdot 10^2$, respectively. The FWI of the direct arrival starts with the same initial models as in Section 5.5.1.

In Fig. 5.13 the results after 20 iterations are shown: the synthetic direct arrivals after FWI have a better fit than the initial synthetic data to that of the observed data, which is indicated by the difference. Furthermore, this difference in Fig. 5.13 has even lower coherency than the difference determined using a long record length, Fig. 5.9. The minimization of the difference is the largest in the reservoir area. The relative data error in Fig. 5.14 is reduced from approximately 0.60 to 0.36, a relative reduction of some 40 %, which confirms the minimization of the data misfit. Moreover, it shows a stable convergence with values from the 4th to the 20th iteration plateau. The inverted model with the windowed direct arrival matches better with the sonic log and the geophone inverted models compared to that with full-record data (of 2 s duration). In addition, the sharp transition above the geothermal reservoir is now retrieved. However, the velocity structure within the reservoir is not well resolved, which can be attributed to the absence of high frequencies; in this region, the maximum frequency recorded is 25 Hz.

It could be shown that FWI of these DAS data is more reliable, when only the direct

arrivals are considered. However, this approach lacks resolution below the high-contrast boundary and within the geothermal reservoir. To improve the resolution of the FWI with the direct arrival, we next leverage the dense sampling achieved by the DAS data.
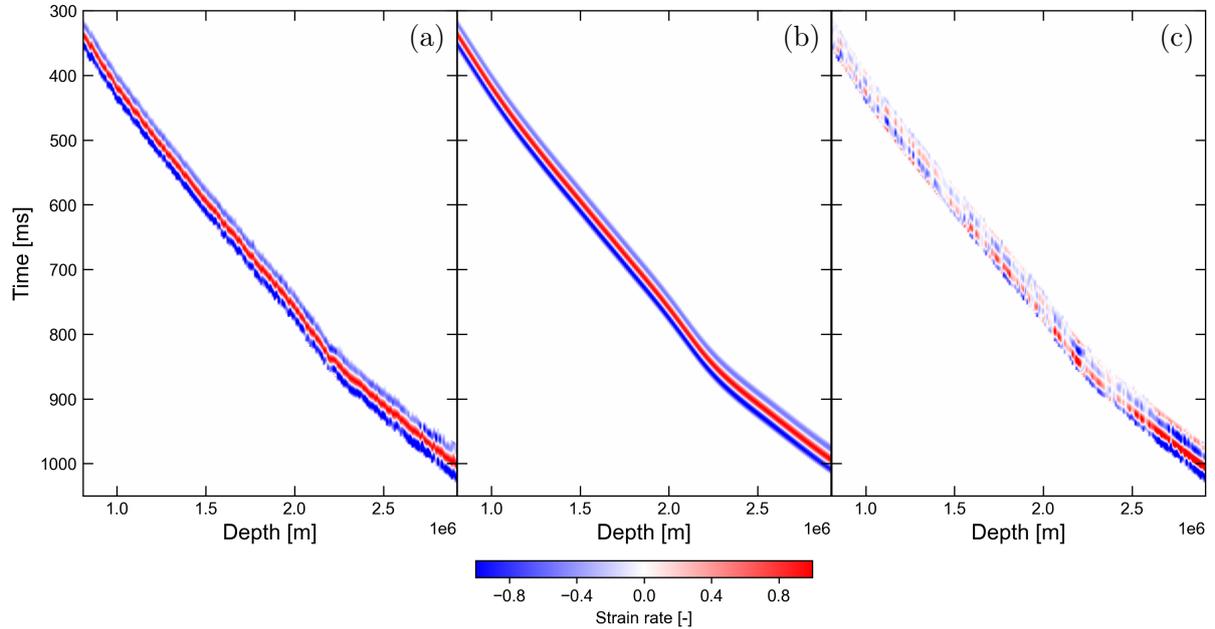

Figure 5.12: Trace-normalized windowed direct arrival of the observed DAS data (a), trace-normalized direct arrival of the initial synthetic data with velocity estimated by traveltime tomography (b) and their difference (c).
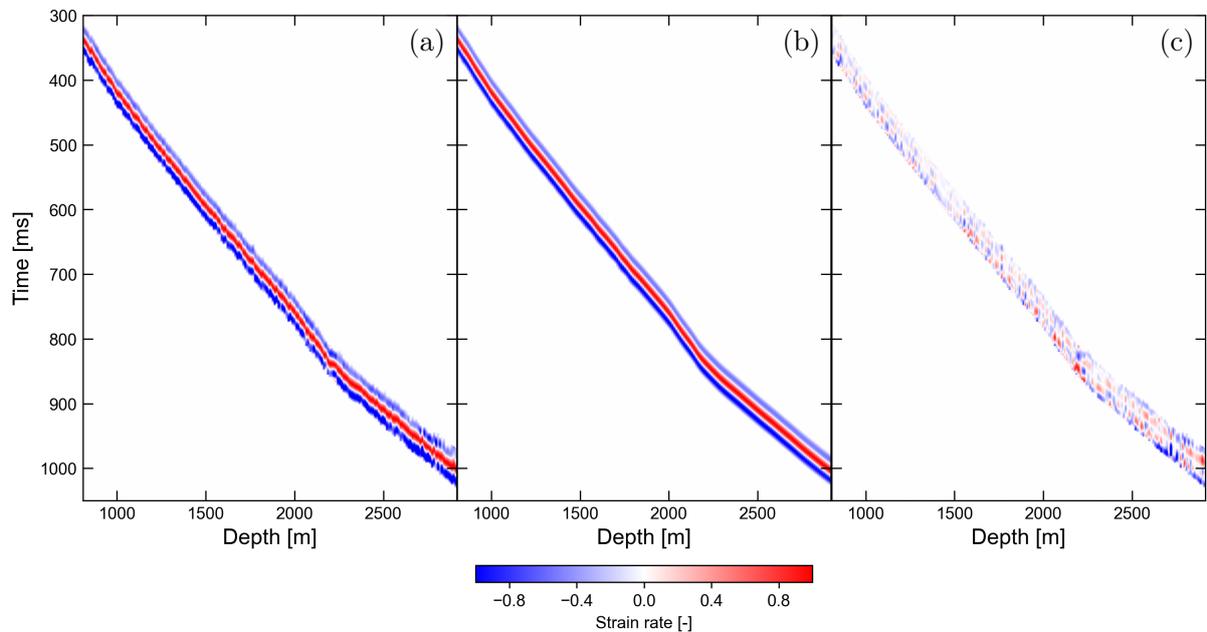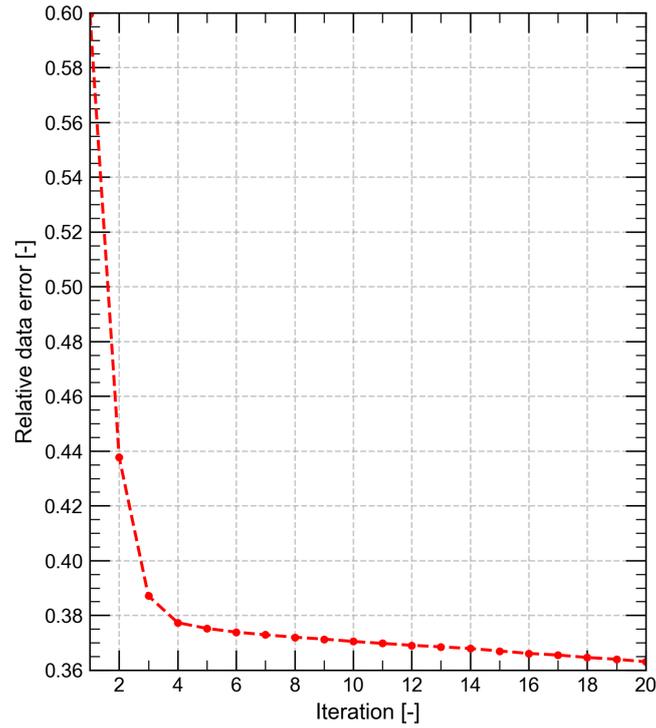

Figure 5.13: Trace-normalized windowed direct arrival of observed DAS data (a), direct arrival after FWI with 20 iterations (b) and their difference (c). The difference in the first break between the observed and the data after inversion shows little coherence, indicating a better fit.

Figure 5.14: Relative data error of 20 FWI iterations. In the first three iterations, the misfit is reduced considerably compared to later iterations, where the rate of change of the misfit slows down.
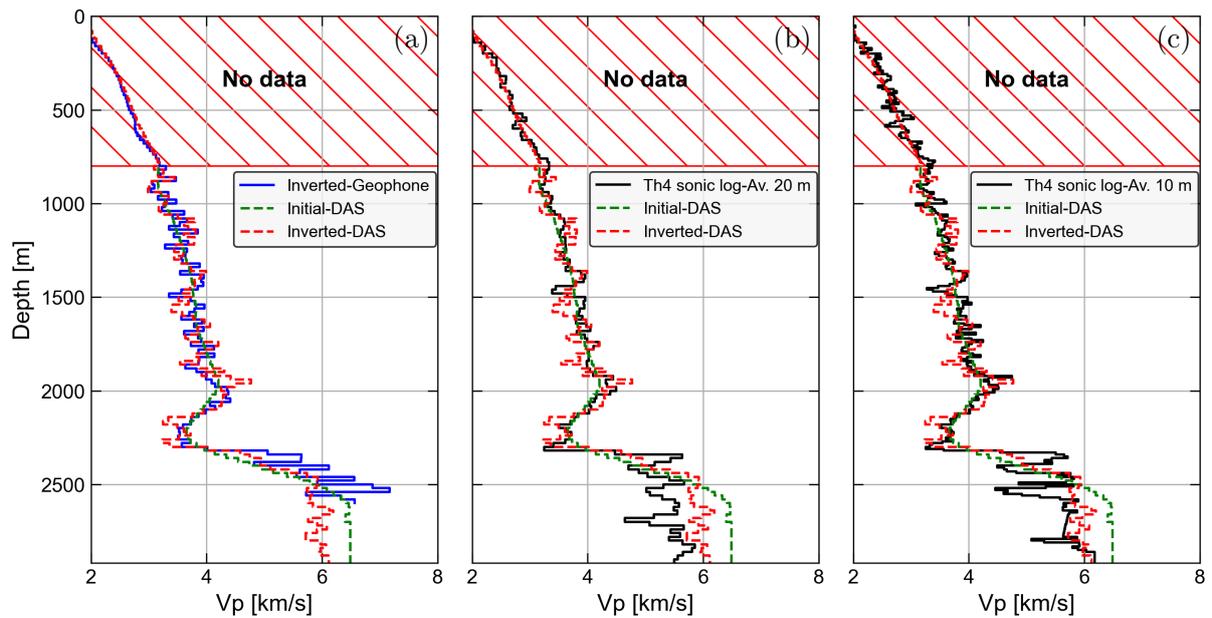
Figure 5.15: Comparison of the inverted V_P model from the windowed direct arrival of DAS data sampled every 15 m with the inverted model from the geophone data (a), the sonic-log data in Th4 averaged over 20 m (b) and averaged over 10 m (c).

5.5.2 FWI of DAS with denser data sampling

Previously, we chose to down-sample the DAS data to the sampling of the geophone data, i.e., 15 m. Thus, we discarded $14/15^{th}$, which may be able to increase the resolution of our V_P model. Here, we investigate the effect of using more DAS data.

Narrower spacing of DAS receivers (10 m)

We reduce the channel spacing to 10 m, which includes more physically independent data, for two objectives: (1) to increase the inversion constraints by leveraging the dense data sampling, and (2) to investigate the resulting differences in the estimated velocity. In this case, the total number of channels is 284. The regularization is kept fixed at $1 \cdot 10^2$ and $5 \cdot 10^2$ for α and β, respectively. The overall reduction in the misfit of approximately 40 % is comparable with the previous results (Fig. 5.14). Deploying channels every 10 m on a deviated trajectory means that the velocity of each layer needs to fit 2 direct arrivals determined by two independent gauges. This results in an increased underdeterminancy of the inversion problem. The estimated velocities, as shown in Fig. 5.17, exhibit fluctuations just below 800 and 1500 m that are not present in the sonic logs. Furthermore, the velocities in some places within the reservoir do not have significant updates from the initial model. Apart from that, there are no notable differences.

Adding neighbouring receivers

In the previous, we selected DAS channels that are physically independent, every 15 or 10 m. Although a spacing of 10 m may offer a higher spatial resolution, the outcome is not necessarily beneficial. We aim to develop an FWI approach that leverages the dense data sampling to compensate for the lack of seismic events beside the direct arrival. Therefore, we add the channels located 1 m below the previous channels in Section 5.5.1, leading to total spacings of $1, 14, 1, 14, \ldots$ m and a total number of channels equal to 380. The extra data has been chosen so that it was recorded with 90 % gauge overlap—sensitivity to the same V_P—with the data in Fig. 5.12. Because adding more direct arrivals comes with more uncertainty, we increase the value of the regularization parameters, α and β, to $5 \cdot 10^2$ and $1 \cdot 10^3$.

The misfit in Fig. 5.18 starts at approximately 0.60 and ends at approximately 0.36 with a 40 % relative decrease. The velocity model in Fig. 5.19 inverted with denser data sampling matches best the sonic log averaged over 10 m. It also matches the other inverted and sonic-logs velocity models. More importantly, the large contrast above the geothermal reservoir is clearly visible with the current FWI of double amount of direct arrivals, where an increase in velocity appears at a depth of 2340 m. The structure inside the reservoir has the best recovery possible compared to all previous inversions.
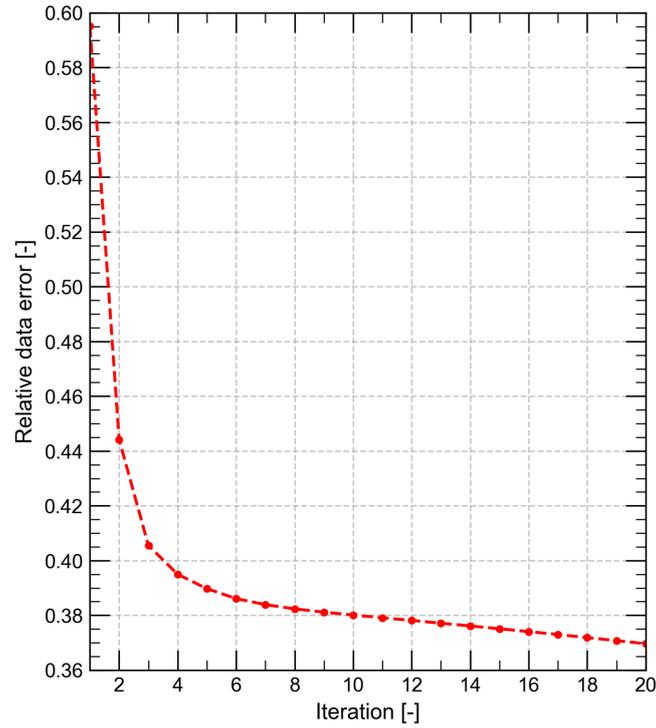
Figure 5.16: Relative data error of 20 iterations of FWI with the direct arrival of DAS data sampled every 10 m. In the first three iterations, the misfit is reduced considerably compared to later iterations, where the rate of change of the misfit slows down.
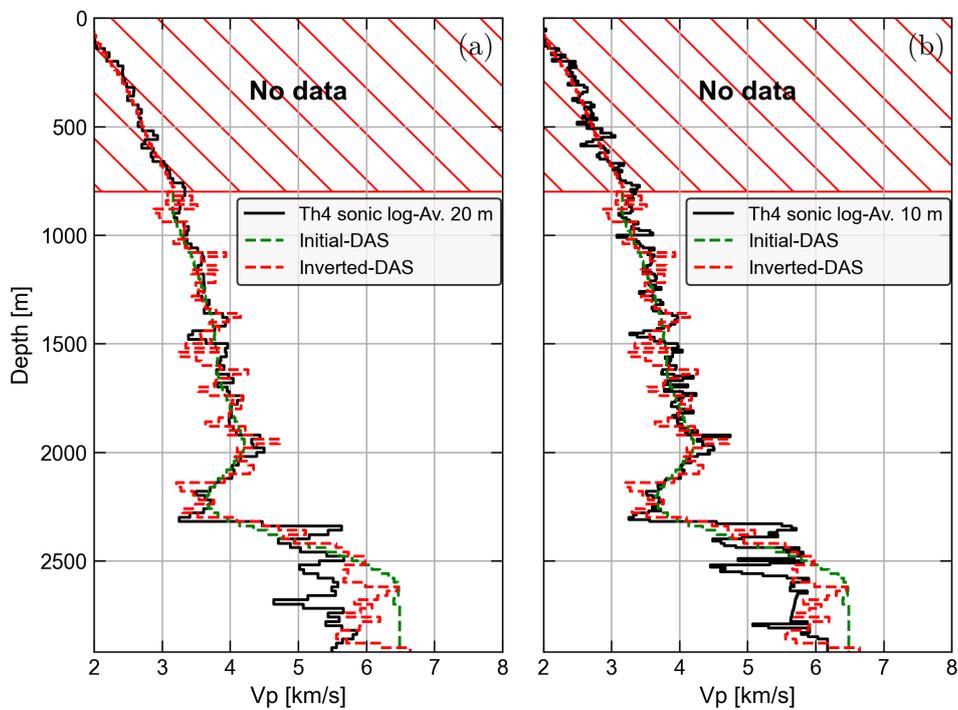

Figure 5.17: Comparison of the inverted V_{P} model from the windowed direct arrival of DAS data sampled every 10 m with the sonic-log profile in Th4 averaged over 20 m (a) and averaged over 10 m (b).
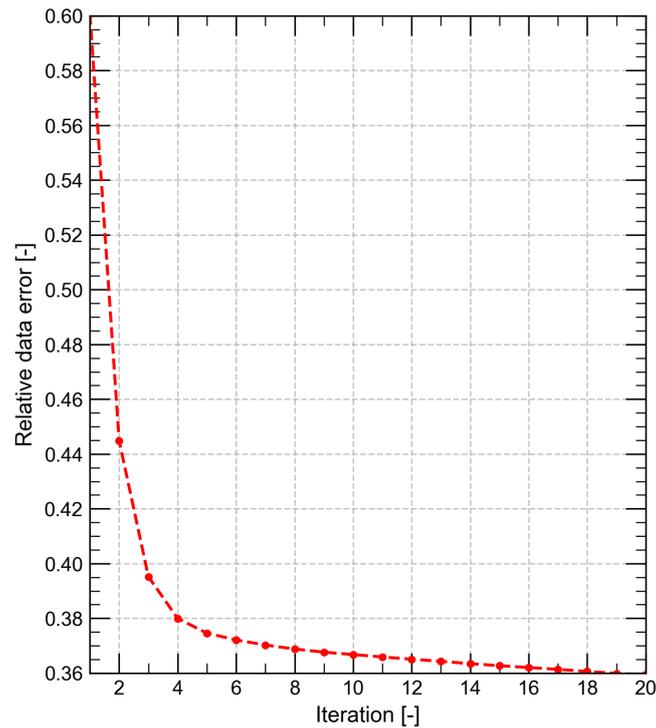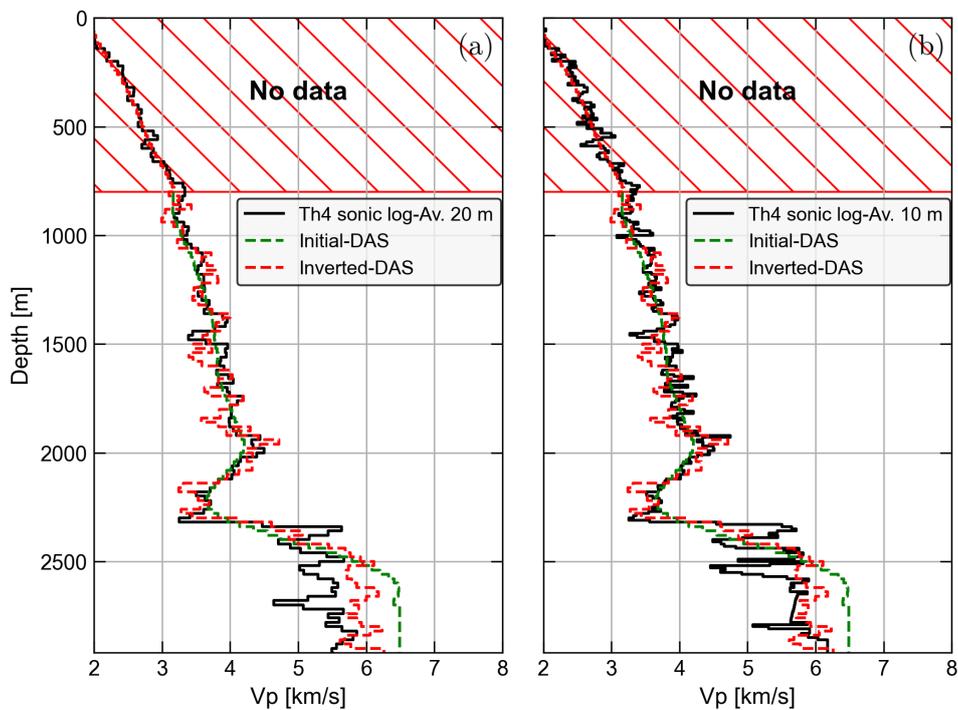
Figure 5.18: Relative data error of 20 FWI iterations with direct arrivals of 380 traces. In the first three iterations, the misfit is reduced considerably compared to later iterations, where the rate of change of the misfit slows down.

Figure 5.19: Comparison between the inverted V_P model from direct arrival of 380 traces with the sonic-log data in Th4 averaged over 20 m (a) and averaged over 10 m (b).

Model match

If we consider the average sonic log profiles as the true model, the model match reached by adding receivers can be evaluated. To quantify the total model match, we use the following formula:

$$\epsilon_m = \frac{||m_{true} - m_{inv}||}{||m_{true}||}, \tag{5.9}$$

where ϵ_m is the relative model misfit, m_{true} is the true model vector, and m_{inv} is the inverted model vector.

For a log profile averaged over 20 m (true model), ϵ_m equals 0.078, 0.089 and 0.078 for receivers spaced at 15, 10 and $1, 14, 1, 14, \ldots$ m, respectively. From these values, it is clear that estimating a layer velocity from two channels with isolated gauge gives poor results. While ϵ_m is equal for the first and third data sampling mentioned above, denser data sampling with adjacent receiver points is superior to denser data sampling with equally spaced receivers. To find the velocity misfit for each layer, we subtract true and inverted models and plot the difference in Fig. 5.20. It generally shows the highest values at the strong contrast in the region around 2350 m and the low velocity layers below, indicating that these areas were the most difficult to reconstruct. Inside the reservoir, the velocity difference for receivers at 15 m is variable, being large in some layers and small in other layers and with values spanning a wide range (-1.2 to 0.2 km/s). This range narrows (-1.2 to -0.2 km/s) when neighbouring receivers located 1 m away were included, suggesting that the velocity recovery becomes more robust.
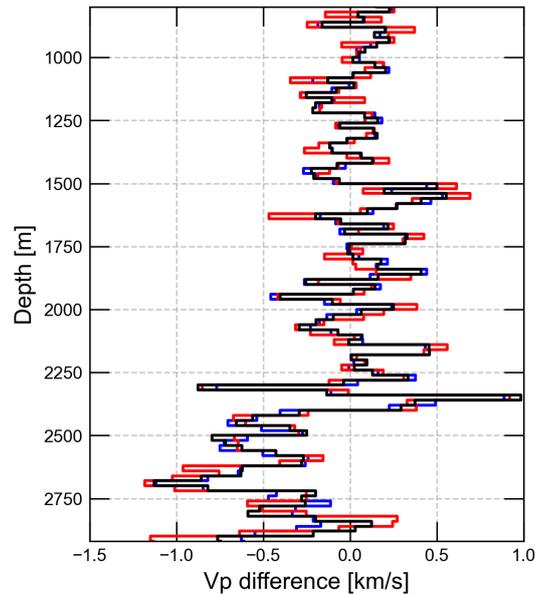

Figure 5.20: Difference between inverted V_P from the direct arrival of receivers spaced at 15 m (black line), 10 m (red line) and $1, 14, 1, 14, \ldots$ m (blue line), compared with the sonic-log profile averaged over 20 m.

5.6 Conclusions

We applied FWI to the VSP DAS data recorded with an optical fibre inside the casing in a deviated geothermal well in Munich. The uncertainty about the exact geometry of the fibre-optic cable and consequently the coordinates of the channels required the Laplacian smoothing factor β be greater than the diagonal-scaling damping factor α. Traditional FWI using full-record traces—in our case 2 seconds—led to poor results compared to other waveform inversions due to the presence of coherent noise. The results demonstrate that the DAS VSP data recorded inside the casing can give meaningful high-resolution V_P models. FWI to the windowed direct arrival gave a higher resolution V_P profile and better fit to the geophone and/or sonic-log models compared to traveltime tomography. Leveraging the dense sampling achieved with the DAS data needs careful consideration, where deploying 10 m distanced receivers to estimate the velocity of 20 m layers proved unreliable. On the other hand, adding neighbouring receivers gave the best resolution. The study demonstrated that FWI is superior to traveltime tomography, even when applied to only the first arriving waveform of inside-casing DAS data. A future field of FWI research should be the optimization of spatial sampling of DAS data for improved model resolution and efficient computation.

References

Al Hasani, M. and Drijkoningen, G. (2023). Experiences with distributed acoustic sensing using both straight and helically wound fibers in surface-deployed cables—A case history in Groningen, The Netherlands. Geophysics, 88(6):B369–B380.

Al Shoaibi, S. S., Florez, J. C., Farsi, S. A., Hinai, A. A., Nunez, A., in 't Panhuis, P., Taha, A., Van der Horst, M., Melanson, D., Wojtaszek, M., Moes, E., and Mccoy, K. (2022). The First Behind-Casing Fiber-Optic Installation in a High-Pressure High-Temperature Deep Gas Well in Oman. In SPE International Hydraulic Fracturing Technology Conference and Exhibition, page D021S005R001. Society of Petroleum Engineers.

Ali, A. and Jakobsen, M. (2011). Seismic characterization of reservoirs with multiple fracture sets using velocity and attenuation anisotropy data. Journal of Applied Geophysics, 75(3):590–602.

Balch, A. H., Lee, M., Miller, J., and Ryder, R. T. (1982). The use of vertical seismic profiles in seismic investigations of the earth. Geophysics, 47(6):906–918.

Barnolas, A., Larrasoaña, J. C., Pujalte, V., Schmitz, B., Sierro, F. J., Mata, M. P., van den Berg, B. C., Pérez-Asensio, J. N., Salazar,

References

Á., Salvany, J. M., et al. (2019). Alpine foreland basins. In *The Geology of Iberia: A Geodynamic Approach: Volume 4: Cenozoic Basins*, pages 7–59. Springer.

Barrias, A., Casas, J. R., and Villalba, S. (2016). A review of distributed optical fiber sensors for civil engineering applications. *Sensors*, 16(5):748.

Berkhout, A. and Verschuur, D. (2008). Imaging of multiple reflections.

Bredesen, K., Dalgaard, E., Mathiesen, A., Rasmussen, R., and Balling, N. (2020). Seismic characterization of geothermal sedimentary reservoirs: A field example from the Copenhagen area, Denmark. *Interpretation*, 8(2):T275–T291.

Chen, Y., Chen, Y., Fomel, S., Savvaidis, A., Saad, O. M., and Oboué, Y. A. S. I. (2023). Pyekfmm: a python package for 3D fast-marching-based traveltime calculation and its applications in seismology. *Seismological Research Letters*, 94(1):2050–2059.

Crampton, S. and Allen, P. (1995). Recognition of forebulge unconformities associated with early stage foreland basin development: example from the North Alpine Foreland Basin. *AAPG Bulletin*, 79(10):1495–1514.

Daley, T. M., Niu, F., Silver, P. G., and Majer, E. L. (2010). Acquisition of crosswell seismic monitoring data. In *Handbook of geophysical exploration: Seismic Exploration*, volume 40, pages 165–176. Elsevier.

Davydenko, M. and Verschuur, D. (2017). Full-wavefield migration: using surface and internal multiples in imaging. *Geophysical Prospecting*, 65(1):7–21.

Ernst, J. R., Green, A. G., Maurer, H., and Holliger, K. (2007). Application of a new 2D time-domain full-waveform inversion scheme to crosshole radar data. *Geophysics*, 72(5):J53–J64.

Fang, Z., Chin, K., Qu, R., and Cai, H. (2012). *Fundamentals of Optical Fiber Sensors*. John Wiley & Sons, Hoboken, NJ.

Fernández-Ruiz, M. R., Soto, M. A., Williams, E. F., Martin-Lopez, S., Zhan, Z., Gonzalez-Herraez, M., and Martins, H. F. (2020). Distributed acoustic sensing for seismic activity monitoring. *APL Photonics*, 5(3).

Ge, X., Lu, S., Li, X., Shang, J., Wu, H., Ren, K., and Wang, S. (2025). Full Waveform Inversion Using Deviated Well Distributed Acoustic Sensing Vertical Seismic Profiling Data: A Case Study. *Geophysics*, 90(5):1–55.

Grant, M. A. and Bixley, P. F. (2011). *Geothermal reservoir engineering*. Academic Press.

Hardage, B. A. (1985). Vertical seismic profiling. The Leading Edge, 4(11):59–59.

Hartog, A., Frignet, B., Mackie, D., and Clark, M. (2014). Vertical seismic optical profiling on wireline logging cable. Geophysical Prospecting, 62(4-Vertical Seismic Profiling and Microseismicity Frontiers):693–701.

Henninges, J., Martuganova, E., Stiller, M., Norden, B., and Krawczyk, C. M. (2021). Wireline distributed acoustic sensing allows 4.2 km deep vertical seismic profiling of the Rotliegend 150 °C geothermal reservoir in the North German Basin. Solid Earth, 12(2):521–537.

Herrmann, R. B. (2013). Computer programs in seismology: An evolving tool for instruction and research. Seismological Research Letters, 84(6):1081–1088.

Huenges, E. and Ledru, P. (2011). Geothermal energy systems: exploration, development, and utilization. John Wiley & Sons.

Jousset, P., Currenti, G., Schwarz, B., Chalari, A., Tilmann, F., Reinsch, T., Zuccarello, L., Privitera, E., and Krawczyk, C. M. (2022). Fibre optic distributed acoustic sensing of volcanic events. Nature Communications, 13(1):1753.

Junker, J. S., Obermann, A., Voigt, M., Maurer, H., Eruteya, O. E., Moscariello, A., Wiemer, S., and Zappone, A. (2025). Geophysical characterization of the in-situ CO2 mineral storage pilot site in Helguvik, Iceland. International Journal of Greenhouse Gas Control, 141:104320.

Kasahara, J., Hasada, Y., and Mikada, H. (2024). Geothermal reservoir characterization using distributed acoustic sensing from vertical seismic profiling in six geothermal fields in Japan. Distributed Acoustic Sensing in Borehole Geophysics, pages 205–223.

Kastrup, U., Deichmann, N., and Fröhlich, A. (2007). Evidence for an active fault below the northwestern Alpine foreland of Switzerland. Geophysical Journal International, 169(3):1273–1288.

Kastrup, U., Zoback, M. L., Deichmann, N., Evans, K. F., Giardini, D., and Michael, A. J. (2004). Stress field variations in the Swiss Alps and the northern Alpine foreland derived from inversion of fault plane solutions. Journal of Geophysical Research: Solid Earth, 109(B1).

Kuhlemann, J. and Kempf, O. (2002). Post-Eocene evolution of the North Alpine Foreland Basin and its response to Alpine tectonics. Sedimentary Geology, 152(1-2):45–78.

Lindsey, N. J., Rademacher, H., and Ajo-Franklin, J. B. (2020). On the broadband instrument response of fiber-optic DAS arrays. Journal of Geophysical Research: Solid Earth, 125(2):e2019JB018145.

References

Lipus, M. P., Schölderle, F., Reinsch, T., Wollin, C., Krawczyk, C. M., Pfrang, D., and Zosseder, K. (2021). Dynamic motion monitoring of a 3.6 km long steel rod in a borehole during cold-water injection with distributed fiber-optic sensing. Solid Earth Discussions, pages 1–26.

Lucia, F. J., Kerans, C., and Jennings Jr, J. W. (2003). Carbonate reservoir characterization. Journal of Petroleum Technology, 55(06):70–72.

Lüschen, E., Wolfgramm, M., Fritzer, T., Dussel, M., Thomas, R., and Schulz, R. (2014). 3D seismic survey explores geothermal targets for reservoir characterization at Unterhaching, Munich, Germany. Geothermics, 50:167–179.

Ma, X., Hertrich, M., Amann, F., Bröker, K., Gholizadeh Doonechaly, N., Gischig, V., Hochreutener, R., Kästli, P., Krietsch, H., Marti, M., et al. (2021). Multi-disciplinary characterizations of the Bedretto Lab–a unique underground geoscience research facility. Solid Earth Discussions, 2021:1–40.

Mad Zahir, M. H., Abdul Aziz, K. M., Ghazali, A. R., and Abdul Latiff, A. H. (2023). Effectiveness of fiber optic distributed acoustic sensing (DAS) in vertical seismic profiling (VSP) field survey. Applied Sciences, 13(8):5002.

Martuganova, E., Stiller, M., Bauer, K., Henninges, J., and Krawczyk, C. M. (2021). Cable reverberations during wireline distributed acoustic sensing measurements: their nature and methods for elimination. Geophysical Prospecting, 69(5):1034–1054.

Martuganova, E., Stiller, M., Norden, B., Henninges, J., and Krawczyk, C. M. (2022). 3D deep geothermal reservoir imaging with wireline distributed acoustic sensing in two boreholes. Solid Earth, 13(8):1291–1307.

Mateeva, A., Lopez, J., Potters, H., Mestayer, J., Cox, B., Kiyashchenko, D., Wills, P., Grandi, S., Hornman, K., Kuvshinov, B., et al. (2014). Distributed acoustic sensing for reservoir monitoring with vertical seismic profiling. Geophysical Prospecting, 62(4-Vertical Seismic Profiling and Microseismicity Frontiers):679–692.

Meehan, T. (2018). Evolution of the propagator matrix method and its implementation in seismology. arXiv preprint arXiv:1801.04635.

Moeck, I. S., Dussel, M., Weber, J., Schintgen, T., and Wolfgramm, M. (2019). Geothermal play typing in Germany, case study Molasse Basin: a modern concept to categorise geothermal resources related to crustal permeability. Netherlands Journal of Geosciences, 98:e14.

Molenaar, M. M., Fidan, E., and Hill, D. J. (2012). Real-time Downhole Monitoring of Hydraulic Fracturing Treatments Using Fibre Optic Distributed Temperature and Acoustic Sensing. In *SPE/EAGE European Unconventional Resources Conference and Exhibition*, pages SPE–152981. Society of Petroleum Engineers.

Paitz, P., Edme, P., Gräff, D., Walter, F., Doetsch, J., Chalari, A., Schmelzbach, C., and Fichtner, A. (2021). Empirical investigations of the instrument response for distributed acoustic sensing (DAS) across 17 octaves. *Bulletin of the Seismological Society of America*, 111(1):1–10.

Parker, T., Shatalin, S., and Farhadiroushan, M. (2014). Distributed Acoustic Sensing–a new tool for seismic applications. *First Break*, 32(2):61–69.

Pfiffner, O. A. (1986). Evolution of the north Alpine foreland basin in the Central Alps. *Foreland basins*, pages 219–228.

Przybycin, A. M., Scheck-Wenderoth, M., and Schneider, M. (2017). The origin of deep geothermal anomalies in the German Molasse Basin: results from 3D numerical models of coupled fluid flow and heat transport. *Geothermal Energy*, 5:1–28.

Qu, L., Pan, W., Innanen, K., Macquet, M., and Lawton, D. (2024). Feasibility study of anisotropic full-waveform inversion with DAS data in a vertical seismic profile configuration at the Newell County Facility, Alberta, Canada. *Surveys in Geophysics*, 45(4):1117–1142.

Raji, W. O., Gao, Y., and Harris, J. M. (2017). Wavefield analysis of crosswell seismic data. *Arabian Journal of Geosciences*, 10:1–9.

Rawlinson, N. and Sambridge, M. (2005). The fast marching method: an effective tool for tomographic imaging and tracking multiple phases in complex layered media. *Exploration Geophysics*, 36(4):341–350.

Reiser, F., Schmelzbach, C., Maurer, H., Greenhalgh, S., and Hellwig, O. (2017). Optimizing the design of vertical seismic profiling (VSP) for imaging fracture zones over hardrock basement geothermal environments. *Journal of Applied Geophysics*, 139:25–35.

Reiser, F., Schmelzbach, C., Sollberger, D., Maurer, H., Greenhalgh, S., Planke, S., Kästner, F., Flóvenz, Ó., Giese, R., Halldórsdóttir, S., et al. (2020). Imaging the high-temperature geothermal field at Krafla using vertical seismic profiling. *Journal of Volcanology and Geothermal Research*, 391:106474.

References

Rybach, L. (2003). Geothermal energy: sustainability and the environment. Geothermics, 32(4-6):463–470.

Schlunegger, F. and Kissling, E. (2024). A Review of How Our Understanding on the Relationships between the Alps and the North Alpine Foreland Basin has Evolved. Geodynamics of the Alps 3: Collisional Processes, page 125.

Schölderle, F., Lipus, M., Pfrang, D., Reinsch, T., Haberer, S., Einsiedl, F., and Zosseder, K. (2021). Monitoring cold water injections for reservoir characterization using a permanent fiber optic installation in a geothermal production well in the Southern German Molasse Basin. Geothermal Energy, 9:1–36.

Sethian, J. A. (1996). A fast marching level set method for monotonically advancing fronts. Proceedings of the National Academy of Sciences, 93(4):1591–1595.

Simiyu, S. M. (2000). Geothermal reservoir characterization: Application of microseismicity and seismic wave properties at Olkaria, Kenya rift. Journal of Geophysical Research: Solid Earth, 105(B6):13779–13795.

Söding, H., Maurer, H., and Fechner, T. (2024). Source-and receiver-coupling effects for time-domain Full Waveform Inversion. In EGU General Assembly Conference Abstracts, page 19778.

Sollberger, D., Igel, H., Schmelzbach, C., Edme, P., Van Manen, D.-J., Bernauer, F., Yuan, S., Wassermann, J., Schreiber, U., and Robertsson, J. O. (2020). Seismological processing of six degree-of-freedom ground-motion data. Sensors, 20(23):6904.

Staněk, F., Jin, G., and Simmons, J. (2022). Fracture imaging using DAS-recorded microseismic events. Frontiers in Earth Science, 10:907749.

Udd, E. and Spillman Jr, W. B., editors (2024). Fiber Optic Sensors: An Introduction for Engineers and Scientists. John Wiley & Sons, Hoboken, NJ.

Verschuur, D. and Neumann, E. (1999). Integration of OBS data and surface data for OBS multiple removal. In 61st EAGE Conference and Exhibition, pages cp–132. European Association of Geoscientists & Engineers.

Virieux, J., Asnaashari, A., Brossier, R., Métivier, L., Ribodetti, A., and Zhou, W. (2017). An introduction to full waveform inversion. In Encyclopedia of exploration geophysics, pages R1–1. Society of Exploration Geophysicists.

Warner, M., Ratcliffe, A., Nangoo, T., Morgan, J., Umpleby, A., Shah, N., Vinje, V., Štekl, I., Guasch, L., Win, C., et al. (2013). Anisotropic 3D full-waveform inversion. Geophysics, 78(2):R59–R80.

Webster, P., Wall, J., Perkins, C., and Molenaar, M. (2013). Micro-seismic detection using distributed acoustic sensing. In SEG International Exposition and Annual Meeting, pages SEG–2013. Society of Exploration Geophysicists.

Willis, M. E., Barfoot, D., Ellmauthaler, A., Wu, X., Barrios, O., Erdemir, C., Shaw, S., and Quinn, D. (2016a). Quantitative quality of distributed acoustic sensing vertical seismic profile data. The Leading Edge, 35(7):605–609.

Willis, M. E., Erdemir, C., Ellmauthaler, A., Barrios, O., and Barfoot, D. (2016b). Comparing DAS and geophone zero-offset VSP data sets side-by-side. CSEG Recorder, 41(6):22–26.

Yasin, Q., Gholami, A., Majdański, M., Liu, B., and Golsanami, N. (2023). Seismic characterization of geologically complex geothermal reservoirs by combining structure-oriented filtering and attributes analysis. Geothermics, 112:102749.

Yilmaz, Ö. (2001). Seismic data analysis: Processing, inversion, and interpretation of seismic data. Society of exploration geophysicists.

Zhan, Z. (2020). Distributed acoustic sensing turns fiber-optic cables into sensitive seismic antennas. Seismological Research Letters, 91(1):1–15.

Chapter 6

Conclusion and Outlook

6.1 Conclusions

In this thesis, I studied the feasibility of geophysical methods—specifically CSEM and seismic FWI—for monitoring variations in relevant properties caused by temperature changes in low-enthalpy geothermal reservoirs. Through a combination of modeling studies, synthetic tests, and field data applications, I confirmed the applicability of these methods in real-world monitoring scenarios.

The feasibility study on the CSEM method, conducted for the Delft Campus Geothermal Project, demonstrated that surface-to-borehole configurations allow the detection of a 4 Ω·m increase in resistivity associated with a 25 °C decrease in temperature in the Delft Sandstone reservoir. Further careful consideration of the source frequency and offset allows for such a detection with the maximum resolving capability. A source frequency of around 1 Hz generated EM fields that could be determined above a noise floor of 10^{-12} V/m, down to a depth of 3000 m in the Delft Campus layered resistivity model. This propagation depth was enough to investigate the entire thickness of the reservoir and some area below it, where the difference in time-lapse EM fields was noticeable to above 30 %. A resistivity increase of a small radius, 300 m, was more challenging to detect. The source offset of 1000 to 2000 m was suitable for propagating EM fields with sufficient strength to ensure adequate sensitivity. By modelling environmental disturbances such as random recording noise, survey-repeatability errors, near-surface temperature fluctuations and casing effects, it can be concluded that the impact of a steel casing was the most significant as it heavily attenuated the electric field to a radius of 100 m around it. Thus, all field measurements should maintain an appropriate distance from the injection and production steel casing. Since the measurements will be collected in a monitoring well, it would be essential to keep the well design free of highly electrically conductive material.

These findings establish CSEM as a promising tool for enabling informed management decisions to enhance the sustainability of geothermal energy production.

For high-resolution seismic characterization required for geothermal monitoring, I developed a novel FWI approach for 99 % accurate estimation of P impedance. To achieve such accuracy, I chose a sequential work flow beginning with inverting for velocity and then inverting for impedance. I introduced an in-between step called temporal phase resemblance to mitigate remaining small phase errors. The convergence of the FWI was improved by deploying starting models estimated via travel time tomography. Synthetic experiments confirmed the robustness of this approach, which successfully detected impedance variations exceeding 2 %, crucial to identifying temperature-driven variations within the reservoir. Field applications at the Munich site further validated these methods, revealing detailed structural insights into the reservoir and overburden layers, and demonstrating the practical value of seismic FWI for operational geothermal applications.

Furthermore, a comparative study on FWI of DAS versus geophone data highlighted the potential advantages and limitations of VSP acquisition based on fibre-optic cables inside the casing. The DAS data could be recorded along the reservoir depths, which could not be achieved with wireline geophones. However, the former faced challenges related to coupling issues and reduced SNRs. My results showed that careful preprocessing and a robust inversion strategy could overcome some of the challenges, for example, inaccurate positioning of the channels and the absence of subsurface seismic events other than the direct wave. By focusing the FWI on the P-wave arrival, inverted models had higher resolution compared to those from travel time tomography. These models were validated by sonic logs collected in the same borehole (Th4). Leveraging the dense spatial sampling of the DAS data did not necessarily improve the resolution of the inverted velocity model.

Although this research originally aimed to combine seismic FWI and CSEM for monitoring studies at the Delft campus geothermal site, the installation of a fibre-optic cable did not go as planned due to the instability of the newly drilled borehole(s). Therefore, the focus shifted to FWI of the DAS data from the Munich site. The lack of EM acquisition at the latter site meant that spatial and temporal overlap of the two geophysical datasets would be absent. Consequently, the CSEM and the seismic studies provided separate insights into the subsurface.

The modelling in this thesis necessarily relied on simplified assumptions, for example, horizontally layered, isotropic and lossless media for both seismic and EM simulations, reflecting the constraints imposed by the available field data. For the Delft site, the resistivity model was constructed from logs acquired in other regions, without borehole-fluid corrections and without including 3D heterogeneity, which limits its geological fidelity. For the Munich site, seismic FWI was restricted by sparse source coverage, limited angu-

lar aperture, and the absence of time-lapse acquisitions. These constraints reduced the capacity to fully represent reservoir complexity, detect limited-span temporal changes, or validate approaches with time-lapse field datasets. Moreover, because seismic and EM data were not co-located in space, joint inversion and integrated interpretation could not be realised, which led to independent evaluations of each method. The findings of this research therefore best represent feasibility assessments under idealised conditions, with generalisability to more complex geothermal settings requiring further investigation and coordinated field campaigns.

6.2 Outlook

The findings of this research establish a foundation for future geophysical monitoring of low-enthalpy reservoirs and can be extended to the areas discussed in the following.

6.2.1 Incorporating reservoir modelling

In Chapter 3, it was considered that temperature changes have a sharp transition from cold to warm volumes for the sake of model simplicity. Numerical reservoir simulation shows that this transition is rather gradual (Wang et al., 2021). Thus, the resulting variations in electrical resistivity would have an incremental increase. This means that these variations would be less than 4 Ω.m in the case of the Delft campus geothermal reservoir.

Future CSEM monitoring studies of low-enthalpy reservoirs should incorporate variations based on detailed temperature simulations to better represent gradual transitions from hot to cold regions. In an ideal scenario, these simulations would also deploy models that incorporate reservoir geological and petrophysical heterogeneities. Such a non-uniformity of rock properties can lead to uneven thermal depletion (Crooijmans et al., 2016; Zhang et al., 2023), with heat being extracted from areas of the geothermal reservoir in production faster than others. It can also affect fluid flow, leading to preferential fluid pathways (Hewett and Behrens, 1990), where reinjected fluids are channeled back to the production well without having enough time to warm up.

Overall, all these aspects can cause temperature changes to differ in amount or to have channel-like distributions. For a more generalized statement on the feasibility of CSEM monitoring of low-enthalpy reservoirs, different reservoir models that have different features should be studied. This could also involve finding suitable source frequencies and positions, or testing the feasibility of detecting variations smaller than $4\Omega\cdot m$, occurring over thinner thicknesses or a narrow course.

6.2.2 CSEM inversion and application to field data

With the selected source frequency of 1 Hz in Chapter 3, it was noticed that the difference in electric field caused by time-lapse variations is scattered over a wide area, which implies a low resolving power of the variation boundaries. Furthermore, geothermal energy production takes place over local volumes and the accuracy of estimating them is necessary, especially when there is a smooth transition. Therefore, further research should investigate the resolution capabilities of CSEM inversion (Black et al., 2010; Tietze et al., 2015; Constable and Stern, 2022) to monitor low-enthalpy reservoirs. The developed CSEM inversion methods can then be rigorously validated using field data. More field data would help refine theoretical models, confirm the findings of CSEM monitoring studies, and bridge the gap between theoretical studies and operational field monitoring.

6.2.3 Time-lapse VSP surveys

In Chapter 4, the developed seismic FWI approach was applied only to baseline field data. Conducting a repeat VSP survey at the Munich geothermal site and inverting the acquired time-lapse data are essential to validate such a FWI approach of acoustic impedance for geothermal monitoring. As mentioned in Chapter 4, there are a few inversion strategies to estimate the monitoring model. It is recommended to test them to find which strategy would give the best model that captures time-lapse impedance variations with our sequential FWI approach.

Time-lapse variations due to heat production happen over limited reservoir volumes. A layered impedance model with one source location is not expected to directly give the lateral extent of such volumes. However, the direct arrival mode recorded at the reservoir for this source location has sensitivity to the seismic properties of a certain area in production, while the reflection modes from the reservoir have sensitivity to other areas. It would be valuable to investigate whether 3D variations would change the acoustic impedance estimated from these different modes separately. This FWI approach would then combine the work done in Chapters 4 and 5.

In both of the recommended future research areas, high repeatability of the survey acquisition parameters is very important, in addition to using the same value of regularization parameters in time-lapse inversion. Assuming that the source signature (vibroseis sweep) is exact across surveys, it would suffice to use the STF estimated from the base data in the FWI of monitoring data. Detecting impedance variations from time-lapse surveys would decisively demonstrate the real-world utility of seismic methods in monitoring low-enthalpy reservoirs over their operational lifetime.

6.2.4 Efficient Jacobian calculation

To calculate the first-order partial derivatives (Jacobian) matrix in Chapters 4 and 5, a numerical-perturbation method was used, which is robust but computationally expensive. Although it provided an accurate calculation, crucial for determining the second-order derivatives (Hessian) matrix, the number of full-waveform modelling runs was equal to the number of model parameters. For larger models that include more complex 2D or 3D structure, the numerical-perturbation method is prohibitively intensive in terms of computational resources. Other techniques can be used to calculate the approximate Hessian based on the gradient, such as the adjoint method (Fichtner et al., 2006). However, the convergence behavior of these methods is linear and is not granted if starting models close to the global minimum are not used. Thus, a more efficient calculation of the Jacobian is an area for future developments (Coleman and Verma, 1996).

6.2.5 Multi-offset VSP surveys

In Chapters 4 and 5, a layered model was assumed because the VSP dataset included only two source locations, of which only one was used. Expanding VSP survey designs to include multiple source locations at different offsets will advance the inversion beyond the current assumption of a layered medium. Comprehensive 2D and 3D subsurface models constructed from multi-offset VSP data would significantly enhance geological understanding and improve reservoir monitoring.

6.2.6 Clamped fibre-optic installation inside the casing

Improving installation methods of the fibre-optic cable inside borehole casings is critical to achieving high-quality seismic data for FWI. This can benefit from already existing borehole geophones technology, such as electromechanical (St-Onge et al., 2013), spring-loaded (Leary et al., 1990), inflatable bladder (Kalinski, 2012) or hydraulic clamping (Daley et al., 2016). New installation technologies should ensure strong and consistent coupling of fibre-optic cables throughout well sections, enhancing the SNR and data reliability.

6.2.7 Efficient modeling of strain-rate data

In Chapter 5, the model was discretized with a layer thickness of 20 m for various reasons. One of them is the unpractical computational time of waveform modelling in the case of thinner layers, e.g. 10 or 5 m, in addition to the preclusion of physically independent channels in the same layer. Hence, most of the DAS data were discarded. With the current development of DAS systems (He and Liu, 2021; Shang et al., 2022), signals can

be recorded with high SNR and a gauge length as short as a few meters (Kishida et al., 2021). Efficient modelling methods of the strain rate would allow to take advantage of all the data, offering a great opportunity for detailed subsurface characterization. This is especially the case for extensive parameter spaces in 2D and 3D models.

6.2.8   Joint inversion of CSEM and seismic data

Ultimately, the successful implementation of these outlined endeavors would enable real-world realization of joint inversion algorithms combining field CSEM and seismic datasets (Kalscheuer et al., 2015). Two main strategies for integrating multiphysics data are already existing: The first approach simultaneously or cooperatively imposes similarities between two models, i.e. acoustic impedance and electrical resistivity, based on structural constraints (Haber and Oldenburg, 1997; Gallardo and Meju, 2003; Molodtsov et al., 2013). The second approach links physical properties through their petrophysical laws or attributes (Carcione et al., 2007) for joint inversion (Hoversten et al., 2006; Gao et al., 2012). The capabilities of both approaches for the specific application of low-enthalpy reservoir monitoring remain largely unexamined. An integrated approach would benefit from complementary sensitivities (Meju et al., 2003), substantially improving the robustness of geothermal reservoir monitoring and well-informed production management.

References

Black, N., Wilson, G. A., Gribenko, A. V., and Zhdanov, M. S. (2010). 3D inversion of time-lapse CSEM data for reservoir surveillance. In SEG Technical Program Expanded Abstracts 2010, pages 716–720. Society of Exploration Geophysicists.

Carcione, J. M., Ursin, B., and Nordskag, J. I. (2007). Cross-property relations between electrical conductivity and the seismic velocity of rocks. Geophysics, 72(5):E193–E204.

Coleman, T. F. and Verma, A. (1996). Structure and efficient Jacobian calculation. Technical report, Cornell University.

Constable, S. and Stern, L. A. (2022). Monitoring offshore CO2 sequestration using marine CSEM methods; constraints inferred from field-and laboratory-based gas hydrate studies. Energies, 15(19):7411.

Crooijmans, R. A., Willems, C. J., Nick, H. M., and Bruhn, D. (2016). The influence of facies heterogeneity on the doublet performance in low-enthalpy geothermal sedimentary reservoirs. Geothermics, 64:209–219.

Daley, T. M., Miller, D., Dodds, K., Cook, P., and Freifeld, B. (2016). Field testing of modular borehole monitoring with simultaneous distributed acoustic sensing and geophone vertical seismic profiles at Citronelle, Alabama. Geophysical Prospecting, 64(5):1318–1334.

Fichtner, A., Bunge, H.-P., and Igel, H. (2006). The adjoint method in seismology: I. Theory. Physics of the Earth and Planetary Interiors, 157(1-2):86–104.

Gallardo, L. A. and Meju, M. A. (2003). Characterization of heterogeneous near-surface materials by joint 2D inversion of dc resistivity and seismic data. Geophysical Research Letters, 30(13).

Gao, G., Abubakar, A., and Habashy, T. M. (2012). Joint petrophysical inversion of electromagnetic and full-waveform seismic data. Geophysics, 77(3):WA3–WA18.

Haber, E. and Oldenburg, D. (1997). Joint inversion: a structural approach. Inverse problems, 13(1):63.

He, Z. and Liu, Q. (2021). Optical fiber distributed acoustic sensors: A review. Journal of Lightwave Technology, 39(12):3671–3686.

Hewett, T. A. and Behrens, R. A. (1990). Conditional simulation of reservoir heterogeneity with fractals. SPE formation evaluation, 5(03):217–225.

Hoversten, G. M., Cassassuce, F., Gasperikova, E., Newman, G. A., Chen, J., Rubin, Y., Hou, Z., and Vasco, D. (2006). Direct reservoir parameter estimation using joint inversion of marine seismic AVA and CSEM data. Geophysics, 71(3):C1–C13.

Kalinski, M. (2012). A small, lightweight borehole receiver for crosshole and downhole seismic testing. Geotechnical Testing Journal, 35(2):363–366.

Kalscheuer, T., Blake, S., Podgorski, J. E., Wagner, F., Green, A. G., Maurer, H., Jones, A. G., Muller, M., Ntibinyane, O., and Tshoso, G. (2015). Joint inversions of three types of electromagnetic data explicitly constrained by seismic observations: results from the central Okavango Delta, Botswana. Geophysical Journal International, 202(3):1429–1452.

Kishida, K., Liu, Q., Azuma, D., and He, Z. (2021). A new generation of DAS with greatly improved gauge length and spatial resolving function from the same measurement. In Proceedings of the 14th SEGJ International Symposium, Tokyo, Japan, 18–21 October 2021, pages 12–14. Society of Exploration Geophysicists and Society of Exploration.

Leary, P., Li, Y.-G., and Manov, D. (1990). A microprocessor-based borehole seismic sonde. Bulletin of the Seismological Society of America, 80(3):717–736.

References

Meju, M. A., Gallardo, L. A., and Mohamed, A. K. (2003). Evidence for correlation of electrical resistivity and seismic velocity in heterogeneous near-surface materials. Geophysical Research Letters, 30(7).

Molodtsov, D. M., Troyan, V. N., Roslov, Y. V., and Zerilli, A. (2013). Joint inversion of seismic traveltimes and magnetotelluric data with a directed structural constraint. Geophysical Prospecting, 61(6-Challenges of Seismic Imaging and Inversion Devoted to Goldin):1218–1228.

Shang, Y., Sun, M., Wang, C., Yang, J., Du, Y., Yi, J., Zhao, W., Wang, Y., Zhao, Y., and Ni, J. (2022). Research progress in distributed acoustic sensing techniques. Sensors, 22(16):6060.

St-Onge, A., Eaton, D., and Pidlisecky, A. (2013). Borehole vibration response to hydraulic fracture pressure. In 75th EAGE Conference & Exhibition incorporating SPE EUROPEC 2013, pages cp–348. European Association of Geoscientists & Engineers.

Tietze, K., Ritter, O., and Veeken, P. (2015). Controlled-source electromagnetic monitoring of reservoir oil saturation using a novel borehole-to-surface configuration. Geophysical Prospecting, 63(6):1468–1490.

Wang, Y., Voskov, D., Khait, M., Saeid, S., and Bruhn, D. (2021). Influential factors on the development of a low-enthalpy geothermal reservoir: A sensitivity study of a realistic field. Renewable Energy, 179:641–651.

Zhang, C., Wang, X., Jiang, C., and Zhang, H. (2023). Numerical simulation of geothermal energy production from hot dry rocks under the interplay between the heterogeneous fracture and stimulated reservoir volume. Journal of Cleaner Production, 414:137724.

Acknowledgments

Curriculum Vitae

Mahmoud Eltayieb

✉ m.f.m.i.eltayieb@tudelft.nl

📱 +31 68 321 71 62

in [Mahmoud Eltayieb](https://linkedin.com)

📍 Dr. H. Colijnlaan 339, 2283XL Rijswijk

Education

Mar 2021 - Mar 2025	**Delft University of Technology, the Netherlands & Federal Institute of Technology Zurich, Switzerland**

- Joint Doctorate of Philosophy in Applied Geophysics, successfully:

Aug 2018 - Aug 2020	**University of Bergen, Norway**

- Master of Science in Geophysics, grade: A

Oct 2011 - Jun 2015	**Mansoura University, Egypt**

- Bachelor of Science in Geophysics, grade: B

Experience

Jan 2021 - Mar 2021	**Graduate Teaching Assistant in Global and Applied Geophysics, University of Bergen, Norway**

Aug 2020 - Dec 2020	**Teaching Assistant in Signal Processing and Inversion, University of Bergen, Norway**
Jan 2019 - Mar 2021	**Household Mover, Bergen Flyttetjeneste AS, Norway**
Jan 2020 - May 2020	**Teaching Assistant in Computational Geophysics, University of Bergen, Norway**
Aug 2017 - April 2018	**Medical Representative, Rovamed Pharma, Egypt**
Jul 2014 - Aug 2014	**Egyptian General Petroleum Corporation (EGPC), Egypt**

Publications

Eltayieb, M., Drijkoningen, G., Reinsch, T., Maurer, H.-R., and Hoerbrand, T. (2025). FWI of VSP Data for Munich Geothermal Reservoir Monitoring. Geophysics. To be submitted.

Eltayieb, M., Werthmüller, D., Drijkoningen, G., and Slob, E. (2023). Feasibility Study Controlled-Source Electromagnetic Method for Monitoring Low-Enthalpy Geothermal Reservoirs. Applied Sciences, 13(16):9399.

Eltayieb, M. F. M. I., Werthmüller, D., Drijkoningen, G. G., and Slob, E. C. (2022). Feasibility Study of Monitoring the Delft Geothermal Project Using the Land Controlled-Source Electromagnetic Method. In 13th European Geothermal PhD Days, page 13, Aachen, Germany.

Luo, W., Drijkoningen, G., Eltayieb, M., Amann, F., and Vardon, P. J. (2025). Feasibility Study of Single-Well Dual-Cable DAS for Microseismic Monitoring of Geothermal Operations. Rock Mechanics and Rock Engineering. Re-submitted after major revision.

Slob, E. C., Eltayieb, M., Ghose, R., Drijkoningen, G., and Werthmüller, D. (2021). Examples of Seismic Shallow Subsurface Characterisation and Deep Electromagnetic Monitoring. In Near Surface Geoscience & Exhibition, Bordeaux, France.